ABSTRACT

Title of dissertation: NOVEL EMITTANCE MEASUREMENT THROUGH EXPERIMENTAL STUDY OF ENVELOPE MODE RESONANCE IN A HIGH-INTENSITY PARTICLE BEAM

William D. Stem, Doctor of Philosophy, 2015

Dissertation directed by: Professor Timothy Koeth
Department of Physics

On-line monitoring of beam quality for high-intensity particle beams requires non-invasive transverse phase space diagnostics. Such diagnostics are in high demand for use in heavy ion accelerators and free-electron lasers (FELs). A technique to measure emittance using multi-turn resonant excitation of the quadrupole envelope mode has been demonstrated at the University of Maryland Electron Ring (UMER).

The rms Kapchinsky-Vladimirsky (KV) equations predict the time-evolution of particle beam envelopes. Linear perturbations to the matched envelope solution of these equations excite normal modes at space-charge-dependent natural frequencies. This experiment employs periodic, impulsed perturbations to drive resonant excitations of these modes. Steady state resonance structure in the form of a lattice is predicted using analytic solutions of a delta-kicked simple harmonic oscillator (SHO). Numerical simulations of this SHO along with simulations from the WARP envelope solver and particle-in-cell (PIC) codes are documented.

This dissertation presents the first proof-of-principle experimental resonant excitation of the quadrupole envelope mode in a high-intensity particle beam. To excite the mode experimentally, an rf-driven electric quadrupole is constructed and installed in UMER. The quadrupole fields are driven by a tunable resonant tank circuit designed and built for this experiment. After resonant excitation, the knock-out imaging method is used to collect 3 ns synchronized transverse time slice images of the beam. Image moments are analyzed and show good agreement with simulation. Emittance can then be inferred from the measured natural frequencies of the envelope modes utilizing a conversion obtained through simulation. A direct emittance measurement is performed using a conventional pinhole scan at injection as an experimental validation of the envelope resonance method.

NOVEL EMITTANCE MEASUREMENT THROUGH EXPERIMENTAL STUDY OF ENVELOPE MODE RESONANCE IN A HIGH-INTENSITY PARTICLE BEAM

by

William Durst Stem

Dissertation submitted to the Faculty of the Graduate School of the
University of Maryland, College Park in partial fulfillment
of the requirements for the degree of
Doctor of Philosophy
2015

Advisory Committee:
Professor Timothy Koeth, Co-Chair/Advisor
Professor Patrick O'Shea, Co-Chair
Professor Rami Kishek
Professor Thomas Antonsen
Professor Michael Coplan, Dean's Representative
Dr. Brian Beaudoin

If I have seen further it is by standing on the shoulder of giants.

–Isaac Newton

Acknowledgments

Although this was my project, I couldn't have done it without the help and support of a multitude of people. It has been my honor to work with many of the brightest, most talented, passionate people I have ever had the pleasure of knowing. I would first like to thank my advisor, Professor Timothy Koeth, for his continuous support of my academic growth, and for his creative and technical guidance throughout my research. I would also like to thank Dr. Brian Beaudoin for his advice and assistance in the laboratory. He has served as a mentor, teaching me nearly all I know about electrical engineering, and he was always willing to work with me to diagnose a problem. Another mentor I would like to thank is Dr. Irving Haber. His simulation assistance was invaluable. What's more, his creative and novel research suggestions were critical to the direction and success of my thesis. I would also like to thank Professor Patrick O'Shea, Professor Rami Kishek, Professor Thomas Antonsen, and Professor Michael Coplan for taking the time to serve on my dissertation advisory committee.

I would like to thank the remainder of the UMER group for their support, understanding, and patience throughout my research. I monopolized UMER as I was completing this project, postponing upgrades that were vital to the progress of others. Thanks to Kiersten Ruisard for her helpful discussions and experimental collaborations. Thanks to Dr. Santiago Bernal, Dr. David Sutter, and Dr. Eric

Montgomery for their helpful advice throughout my years at IREAP. Thanks also to my graduated UMER colleagues Dr. Hao Zhang, Dr. Yichao Mo, and Dr. Kamal PoorRezaei for their assistance in the infancy of my project.

In the machine shop, constructing my quadrupole would not have been possible without the knowledgeable aid of Jay Pile. His creative ideas and technical ability are unparalleled, and he always had a word of encouragement. Nolan Ballew also had helpful suggestions in the design and construction phase. They both deserve my thanks.

I would like to thank the scientists who have lent me their time on this project. Dr. Luke Johnson and Dr. Aram Vartanyan always welcomed me with open doors to discuss the theoretical aspects of my research, providing new perspectives from outside of accelerator physics. I would also like to thank Professor Steven Lund. Email and conference correspondence opened up a dialogue that deepened my understanding of envelope modes and their importance for the community. A big thank you also to Dr. David Grote, Dr. Jean-Luc Vay, and Dr. Alex Friedman for their support of the WARP code.

I would also like to thank the remainder of the IREAP staff, including Edward Condon, Dorothy Brosius, Brian Quinn, Donald Martin, Leslie Delebar, Nancy Boone, and Kathryn Tracey for their help in administrative matters.

A big thank you to my parents, Bill and Debbie Stem, my sister and brother-in-law, Jaimy and Sean Gillow, and my nephew Zachary Gillow for their support and encouragement throughout the years. I would also like to thank all of my friends, too numerous to list, who have kept me sane and happy in a trying time. I would

not have been able to do this without you.

Finally, I would like to thank all of the scientists and engineers that have come before me. For with a match forged from their hard work and dedication to science, they have lit the path of human understanding, as we ever strain to see through the darkness.

Table of Contents

List of Abbreviations

γ	Relativistic $1/\sqrt{(}1-\beta^2)$
β	Relativistic v/c
c	Speed of Light in Vacuum
$\tilde{\epsilon}$	rms Emittance
ϵ	$4\tilde{\epsilon}$
ϵ_0	Permittivity of Free Space
K	Generalized Perveance
$\kappa(s)$	Lattice Focusing Function
σ	Phase Advance
S	Lattice Period
x_{rms}	Horizontal rms Beam Radius
y_{rms}	Vertical rms Beam Radius
R_+	Breathing Mode Radius
R_-	Quadrupole Mode Radius
χ	Intensity Parameter

BPM	Beam Position Monitor
DMD	Digital Micromirror Device
FEL	Free-Electron Laser
FFT	Fast Fourier Transform
FODO	Alternating-Gradient Lattice Structure
FWHM	Full Width Half Maximum
HOM	Higher Order Mode
IREAP	Institute for Research in Electronics and Applied Physics
KO	Knockout Imaging Method
KV	Kapchinsky-Vladimirsky
PIC	Particle-in-Cell
PTSX	Paul Trap Simulator Experiment
RC	Ring Chamber
RMS	Root-Mean-Square
SHO	Simple Harmonic Oscillator
SWR	Standing Wave Ratio
UMER	University of Maryland Electron Ring
WCM	Wall Current Monitor
WLOG	Without Loss of Generality

Chapter 1: Introduction

1.1 Motivation

In accelerator physics, there are two axes of progress, the energy frontier and the intensity frontier. The energy frontier is concerned with the discovery of new physics at higher and higher energies. Currently the Large Hadron Collider (LHC) is working to make improvements to the standard model and determine whether supersymmetry is physical. In the intensity frontier, the goal is to increase a beam's particle density. This is important for several reasons. For colliders [1, 2], a greater density of particles enables more collisions per interaction, leading to rare events occurring on a reasonable time scale. For medical applications [3], a greater quantity of various radioisotopes can be produced from higher beam intensities, permitting the diagnosis and treatment of a greater number of patients. For industrial applications [4,5], higher density beams enables a more efficient irradiation and production. These are just a few examples reflecting the demand for higher intensity beams.

To achieve high-intensity beams, it is important to maintain beam control and beam quality. For example, the Large Hadron Collider (LHC) [2] seeks large charge per unit area (brightness) to increase the number of collisions per second (luminosity). In another example, the Dual-Axis Radiographic Hydrodynamic Test

(DARHT) Facility [6] requires a minimal beam spot size on their target to optimize their radiography. As a final example, free-electron lasers (FELs) [7, 8] require a small transverse beam phase space to improve the gain of the laser.

To monitor the quality of high-intensity beams, diagnostics are needed to measure emittance, a beam quality indicator. Ideally, these diagnostics should be non-invasive, so that the beam can be used after it is characterized and not destroy the diagnostic in the process. However, as outlined in the next section, emittance is notoriously difficult to measure for high-intensity beams.

1.2 A Brief History of Emittance Measurement

Traditional methods of measuring emittance are invasive and of limited accuracy. Such measurement methods include quadrupole scans, pepper pots, and wire scanners [9, 10].

In the quadrupole scan, the size of the beam is measured in response to the adjustment of an upstream quadrupole magnet strength. By populating a response matrix, the Courant-Snyder parameters β, γ, and α can be determined [11]. These parameters determine the size and orientation of the trace space ellipse described by

$$\gamma x^2 + 2\alpha x x' + \beta x'^2 = \epsilon_x, \tag{1.1}$$

where ϵ_x is the beam emittance. This is a non-invasive measurement, but it assumes that beam forms a trace space described by an ellipse, which is only true under linear forces. For intense beams, the measurement is associated with significant systematic

errors [10]. Intense beams are characterized by large amounts of space-charge or self-fields that distort particle trajectories and confound the emittance measurement.

In the pepper pot measurement, the beam is intercepted by mask with a lattice of small apertures. The apertures fragment the beam into an array of beamlets in which the remaining particles move in straight lines, no longer affected by self-forces. The transverse velocity spread of each beamlet is measured by a downstream fluorescent screen. The beam's trace space (and hence emittance) is reconstructed from images. The pepper pot method is often used for intense beams, but is an invasive technique. Additionally, a pepper pot mask has to be specifically constructed for each beam; the smaller the beam radius, the denser and smaller the arrayed apertures. This often leads to overlapping beamlet images causing uncertainty in the measurement. This can create problems when different beams are used in the same beam line.

In the wire scanner method, a wire is moved quickly across the beam that produces secondary particle shower. The shower is detected outside the vacuum chamber by a scintillator and photo-multiplier assembly. Transverse position and velocity are measured simultaneously from the photo-multiplier assembly, and emittance can then be determined. There are several limitations to this method. First, it is invasive. It also has a small signal-to-noise ratio. Finally, the wire needs to move quickly across the beam so that the measurement is limited to a single transverse beam slice. This leads to mechanical limitation when implementing this experimentally for short beam pulses.

1.3 The Envelope Mode Resonance Method

Collectively, particles define the beam envelope, the transverse edge of the beam bunch. The beam envelope is a dynamic structure that oscillates with the period of the accelerator lattice, the periodic arrangement of magnets used to focus the beam. Great care is taken to "match" the envelope to the lattice, such that the envelope flutter is periodic and has a constant average size. In intense beams, a beam disturbed from the matched case can cause a superposition of two oscillatory normal modes, the even or "breathing" mode and the odd or "quadrupole" mode. The frequencies of these modes scale with I/ϵ, where I is the beam current and ϵ is the beam emittance. If the beam current and the frequency of either mode can be measured, the emittance can be determined.

This dissertation details a successful measurement of the quadrupole envelope frequency by applying periodic, impulsed quadrupole perturbations to the beam using an rf-driven electric quadrupole specifically constructed for this task. After encountering several quadrupole perturbations, transverse beam slice images were collected using the combination of a fast camera (3 ns) and a fast phosphor screen. The rms beam sizes of these images determine the growth of the envelope due to the quadrupole perturbations. By tuning the rf frequency, the resonance structure of the envelope growth can be determined. The emittance can be inferred by identifying the frequencies of the resonances. This method is both sensitive and non-invasive.

1.4 Organization of the Dissertation

The focus of this dissertation is the experimental measurement of the quadrupole envelope mode frequency of an electron beam in a high-intensity circular accelerator. In chapter 2, it is shown how the dynamics of the quadrupole mode in an alternating-gradient lattice directly depends on the current and emittance, thus providing a way of determining the emittance from the mode frequency. The particle-core model of the beam is also introduced, and it is shown how envelope mode excitations can lead to resonant halo growth and beam degradation.

Chapter 3 introduces the experiment by deriving and simulating the delta-kicked harmonic oscillator. Theoretical results are compared to simulations with the introduction of a python-based code called WARP, detailing results from both its envelope solver and its particle-in-cell (PIC) code. Predicted values of quadrupole mode frequency from the envelope solver provide a metric for beam emittance. PIC codes show how halo formation is an indication of resonant envelope excitation over long beam lifetimes. In this way, halo measurement can be used as a possible envelope resonance diagnostic for high-intensity accelerators over long time scales.

Chapter 4 details the experimental apparatus used in this dissertation, as well as a detailed introduction to the University of Maryland Electron Ring (UMER). This includes the design, simulation, construction, bench tests, and installation of an rf-driven electric quadrupole and the resonant tank circuit that drives it. Great care is taken to theoretically and experimentally explore the fields generated by the quadrupole, and to ensure that it produces the fields calculated in chapter 3 for all

values of rf frequency.

Chapter 5 details the knockout method, the primary diagnostic used in this dissertation. A technical discussion of the fast phosphor screens, time delay mechanism, and gated camera is included. Other UMER diagnostics such as the wall current monitor (WCM) and beam position monitors (BPMs) are introduced.

Chapter 6 contains the experimental results and compares them with the simulations of chapter 3. It is shown that multi-turn resonant excitation of the quadrupole envelope mode provides a sensitive, non-invasive measurement of emittance. The conventional pinhole scan is also introduced, which is a method to directly determine the emittance at injection by using a small aperture and a downstream phosphor screen to measure the transverse velocity spread in the beam. This provides an experimental validation of the envelope resonance method.

Chapter 7 provides a summary of the dissertation along with ideas and suggestions for future research.

Appendix A discusses a steering method used to optimize the values of magnet current in UMER's injection line. Appendix B describes a technique used to match the UMER beam on the first turn with injection line quadrupole magnets using the steering solution of Appendix A.

Appendix C includes a discussion of the application of quadrupole pick-ups to measure beam size, and an explanation of the knockout method as the preferred diagnostic at UMER.

Chapter 2: Envelope Resonance in an Alternating-Gradient Lattice

To derive the theory of envelope resonance, it is first necessary to understand both the characteristic beam parameters and the time-evolution of charged particle beams. The underlying physics of these beams are described by the classical theory of electrodynamics [33].

2.1 Coordinate Definition

As a single particle moves with a velocity $v = \beta c$, it oscillates transversely about the beam's equilibrium orbit. In circular accelerators, it is convenient to employ a new coordinate system (x, y, s), where s is the co-moving longitudinal coordinate of the equilibrium orbit. Since a particle's longitudinal position is uniquely determined at a time t, the time-evolution of a particle's transverse motion $\dot{x} = \frac{dx}{dt}$ is expressed naturally in terms of its longitudinal spacial-evolution in the lab frame $x' = \frac{dx}{ds}$. The coordinate transformation is

$$\begin{aligned} \dot{x} &= \frac{dx}{ds}\frac{ds}{dt} = x'\dot{s}, \\ \ddot{x} &= \dot{x}'\dot{s} + x'\ddot{s} = x''\dot{s}^2. \end{aligned} \tag{2.1}$$

Here it is assumed that the longitudinal velocity is constant, thus $\ddot{s} = 0$. Since a particle's trajectory is slightly offset from the equilibrium orbit, it is not precisely

true that $v = \dot{s}$. Inspecting Figure 2.1, a geometrical argument is used to see that $v = \dot{s}\big(1 + \frac{x}{R}\big)$. However, since $x \ll R$, the paraxial approximation, $\dot{s} \approx v = \beta c$.

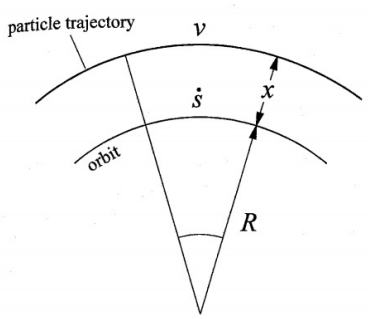

Figure 2.1: A particle's trajectory compared to the velocity of the longitudinal coordinate system of the beam's equilibrium orbit [34].

2.2 Fundamental Particle Beam Quantities

In order to discuss the dynamics of charged particle beams, certain fundamental quantities must be defined. The first quantity is the particle distribution function, or PDF. This function $f = f(x, y, s, x', y', s')$ describes the density of the beam at all points in 6-dimensional phase space. The paraxial approximation assumes the transverse and longitudinal dynamics are decoupled, and the 4-dimensional transverse PDF of the beam slice across the distance $\Delta s = s_2 - s_1$ is examined independently of the longitudinal dynamics. The new PDF is

$$f = f(x, y, x', y') = \int_{-\infty}^{+\infty} \int_{s_1}^{s_2} f(x, y, s, x', y', s') ds ds'. \tag{2.2}$$

The moments of this particle distribution function are defined as

$$M_{pqrs} = \iiiint_{beam} x^p y^q (x')^r (y')^s f(x, y, x', y') dx dy dx' dy'. \tag{2.3}$$

The number of particles in a given time slice is defined as the 0^{th} moment $M_{0000} \equiv N$. The 2^{nd} moments in x and y, M_{2000} and M_{0200}, are used to define the rms beam sizes

$$x_{rms}^2 = \langle x^2 \rangle = \frac{M_{2000}}{N}, \tag{2.4a}$$

$$y_{rms}^2 = \langle y^2 \rangle = \frac{M_{0200}}{N}. \tag{2.4b}$$

These values are important when describing the beam quality. Two measures of the beam quality are called the emittance ϵ and the brightness B. The rms emittance in x is given by

$$\tilde{\epsilon}_x^2 = \langle x^2 \rangle \langle x'^2 \rangle - \langle x x' \rangle^2. \tag{2.5}$$

This value is related to the area of trace space (x' vs. x) in a beam slice as shown in Figure 2.2, and it is conserved under linear forces ($F_x \propto x$). It is often useful to define the normalized rms emittance, $\tilde{\epsilon}_{n_x} = \beta\gamma\tilde{\epsilon}_x$, where γ is the relativistic $1/\sqrt{1-\beta^2}$ and β is the relativistic v/c. $\tilde{\epsilon}_{n_x}$ is preserved under longitudinal acceleration described by Liouville's Theorem [37]. In a particle accelerator, an increase in emittance over time generally indicates a deterioration of beam quality. **As explained in chapter 1, emittance is often difficult to measure in the lab, and this dissertation introduces a new method to measure it**.

Another measure of the beam quality is called the brightness. It is inversely proportional to the emittance and generally a measure of the density of phase space.

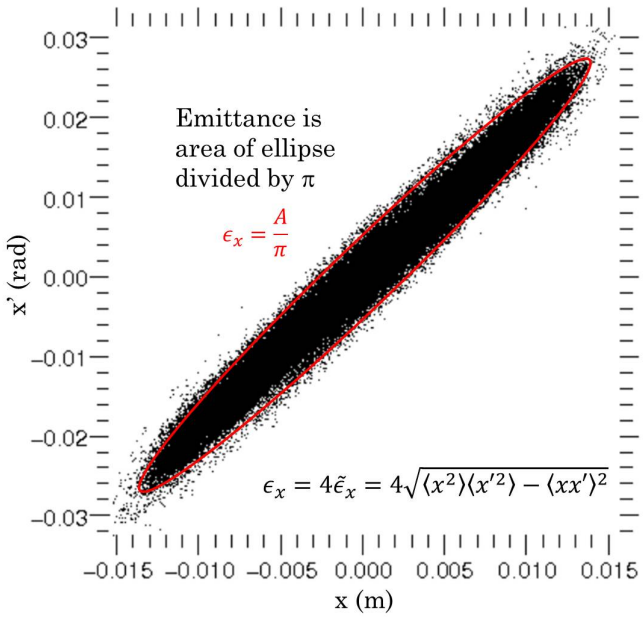

Figure 2.2: Emittance ϵ_x is defined as the area of a beam's transverse particle distribution in trace space. Though the ellipse evolves in time according to the magnet lattice, its area is preserved at all times under linear forces ($F_x \propto x$) [41].

The normalized average brightness is given by

$$\bar{B}_n = \frac{2I}{\pi^2 \epsilon_{n_x} \epsilon_{n_y}}, \tag{2.6}$$

where I is the beam current and $\epsilon_{n_x} = 4\tilde{\epsilon}_{n_x}$ for a beam with uniform particle density.

Two parameters that characterize the intensity of the beam are the generalized perveance K and the intensity parameter χ. K is a measure of the self-fields or space-charge intensity of the beam and is directly proportional to the beam current I. The generalized perveance is given by

$$K = \frac{I}{I_0} \frac{2}{(\beta\gamma)^3}. \tag{2.7}$$

I_0 is the characteristic current, defined by $I_0 = (4\pi\epsilon_0 mc^3)/q$. For electrons, $I_0 \approx 17$

kA. Since K is proportional to $(\beta\gamma)^{-3}$, space charge becomes negligible at high energies, where $\gamma \gg 1$. Proportional to the generalized perveance is the dimensionless intensity parameter χ, defined by

$$\chi = \frac{K}{k_0^2 a^2}, \tag{2.8}$$

where k_0 is the betatron oscillation wave number in the absence of space charge and a is the average beam radius. In the next section, these values will be used to describe beam transport in an alternating-gradient lattice.

2.3 Beam Transport in an Alternating-Gradient Lattice

In an alternating-gradient lattice structure, or FODO lattice, quadrupole magnets are used to focus the beam. Quadrupole magnets provide stronger focusing than axisymmetric fields. Because a quadrupole magnet focuses in one plane and defocuses in the other, the lattice geometry requires each sequential quadrupole magnet to be rotated by 90° with respect to the one before it. Since the beam envelope size is maximized as it passes through focusing fields and minimized as it passes through defocusing fields, The net result is a focused beam.

A particle moving through an alternating-gradient lattice will experience a trajectory described by

$$x'' + \kappa_x(s)x - \frac{2K}{X(X+Y)}x = 0, \tag{2.9a}$$

$$y'' + \kappa_y(s)y - \frac{2K}{Y(X+Y)}y = 0, \tag{2.9b}$$

where $\kappa_x(s)$ and $\kappa_y(s)$ are the lattice focusing functions. X and Y are the time-

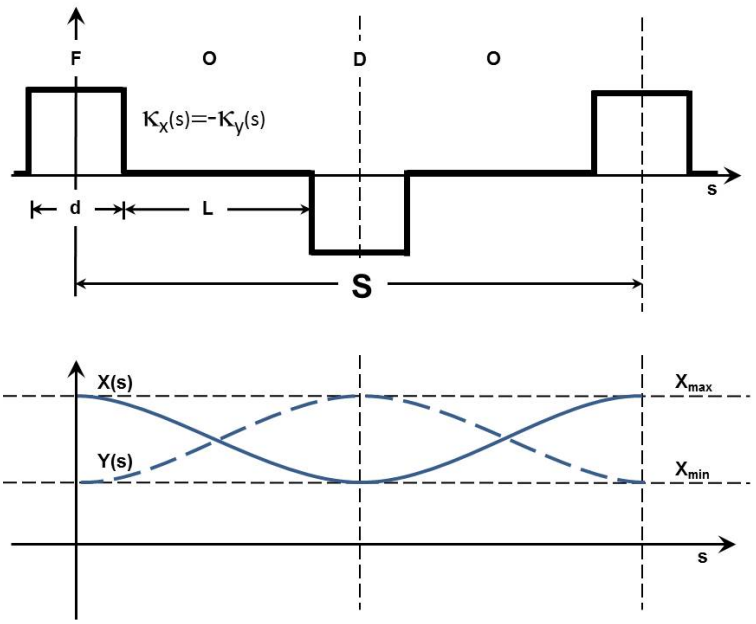

Figure 2.3: The alternating-gradient lattice focusing function plotted above the (matched) X and Y envelope functions.

dependent rms Kapchinsky-Vladimirsky (KV) envelope equations that evolve according to

$$X'' + \kappa_x(s)X - \frac{2K}{X+Y} - \frac{\epsilon_x^2}{X^3} = 0,, \tag{2.10a}$$

$$Y'' + \kappa_y(s)Y - \frac{2K}{X+Y} - \frac{\epsilon_y^2}{Y^3} = 0., \tag{2.10b}$$

where X and Y are defined by the rms beam sizes

$$X \equiv X_{rms}(s) = \sqrt{\langle X^2 \rangle_s}, \tag{2.11a}$$

$$Y \equiv Y_{rms}(s) = \sqrt{\langle Y^2 \rangle_s}. \tag{2.11b}$$

Space-charge decreases a charged particle's oscillation frequency through a force that opposes the lattice focusing force $\kappa_x x$. The phase advance is defined by the

amount a single particle oscillates over a lattice period. It is calculated by

$$\sigma = 360^\circ \frac{S}{\lambda}. \tag{2.12}$$

This value, measured in degrees, decreases with increasing space charge. Thus, the space-charge undepressed phase advance constant σ_0 is equivalent to the zero-current limit for an intense beam. It is useful to define the normalized phase advance σ/σ_0 as a measure of space-charge intensity. This dimensionless ratio is related to the beam parameters already defined by

$$\frac{\sigma}{\sigma_0} = \sqrt{1+u^2} - u, \tag{2.13}$$

where

$$u = \frac{KS}{2\epsilon\sigma_0}. \tag{2.14}$$

In this way, space-charge, measured by the normalized phase advance, scales by a factor of I/ϵ. Figure 2.4 shows the time-evolution of the matched rms envelope and single particle trajectories in an alternating-gradient lattice for depressed and undepressed phase advances akin to the values used in the experiment detailed in this dissertation.

In particle beams, it is often convenient to consider the collective dynamics of the beam as well as the motion of a single particle. This dissertation focuses on the dynamics of the envelope described by the equations 2.10a and 2.10b. The theory of envelope dynamics was first derived in 1959 by Kapchinsky and Vladimirsky [12] and later generalized to the rms case in 1971 by Lapostolle [13] and Sacherer [14]. The generalization provided the freedom to explore any non-uniform charge distribution

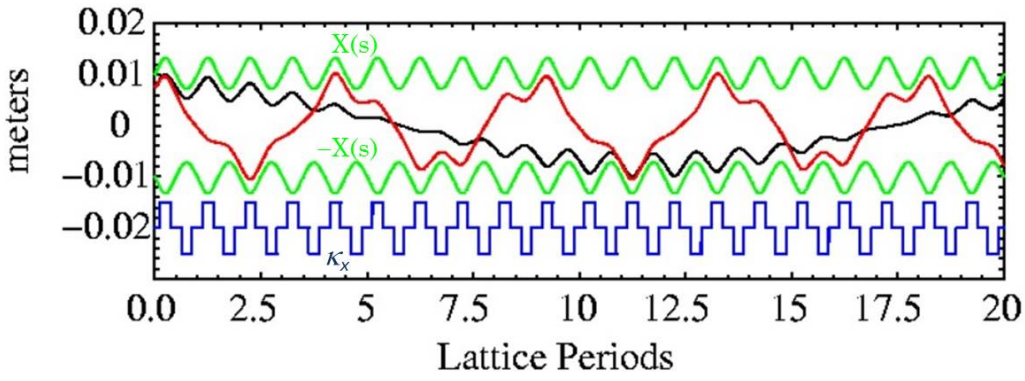

Figure 2.4: Depressed (black) and undepressed (red) single particle trajectories plotted within the matched envelope $X(s)$ in the plane $y = 0$. This alternating-gradient lattice has phase advances $\sigma_0 = 80°$ and $\sigma = 16°$ [42].

with elliptical symmetry. A conceptual drawing of a collection of particles that make up the beam envelope is shown in Figure 2.5. In the next section, the mismatch consequences of these equations will be examined.

2.4 Perturbations on the Matched KV Envelope Solutions

Although there are no known analytic solutions to the envelope modes in an alternating-gradient lattice, the smooth approximation provides a simplified approach that results in an analytic solution. This solution is presented and then followed by an analysis of the more complex alternating-gradient lattice structure.

2.4.1 The Smooth Approximation

In the focusing channel of the smooth approximation, the focusing functions $\kappa_x(s)$ and $\kappa_y(s)$ depicted in Figure 2.3 are replaced by the constant $\kappa_0 = k_0^2$. The

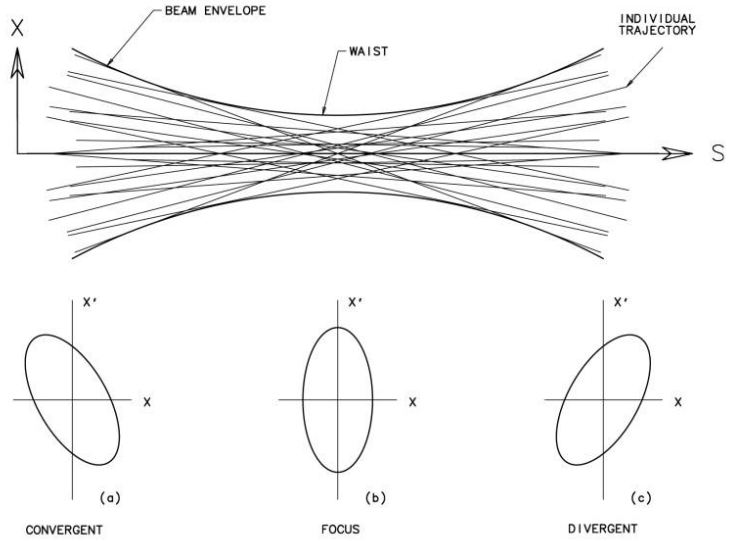

Figure 2.5: Conceptual drawing of a beam passing through a waist, plotted with snapshots of its corresponding trace space ellipse [43].

undepressed wave number (or spatial frequency) k_0 is defined as

$$k_0^2 = \frac{\sigma_0^2}{S^2}, \tag{2.15}$$

where σ_0 is the phase advance of particle oscillations in the absence of space charge and S is the lattice period. In a matched beam, the axisymmetric property of the smooth approximation implies that the average envelope functions $\bar{X}(s)$ and $\bar{Y}(s)$ be equal to the matched radius $\bar{R} = \sqrt{\epsilon/k} = \sqrt{\epsilon S/\sigma}$, where $\epsilon = \tilde{\epsilon}_x = \tilde{\epsilon}_y$ for a matched beam. In this case, the envelope equation becomes

$$k_0^2 \bar{R} - \frac{K}{\bar{R}} - \frac{\epsilon^2}{\bar{R}^3} = 0. \tag{2.16}$$

With a mismatch, $\bar{X}$ and $\bar{Y}$ differ from $\bar{R}$ and the envelope equations become

$$\bar{X}'' + k_0^2 \bar{X} - \frac{2K}{\bar{X} + \bar{Y}} - \frac{\epsilon^2}{\bar{X}^3} = 0, \tag{2.17a}$$

$$\bar{Y}'' + k_0^2 \bar{Y} - \frac{2K}{\bar{X} + \bar{Y}} - \frac{\epsilon^2}{\bar{Y}^3} = 0. \tag{2.17b}$$

Now that the transverse dimensions are considered independently, distinct perturbations are applied separately to each envelope function. These perturbations reflect the degree of the mismatch, and are written as

$$\bar{X}(s) = \bar{R} + \delta X(s), \tag{2.18a}$$

$$\bar{Y}(s) = \bar{R} + \delta Y(s), \tag{2.18b}$$

where $\delta X, \delta Y \ll \bar{R}$. Substituting 2.18 into 2.17 and keeping only the first order terms of the expansion, the new envelope equation is

$$\delta X'' + A\delta X + B\delta Y = 0, \tag{2.19a}$$

$$\delta Y'' + A\delta Y + B\delta X = 0, \tag{2.19b}$$

where

$$A = \frac{3\sigma_0^2 + 5\sigma^2}{2S^2}, \tag{2.20a}$$

$$B = \frac{\sigma_0^2 - \sigma^2}{2S^2}. \tag{2.20b}$$

These equations still have coupled transverse motion. A change of coordinates will uncouple the transverse modes into two oscillatory equations of motion. These new coordinates are defined by

$$R_+ \equiv \delta X + \delta Y, \tag{2.21a}$$

$$R_- \equiv \delta X - \delta Y. \tag{2.21b}$$

The new equations of motion are

$$R''_+ + k_+^2 R_+ = 0, \tag{2.22a}$$

$$R''_- + k_-^2 R_- = 0. \tag{2.22b}$$

Equation 2.22a describes the time evolution of the even or "breathing" mode. Equation 2.22b describes the time evolution of the odd or "quadrupole" mode. Their wave numbers are

$$k_+ = \sqrt{2k_0^2 + 2k^2}, \tag{2.23a}$$

$$k_- = \sqrt{k_0^2 + 3k^2}, \tag{2.23b}$$

and their phase advances are

$$\sigma_+ = \sqrt{2\sigma_0^2 + 2\sigma^2}, \tag{2.24a}$$

$$\sigma_- = \sqrt{\sigma_0^2 + 3\sigma^2}. \tag{2.24b}$$

These phase advances occur for a mismatch that reflects the pure mode launching conditions. All other cases are expressed as a superposition of these two modes. The pure modes are plotted in Figure 2.6 as a function of the normalized phase advance. At the zero space-charge limit where σ/σ_0 approaches 1, the envelope mode phase advances converge to twice the phase advance of an undepressed particle oscillation.

A more thorough analysis in the smooth approximation [16] studies the effect of perturbations applied to the generalized perveance K, the emittance ϵ and the focusing function κ. The resulting envelope mode frequencies and phase advances remain the same.

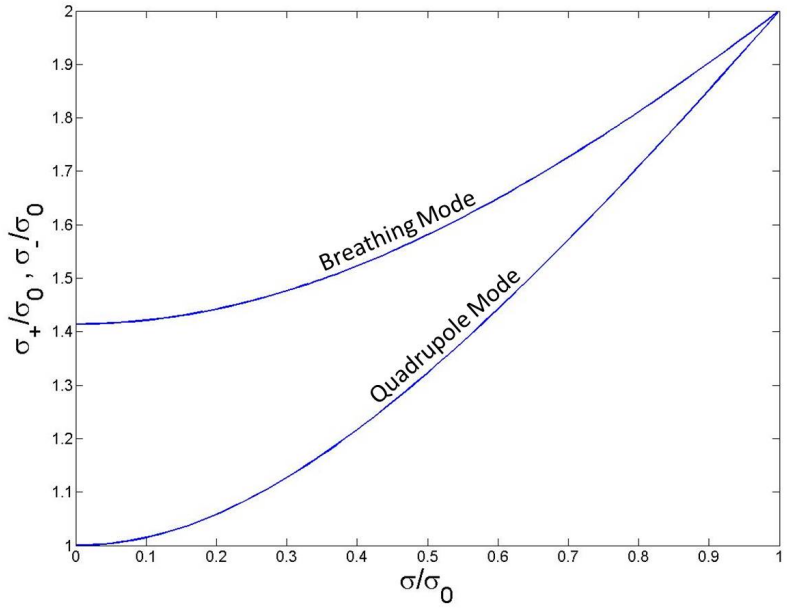

Figure 2.6: Normalized envelope mode phase advances plotted as a function of σ/σ_0 in the smooth approximation.

Equation 2.24 shows the envelope mode dependence on the normalized phase advance, σ/σ_0. Equations 2.13 and 2.14 characterize the dependence of the normalized phase advance on current (through the generalized perveance) and emittance. Chapter 3 will quantify the emittance dependence in high-intensity circular accelerators. This explicit dependence of envelope mode phase advance on emittance leads to a novel emittance diagnostic.

2.4.2 Envelope Modes in an Alternating-Gradient Lattice

For an alternating-gradient lattice (FODO), the analysis becomes more complicated and there is no closed form solution. A numerical solution is reached by repeating the perturbation analysis in the previous section for rms envelope equa-

tions with time-dependent focusing functions.

Applying mismatch perturbations to the matched envelopes X_0 and Y_0 analogous to equation 2.18, the new system of equations becomes

$$\delta X'' + a_{1x}(s)\delta X + a_0(s)\delta Y = 0, \tag{2.25a}$$

$$\delta Y'' + a_{1y}(s)\delta Y + a_0(s)\delta X = 0, \tag{2.25b}$$

where

$$a_0(s) = \frac{2K}{(X_0(s) + Y_0(s))^2}, \tag{2.26a}$$

$$a_{1x}(s) = \kappa_{x0}(s) + \frac{3\epsilon^2}{X_0^4(s)} + a_0(s), \tag{2.26b}$$

$$a_{1y}(s) = \kappa_{y0}(s) + \frac{3\epsilon^2}{Y_0^4(s)} + a_0(s). \tag{2.26c}$$

This coupled system of second order differential equations can be written in matrix form as a system of four first order differential equations

$$\delta \mathbf{R}'(s) = \mathbf{A}(s) \cdot \delta \mathbf{R}(s), \tag{2.27}$$

where

$$\delta \mathbf{R} = \begin{pmatrix} \delta X \\ \delta X' \\ \delta Y \\ \delta Y' \end{pmatrix}, \tag{2.28}$$

and

$$\mathbf{A}(s) = \begin{pmatrix} 0 & 1 & 0 & 0 \\ -a_{1x}(s) & 0 & -a_0(s) & 0 \\ 0 & 0 & 0 & 1 \\ -a_0(s) & 0 & -a_{1y}(s) & 0 \end{pmatrix}. \tag{2.29}$$

If the emittance, generalized perveance, and focusing functions are free to be perturbed, an additional vector,

$$\delta\mathbf{P} = \begin{pmatrix} 0 \\ -\delta\kappa_x + 2\frac{\delta K}{X_0+Y_0} + 2\frac{\epsilon_x\delta\epsilon_x}{X_0^3} \\ -\delta\kappa_y + 2\frac{\delta K}{X_0+Y_0} + 2\frac{\epsilon_y\delta\epsilon_y}{Y_0^3} \end{pmatrix}, \tag{2.30}$$

is added to the right-hand side of equation 2.27. This vector represents driving perturbations of the envelope modes. Since only normal mode oscillations are being considered in this dissertation, $\delta\mathbf{P} = 0$ without loss of generality, as only the homogeneous solution contributes.

Let $\delta\mathbf{R}(s)$ be the homogeneous solution to equation 2.27. Due to the periodicity of $\mathbf{A}(s)$, Floquet's theorem implies the existence of a transfer matrix that advances the solution by a lattice period S. By choosing appropriate initial conditions $\delta\mathbf{R}(s_0)$ and iterating through the lattice, a numerical solution is

$$\delta\mathbf{R}(s_0 + nS) = \mathbf{M}(s_0 + S|s_0)^n \cdot \delta\mathbf{R}(s_0), \tag{2.31}$$

where $\mathbf{M} \equiv \mathbf{M}(s_0+S|s_0)$ represents the 4x4 transfer matrix across one lattice period for any initial starting position defined as $s = s_0$. The eigenvalues and eigenvectors of $\mathbf{M}$,

$$\mathbf{M}(s_0 + S|s_0) \cdot \mathbf{E}_n(s_0) = \lambda_n\mathbf{E}_n(s_0), \tag{2.32}$$

provide information about the stability and launching conditions of the envelope modes. The eigenvectors depend on the initial condition $s = s_0$ and are normalized according to $\mathbf{E}_n \cdot \mathbf{E}_n^* = 1$. Because equation 2.27 is real and Hamiltonian, $\mathbf{M}$ is a

real, symplectic matrix. The resulting eigenvalues occur in complex conjugate and reciprocal pairs. Four symmetry classes arise from equation 2.32, corresponding to different stability conditions in the envelope modes. This dissertation is concerned with the stable case; the other cases only exist in alternating-gradient lattices for $\sigma_0 > 90^\circ$ [11, 15, 16, 37], whereas the UMER lattice is fixed at $\sigma_0 = 76^\circ$ to avoid instabilities.

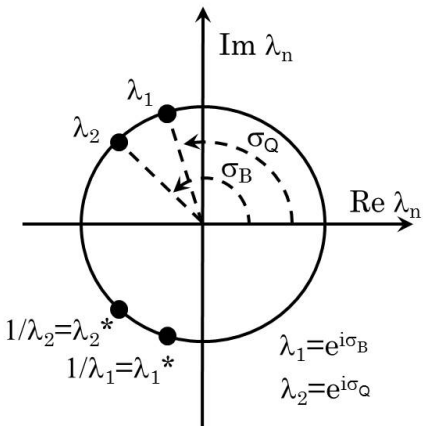

Figure 2.7: Polar representation of the stable symmetry class solution for equation 2.32. All eigenvalues lie on the unit circle, with angles corresponding to the phase advances of each mode. The subscripts B and Q represent the breathing and quadrupole modes, respectively, in an alternating gradient lattice for $\sigma_0 < 90^\circ$.

Due to the complex nature of the alternating-gradient lattice envelope mode coordinates, the modes are not easily decoupled, and exciting a pure mode requires careful initial (or launching) conditions that have a sensitive dependence on σ_0. Numerical studies [16] have shown that for a FODO lattice of $\sigma_0 = 76^\circ$ as for UMER, mid-quad excursion ratios ($\delta X/\delta Y$) are approximately 2.1 and -1.9 for the breathing and quadrupole modes, respectively. A picture of the pure modes from

reference [15] is shown in Figures 2.8 and 2.9.

Even though the alternating-gradient lattice solution is more complicated than the smooth approximation in terms of the evolution of mode coordinates δX and δY, the smooth approximation gives nearly identical frequencies. Therefore, equation 2.24 is used to accurately predict mode phase advances in an alternating-gradient lattice [37]. In the next section, it will be shown how the frequencies of these modes can lead to halo growth and beam degradation.

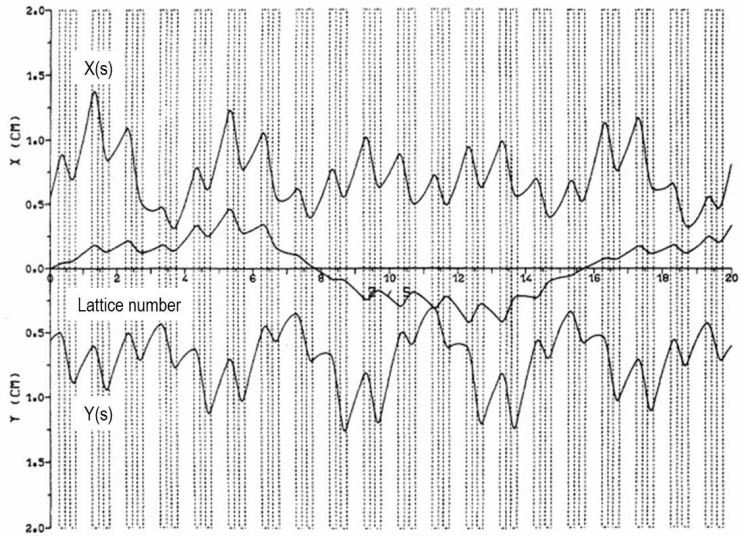

Figure 2.8: X and Y envelope and single particle trajectories for a pure breathing envelope mode mismatch in an alternating-gradient lattice for $\sigma_0 = 60^\circ$ and $\sigma = 21^\circ$ [15].

2.5 Halo Resonance Conditions

Halo generation degrades beam quality. It can cause beam current loss, emittance growth, and reduced beam brightness. Beam quality is crucial to a high

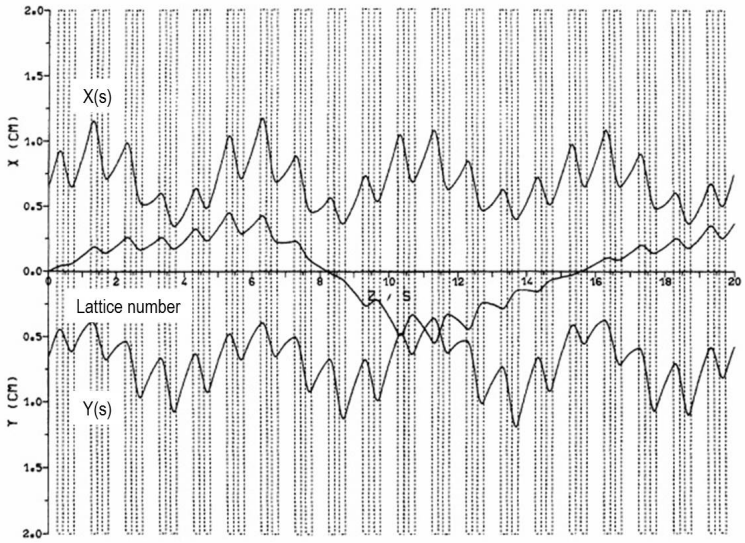

Figure 2.9: X and Y envelope and single particle trajectories for a pure quadrupole envelope mode mismatch in an alternating-gradient lattice for $\sigma_0 = 60^\circ$ and $\sigma = 21^\circ$ [15].

intensity particle accelerator.

In the particle-core model of beam halo [45], a halo particle is defined as a particle that has an amplitude of oscillation that exceeds the core radius of a uniform, oscillating core. These particles experience a different space-charge force depending on whether they are inside or outside of the core. For a particle oscillating in the horizontal plane of a uniform density beam,

$$F_{sc} = \begin{cases} \frac{Kx(s)}{X(s)^2}, & |x(s)| < X(s) \\ \\ \frac{K}{x(s)}, & |x(s)| \geq X(s) \end{cases} \tag{2.33}$$

These space-charge forces are directed away from the center of the core. As a result, a particle that moves toward the center of the core is decelerated; a particle moving away from the center of the core is accelerated. In the case of an envelope

mode, a halo particle experiences a net space-charge impulse as it enters and exits the core at different core radii. By integrating equation 2.33, it is seen that a particle gains the most energy if it enters the core when $X(s)$ is a maximum and exits the core when $X(s)$ is a minimum. This condition becomes resonant when it occurs repeatedly, as shown in Figure 2.10.

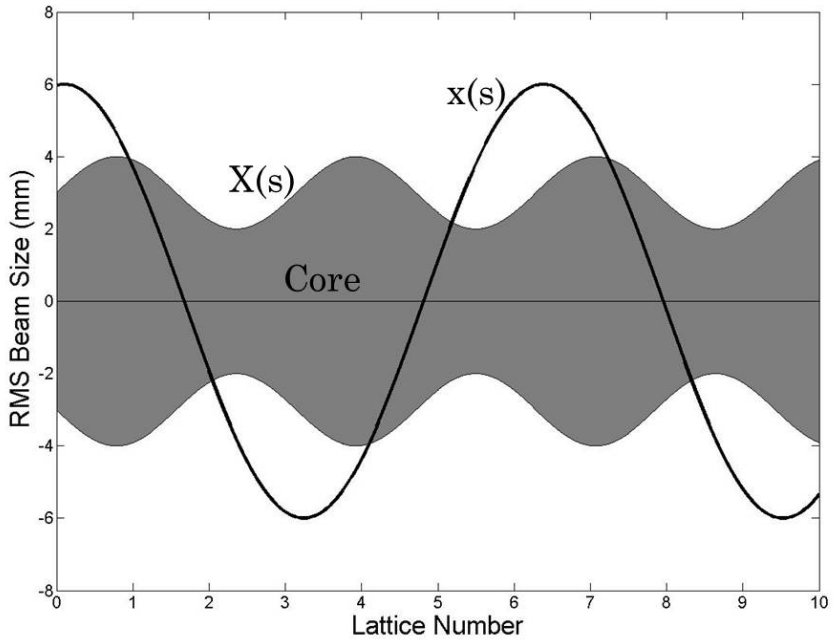

Figure 2.10: Conceptual drawing of a halo particle oscillating under a resonant condition.

For a particle to continually gain energy in this way, it must oscillate at half of an envelope mode frequency,

$$k_{\beta,\mathrm{res}} = \frac{1}{2} k_{B,Q}. \tag{2.34}$$

As a halo particle oscillates with an amplitude larger than the core, it experiences less of a space-charge depression, which in turn increases its wave number k_β.

As shown in Figure 2.11, a particle in the core oscillates at a frequency too small to meet the resonance condition, while a particle of large amplitude will oscillate at a frequency that is too large. At a specific amplitude between these extremes, the resonant amplitude, a halo particle will experience a nonlinear parametric resonance that increases its energy and its amplitude. However, this resonant amplitude growth causes the wave number of the particle to fall out of the resonant condition, limiting resonant growth [46].

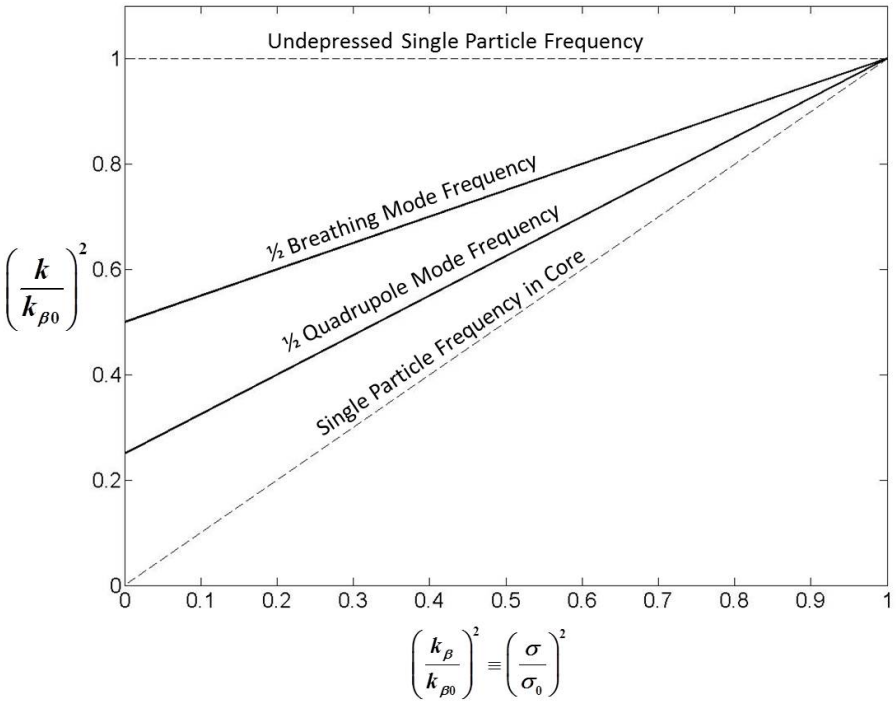

Figure 2.11: Particle oscillation frequencies plotted with the 1/2-frequency envelope modes. The resonance condition is satisfied when particles have a large enough amplitude to oscillate at half the value of an envelope mode frequency.

In this dissertation, the experimental characterization of the resonance struc-

ture of the quadrupole envelope mode in an alternating-gradient lattice is described. The results provide a greater insight to future accelerator projects that desire to minimize beam loss and maximize beam quality. In Chapter 3, the onset of beam halo formed by an envelope mode oscillation is used as an emittance diagnostic for high-intensity circular accelerators with long beam lifetimes.

Chapter 3: Envelope Resonance Simulations

The primary simulation tool used by UMER scientists is a python-based deck called WARP [47], that contains both an envelope solver and a particle-in-cell (PIC) code that accounts for space-charge in intense beams. In this chapter, results from both the envelope solver and PIC codes are examined, along with the results of a reductionist model of envelope resonance.

3.1 Reductionist Model

3.1.1 Analytic Solution

In physics, it often helps to simplify a complex system by using a reductionist model to highlight the fundamental dynamics. In this particular case, the quadrupole envelope mode equation of motion in the smooth approximation (equation 2.22b) is linearized as a 1-dimensional simple harmonic oscillator. Even though the coordinate R_- includes both transverse dimensions as shown in equation 2.21b, the quadrupole perturbation applied to the electron beam couples the two coordinates. Since the beam only experiences the perturbation on a short (0.86 ns) time scale once per turn (197 ns), the driving term in the system is approximated as a

"delta-kicked" simple harmonic oscillator described by

$$\ddot{R} + \omega_0^2 R = A_0 cos(\omega t + \phi) \sum_n \delta(t - nT), \tag{3.1}$$

where R is defined as R_- for the quadrupole mode and R_+ for the breathing mode. This is written in exponential form

$$\ddot{R} + \omega_0^2 R = \tilde{A}_0 Re[e^{i\omega t}] \sum_n \delta(t - nT), \tag{3.2}$$

where

$$cos(\omega t + \phi) = Re[e^{i(\omega t + \phi)}], \tag{3.3}$$

and

$$\tilde{A}_0 = A_0 e^{i\phi}. \tag{3.4}$$

Since the transient behavior of the system is not relevant to this dissertation, equation 3.2 is solved with Fourier analysis. The Fourier representation of the solution is

$$\hat{R}(\omega') = \int_{-\infty}^{\infty} R(t) e^{-i\omega' t} dt. \tag{3.5}$$

Integrating equation 3.2 over all time, the equation of motion is expressed in terms of the Fourier solution as

$$-\omega'^2 \hat{R} + \omega_0^2 \hat{R} + \tilde{A}_0 \sum_n e^{i\omega n T} e^{-i\omega' n T} = 0. \tag{3.6}$$

Solving for $\hat{R}$,

$$\hat{R}(\omega') = \frac{\tilde{A}_0 \sum_n e^{-inT(\omega' - \omega)}}{\omega'^2 - \omega_0^2} = \frac{\tilde{A}_0 \sum_n e^{-inT(\omega' - \omega)}}{(\omega' - \omega_0)(\omega' + \omega_0)}. \tag{3.7}$$

Taking the inverse Fourier transform,

$$R(t) = \frac{1}{2\pi} \int_{-\infty}^{\infty} \hat{R}(\omega') e^{i\omega' t} d\omega', \tag{3.8}$$

$$R(t) = \frac{\tilde{A}_0}{2\pi} \sum_n \int_{-\infty}^{\infty} \frac{e^{-inT(\omega'-\omega)} e^{i\omega' t}}{(\omega' - \omega_0)(\omega' + \omega_0)} d\omega', \tag{3.9}$$

$$R(t) = \frac{\tilde{A}_0}{2\pi} \sum_n e^{in\omega T} \int_{-\infty}^{\infty} \frac{e^{i\omega'(t-nT)}}{(\omega' - \omega_0)(\omega' + \omega_0)} d\omega'. \tag{3.10}$$

This integral is solved with a contour integration around the poles $\omega' = \omega_0$ and $\omega' = -\omega_0$. For $t - nT > 0$, the contour closes above as shown in Figure 3.1. Applying the residue theorem for $t > nT$, the integral in 3.10 becomes

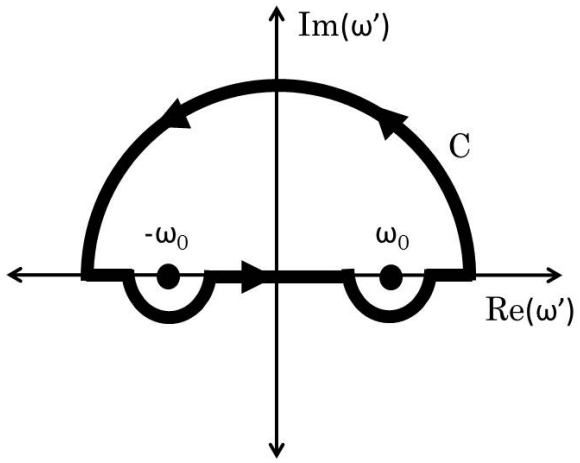

Figure 3.1: Contour integration.

$$2\pi i \left[\frac{1}{2\omega_0} e^{i\omega_0(t-nT)} + \frac{1}{-2\omega_0} e^{-i\omega_0(t-nT)} \right] = -\frac{2\pi}{\omega_0} sin(\omega_0(t - nT)). \tag{3.11}$$

If $t - nT < 0$, then $R(t) = 0$, so instead of summing over all n, the sum is now over $n < t/T$. Taking the real part of $e^{i(n\omega T + \phi)}$, the solution of equation 3.2 is

$$R(t) = -\frac{A_0}{\omega_0} \sum_{n<t/T} cos(n\omega T + \phi) sin(\omega_0(t - nT)). \tag{3.12}$$

3.1.2 Steady State Behavior

As $n \to \infty$, the behavior of the delta-kicked simple harmonic oscillator converges to a steady state solution. Assuming the quad-kick has been applied for a sufficient amount of time in the past, the solution 3.12 is written as

$$R(t) = -\frac{A_0}{\omega_0} \sum_{n=-\infty}^{\infty} cos(n\omega T + \phi) sin(\omega_0(t - nT)). \tag{3.13}$$

Writing this in exponential form and re-arranging terms,

$$\begin{aligned} R(t) = -\frac{A_0}{4i\omega_0} \sum_{n=-\infty}^{\infty} (& e^{i(\omega-\omega_0)nT} e^{i(\omega_0 t+\phi)} - e^{-i(\omega-\omega_0)nT} e^{-i(\omega_0 t+\phi)} \\ & - e^{i(\omega-\omega_0)nT} e^{-i(\omega_0 t-\phi)} + e^{-i(\omega-\omega_0)nT} e^{i(\omega_0 t-\phi)}). \end{aligned} \tag{3.14}$$

The sum across infinity implies that the solution can be written in terms of the Dirac comb,

$$\mathbf{III}_T(t) \equiv \sum_{n=-\infty}^{\infty} \delta(t - nT) = \frac{1}{T} \sum_{n=-\infty}^{\infty} e^{2\pi i n t/T}. \tag{3.15}$$

From the terms in equation 3.14,

$$\sum_{n=-\infty}^{\infty} e^{\pm i(\omega-\omega_0)nT} = \frac{2\pi}{|\omega - \omega_0|} \sum_{n=-\infty}^{\infty} \delta(T - n\tau_-) = \tau_- \mathbf{III}_{\tau_-}(T), \tag{3.16a}$$

$$\sum_{n=-\infty}^{\infty} e^{\pm i(\omega+\omega_0)nT} = \frac{2\pi}{\omega + \omega_0} \sum_{n=-\infty}^{\infty} \delta(T - n\tau_+) = \tau_+ \mathbf{III}_{\tau_+}(T), \tag{3.16b}$$

where

$$\tau_- \equiv \frac{2\pi}{|\omega - \omega_0|}, \tag{3.17}$$

$$\tau_+ \equiv \frac{2\pi}{\omega + \omega_0}. \tag{3.18}$$

Substituting equations 3.16a and 3.16b into equation 3.14,

$$R(t) = -\frac{A_0}{2\omega_0} [\tau_- \mathbf{III}_{\tau_-}(T) sin(\omega_0 t + \phi) + \tau_+ \mathbf{III}_{\tau_+}(T) sin(\omega_0 t - \phi)]. \tag{3.19}$$

Note that the resonance conditions occur for $\omega \pm \omega_0 = 2\pi n/T$, which provides a lattice of resonances for the three frequencies in the system: the driving perturbation frequency ω, the natural frequency ω_0, and frequency at which the perturbation occurs $\Omega \equiv 2\pi/T$. For $\Omega/2\pi = 5$ MHz, a plot of the resonance structure lattice is shown in Figure 3.2.

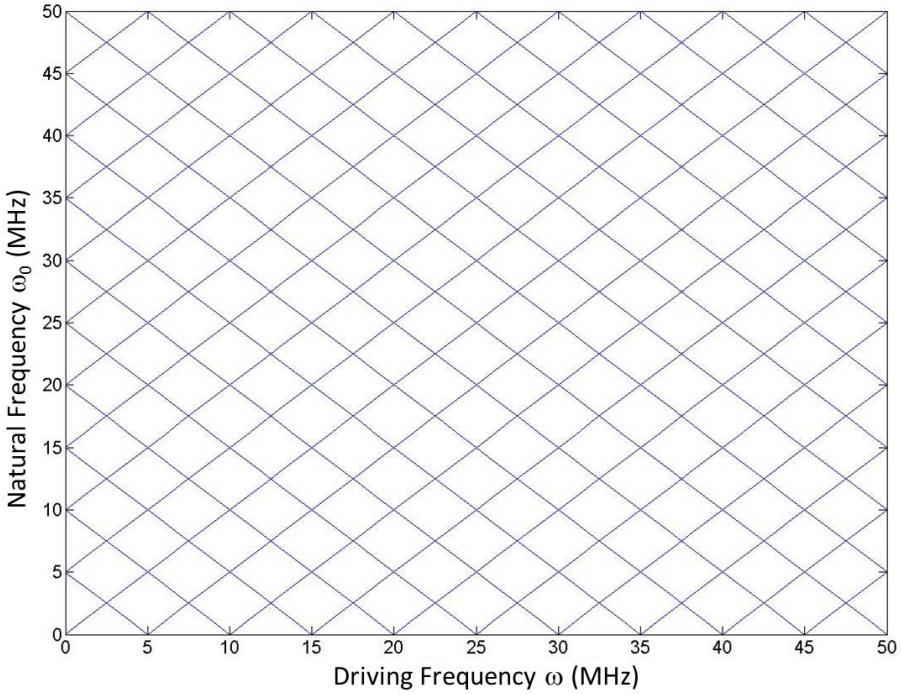

Figure 3.2: Resonance structure lattice showing lines of resonance for varying values of driving frequency and natural frequency for $\Omega/2\pi = 5$ MHz.

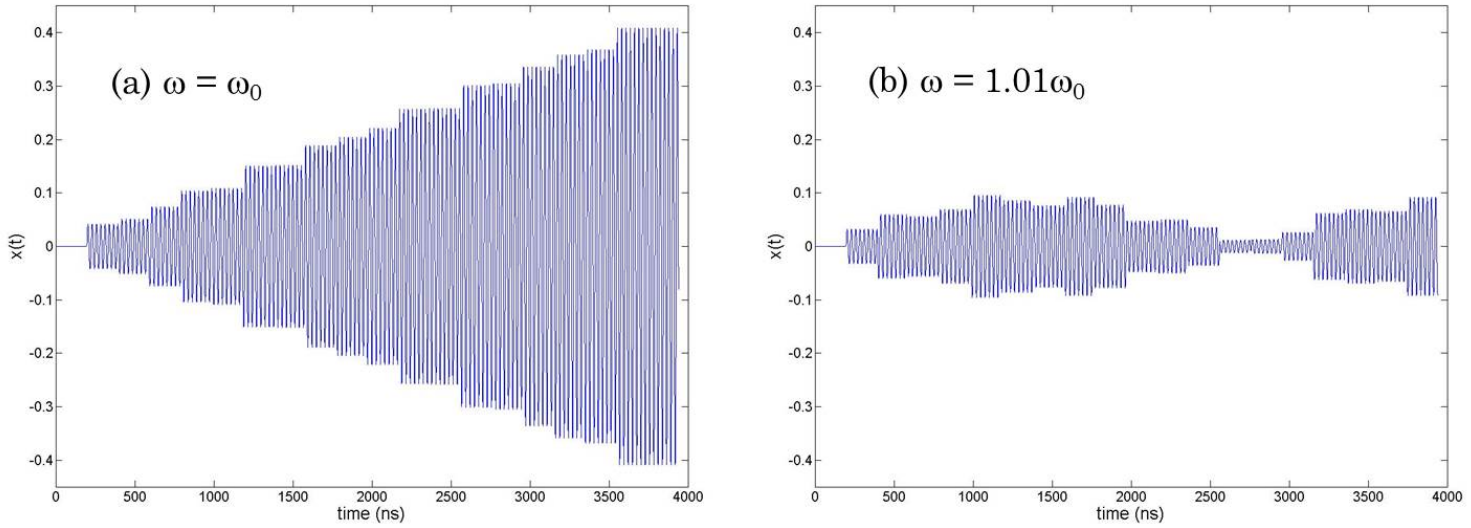

Figure 3.3: Leapfrog integration of the reductionist model for $T = 197$ ns, $\phi = 0$, $A_0 = 1e^{-2}$, and (a) $\omega = \omega_0$ and (b) $\omega = 1.01\omega_0$. These plots represent trajectory behavior due to 19 periodic impulses, resulting in (a) resonant growth and (b) beating.

3.1.3 Leapfrog Simulations of the Reductionist Model

The differential equation 3.2 was integrated using the leapfrog algorithm. This algorithm employs half-integer time steps for velocity so that phase space is preserved. To match experimental conditions, $T = 197$ ns. After integrating for 20 turns, the resulting behavior is shown in Figure 3.3.

For the experiment described in this dissertation, the diagnostic chamber is fixed at a single location in the ring. This means that a graph such as Figure 3.3 cannot be recovered experimentally. It is possible to determine where there is resonant growth from a fixed location by scanning through different phases ϕ. Then the amplitude of the resulting sine wave (e.g. Figure 3.4) is a measure of the growth in the envelope as a function of turn.

Using the same diagnostic location as Figure 3.4, the envelope growth is plotted as a function of driving frequency ω for $\omega_0/2\pi = 37$ MHz. This is shown in Figure 3.5. This result matches predictions from the resonance structure lattice in Figure 3.2.

After 19 quad-kicks, there are clear, well-defined resonance peaks for a given value of ω_0. Consistent with the steady state solution of equation 3.19, as $n \to \infty$, the peaks become narrower and taller, resulting in a delta function wave train.

3.2 Introduction to WARP

WARP [47] is a python-based code used by accelerator physicists to account for space-charge dynamics in a beam. This code contains both an envelope solver and

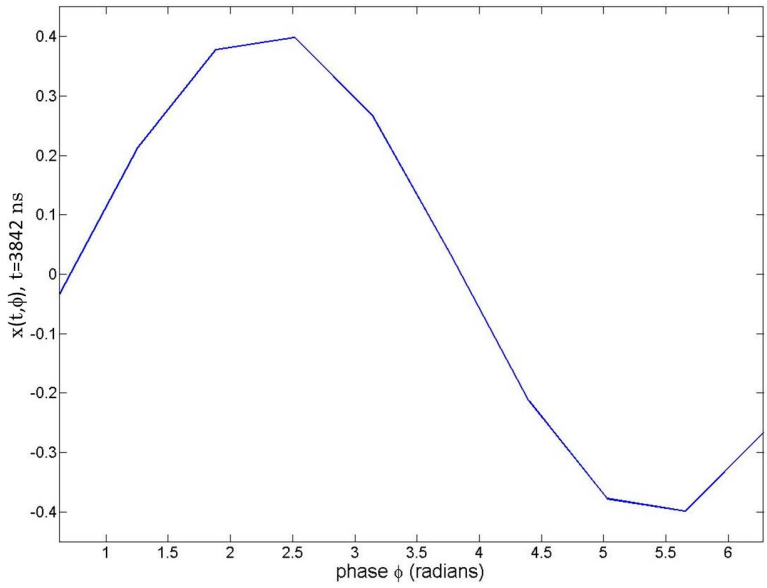

Figure 3.4: Plot of x(t) for $\omega = \omega_0$ over a ϕ phase scan at the location $t = 19.5T = 3842$ ns (n=19).

a particle-in-cell (PIC) code. The envelope solver integrates equation 2.10 giving numerical values of the envelope evolution in the presence of space-charge. This is traditionally used to provide a quick, matched envelope solution for the beam parameters used in the PIC code. However, it is used in this dissertation as an alternating-gradient simulation of the mode resonances.

The PIC code incorporates three descriptions: a 3-D description, an axisymmetric description, and a transverse slice description. The transverse slice description is used in this dissertation to show the growth of halo as a function of longitudinal displacement for a mode-excited beam.

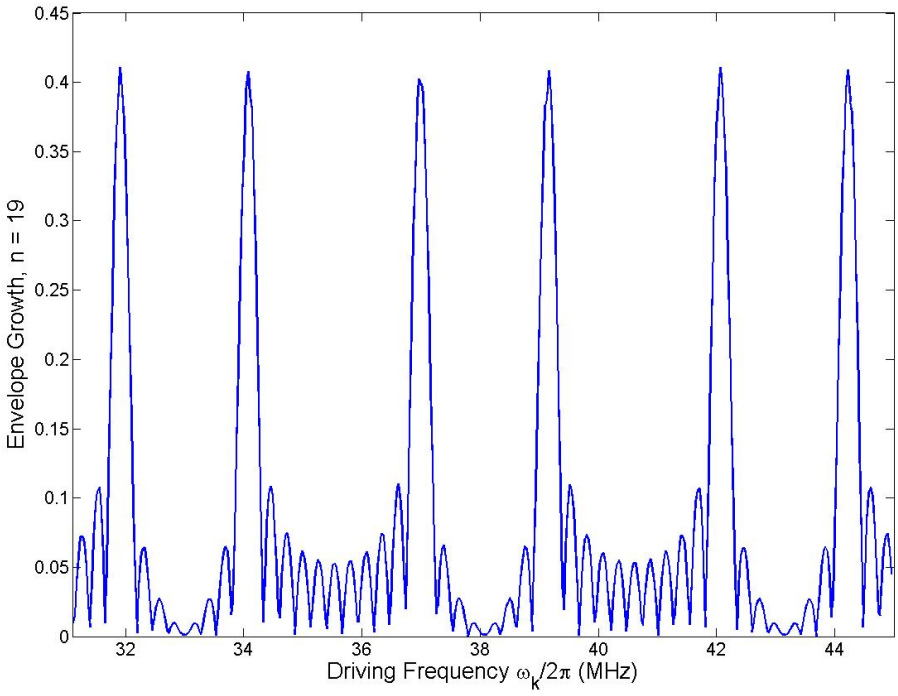

Figure 3.5: Envelope growth as a function of driving frequency $\omega/2\pi$ for $n = 19$ and $\omega_0/2\pi = 37$ MHz. The spacing between resonance peaks match the results of the resonance structure lattice shown in Figure 3.2.

3.3 Envelope Solver

3.3.1 Matching the Beam

A matched beam solution as shown in Figure 2.3 can be found through an iterative method. Using the envelope solver, the rms envelope equations are integrated over one lattice period S. Starting at the center of a quadrupole magnet, the initial envelope velocities x_0' and y_0' are 0. Thus, only the initial envelope displacements x_0 and y_0 are unknown, which are equivalent to the values of the envelope

displacements at the end of the lattice period. New values of x_0 and y_0 are found by averaging over the initial and final envelope displacement values. Using these new initial values, the envelope is again plotted for a lattice period in an iterative process. Generally, the matched envelope solution converges quickly, using an iteration number on the order of $n = 7$.

3.3.2 Mode Frequency Characterization

Applying an initial mismatch to the matched envelope displacements, the quadrupole and breathing modes are excited independently. These pure modes are simulated by applying mismatches proportional in x and y. The envelope is integrated over the equivalent of 1000 turns at UMER. The alternating-gradient lattice oscillations are sampled at a rate of once per lattice period. The mode frequencies are found by applying a fast fourier transform (FFT) to the results. For the 21 mA beam, the frequency as a function of mismatch is shown in Figures 3.6 and 3.7.

For a 10% mismatch, the frequencies predicted for four UMER mask settings are shown in Table 3.1. These frequencies in terms of their phase advances are plotted in Figure 3.8 alongside the predicted frequencies in the smooth approximation (Figure 2.6).

3.3.3 Modeling the Experiment

In simulation, a turn in UMER can be modeled as 36 FODO lattice periods. After each simulated turn, a sinusoidally varying impulsed perturbation is applied

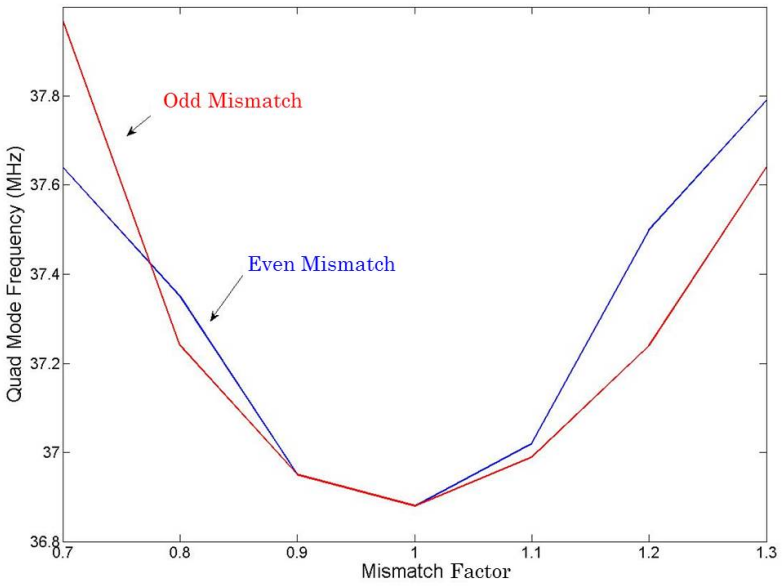

Figure 3.6: Quadrupole envelope mode frequency for the 21 mA beam as a function of initial mismatch. Blue represents an even mismatch and red represents an odd mismatch.

to the envelope velocity variables *env.apenv* and *env.bpenv*, analogous to the right-hand side of equation 3.2. This perturbation is transversely antisymmetric, modeling the excitation of the quadrupole field. Sampling once per lattice period, 20 turns of this applied perturbation are shown in Figure 3.9.

A location in the ring (mid-drift) is selected for the measurement of the growth. The envelope displacements are measured for a phase scan across 2π radians. This is shown in Figure 3.10. The maximum of this phase scan is taken, and the x and y envelope displacements as a function of turn are shown in Figure 3.11. By inspection, it is clear that as the number of turns $n \to \infty$, the peaks approach delta functions.

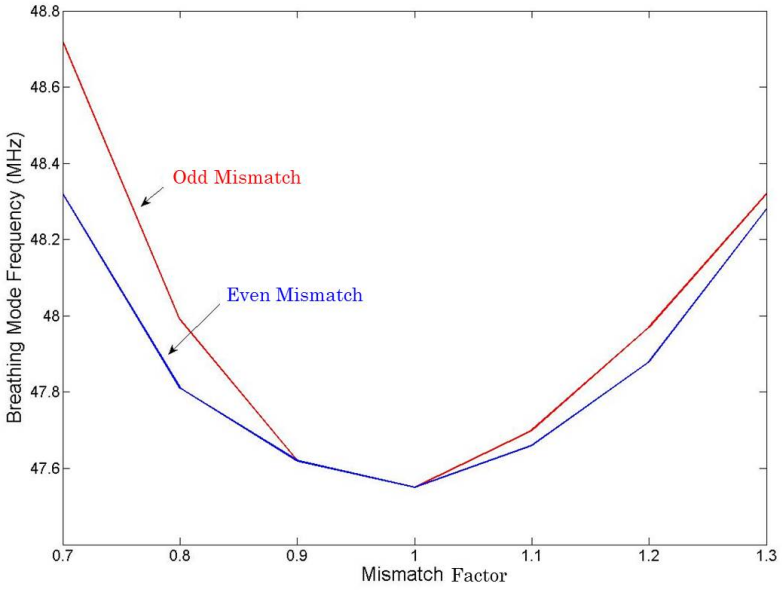

Figure 3.7: Breathing envelope mode frequency for the 21 mA beam as a function of initial mismatch. Blue represents an even mismatch and red represents an odd mismatch.

The mode excitation is amplitude dependent. If the perturbation is too large, the dynamics become nonlinear. It is important to only apply a small quadrupole excitation to the beam to stay within the linear regime. A simulation of the amplitude dependence is shown in Figure 3.12, where the red line represents the chosen amplitude strength.

3.3.4 Emittance Dependence

The initial emittance in the envelope solver is defined to be 30 mm-mrad. A perturbation applied to this value alters the normalized phase advance according to equations 2.13 and 2.14. The mode frequency dependence on phase advance is

Table 3.1: Envelope Mode Frequencies, in MHz

Beam Current	Quadrupole Mode Frequency	Breathing Mode Frequency
0.6 mA	65.5	65.5
6 mA	48.1	53.6
21 mA	36.9	48.0
40 mA	33.7	46.0

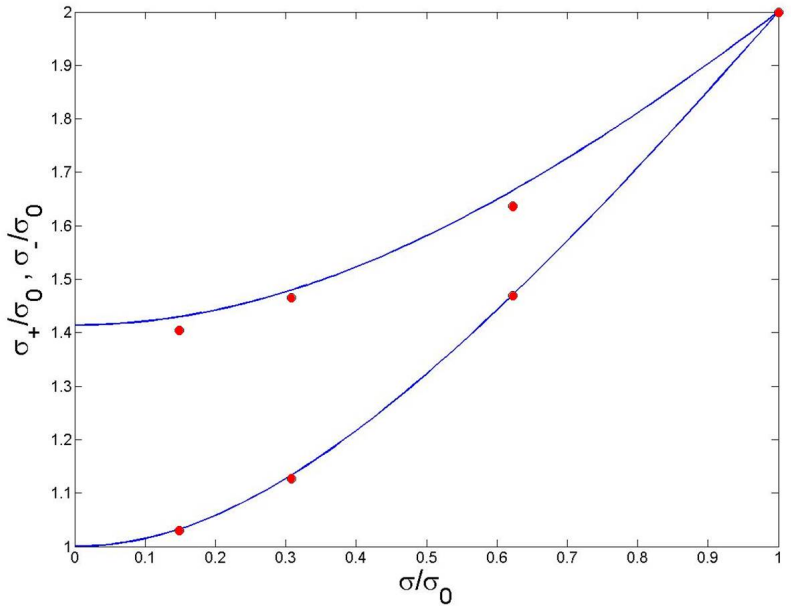

Figure 3.8: Envelope solver mode phase advances (circles) are plotted alongside the predicted values from the smooth approximation.

given in equation 2.24. Finding the mode frequencies using an FFT as described in Section 3.3.2, the frequency dependence on the emittance is determined. A plot of this is shown in Figure 3.13.

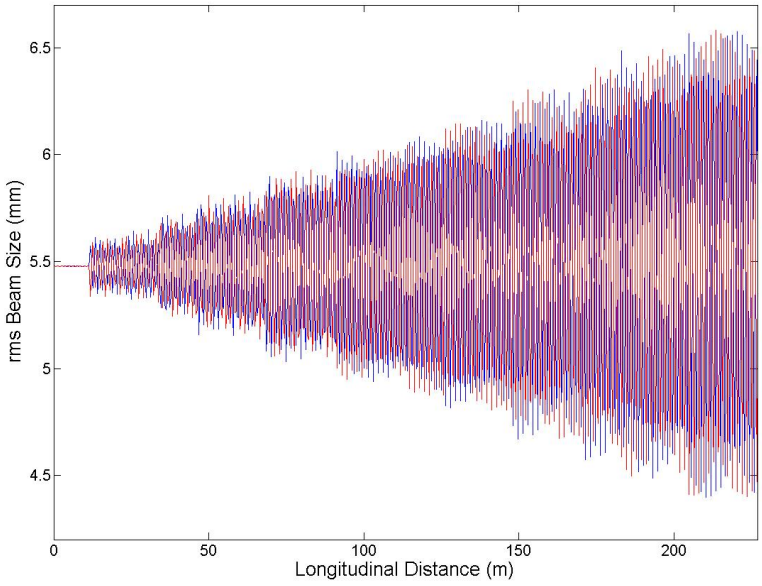

Figure 3.9: Envelope solver simulation of the X (blue) and Y (red) envelope perturbed once per turn, sampled once per lattice period. The rf quadrupole frequency is 37 MHz.

The equation for a fit line for the quadrupole mode is

$$f_{0,Q} = 0.219\epsilon + 30.33. \tag{3.20}$$

This is used to infer the emittance from the measured frequency in the experiment. The slope of the quadrupole mode fit is nearly twice that of the breathing mode slope. This means that exciting the quadrupole envelope mode provides a factor of two more sensitive emittance diagnostic than exciting the breathing envelope mode.

Since the natural mode frequency is emittance-dependent, the resonance structure lattice can be simulated using this envelope solver. This is shown in Figure 3.14. This compares well with the results shown in Figure 3.2.

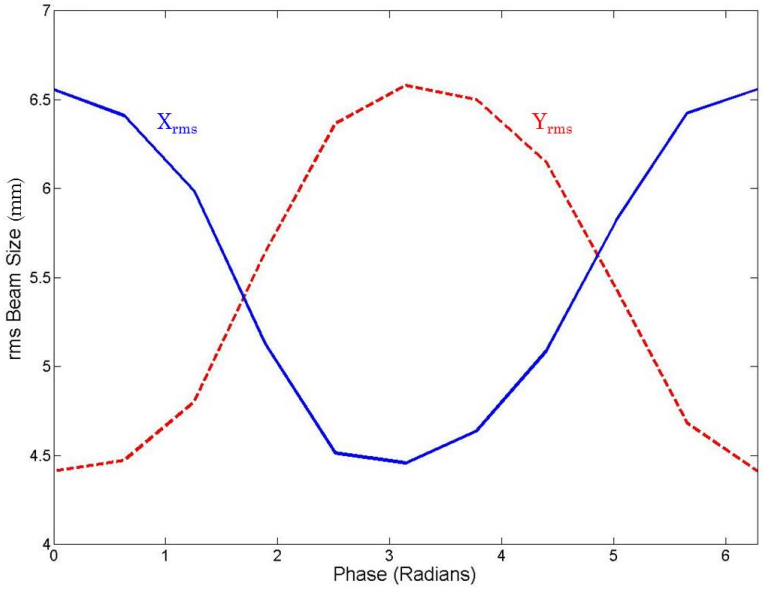

Figure 3.10: rms beam size as a function of initial rf quadrupole phase after 19 passes through the quad for $\omega_0 = \omega$. As is shown, the X_{rms} and Y_{rms} beam sizes are 180° out of phase, indicating a quadrupole excitation.

3.4 PIC Code

Particle-in-cell (PIC) codes require the definition of a grid mesh and the initial particle distribution. Particles are then subject to the integration and interpolation of sources and fields in the mesh. In this way, collective space-charge effects are accounted for. The process is iterated as the beam evolves in time.

3.4.1 Matching Technique

The match values obtained from the envelope solver for each beam setting are imported into the PIC code. Due to the complexities of the beam distribution func-

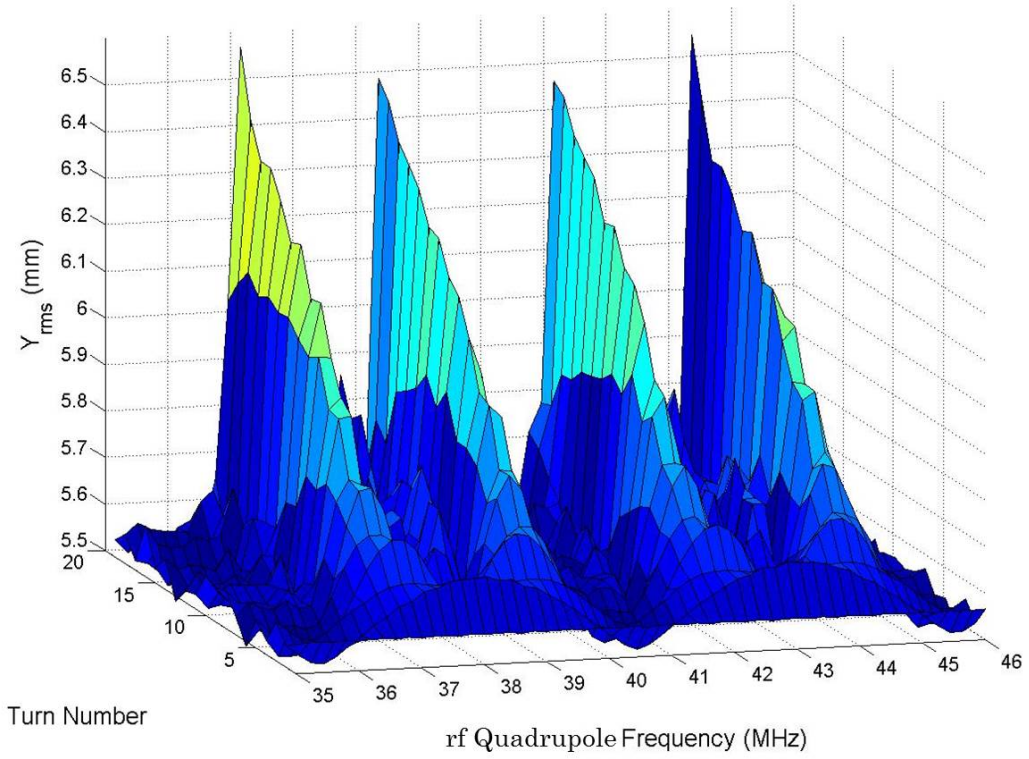

Figure 3.11: Y_{rms} as a function of rf quadrupole frequency and turn number. As $n \to \infty$, the resonant peaks approach delta functions. X_{rms} (not shown) exhibits the same structure.

tion, the envelope match solution is only an approximation of the correct values for the match. Using the WARP functions hpxrms() and hpyrms() from histplotsdoc(), the beam envelope generated from the PIC code was plotted. Plotting these values over one lattice period, the iteration method described in section 3.3.1 was repeated with the PIC code until results converged.

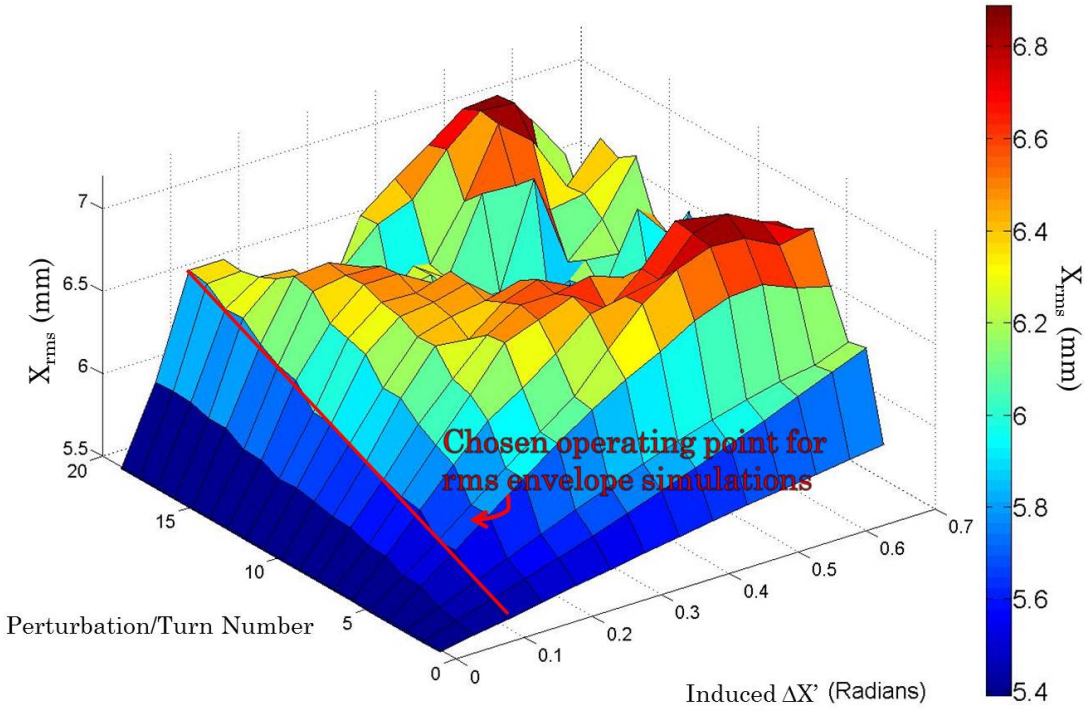

Figure 3.12: X_{rms} as a function of RF quadrupole amplitude and turn number. If the amplitude is too high, the behavior becomes nonlinear. A maximum amplitude is chosen (red line) such that the resonant growth is linear.

3.4.2 Beam Halo Formation

Though more computationally expensive, the usefulness of the PIC code over the envelope code is reflected in the evolution of the transverse phase space distribution over time. For halo studies, 500,000 particles are initially arranged in a semi-Gaussian distribution. After integration, a picture of the transverse beam in both configuration and phase space is recorded.

The experiment simulated in section 3.3.3 is repeated for the PIC code, ap-

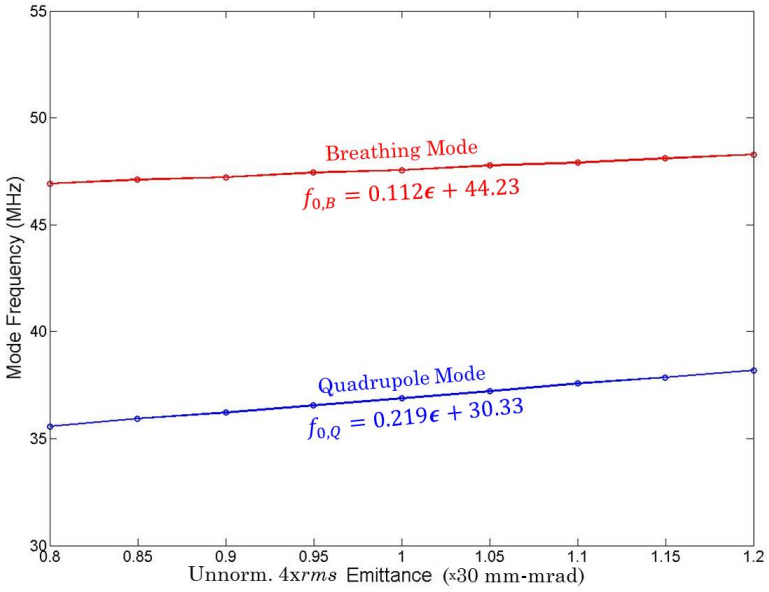

Figure 3.13: Frequency dependence on emittance in the envelope solver simulation.

plying a larger perturbation to particles with a larger displacement from the center of the beam pipe. Once again, dipole fields are neglected, modeling the ring as a LINAC that repeats every 36 FODO periods. Perturbing the beam once per ring "turn" for 20 turns, the beam distribution is shown in Figure 3.15 for a both a resonant and an off-resonant quadrupole frequency. It is shown that on a resonance there is a halo formation, while off resonance there is not. This indicates that the presence of a halo is an indication of resonant mode envelope excitation over long beam lifetimes.

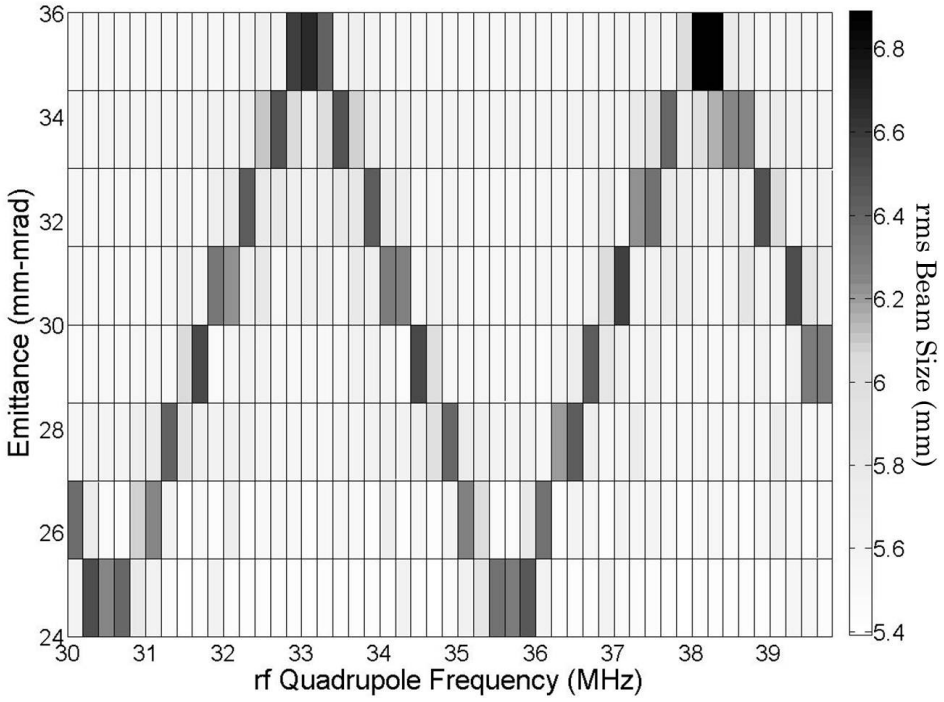

Figure 3.14: Simulated quadrupole mode resonance structure plotted as a function of emittance and rf quadrupole frequency. A change in the emittance directly relates to a change in the natural mode frequency. This result compares to the predicted resonance structure depicted in Figure 3.2.

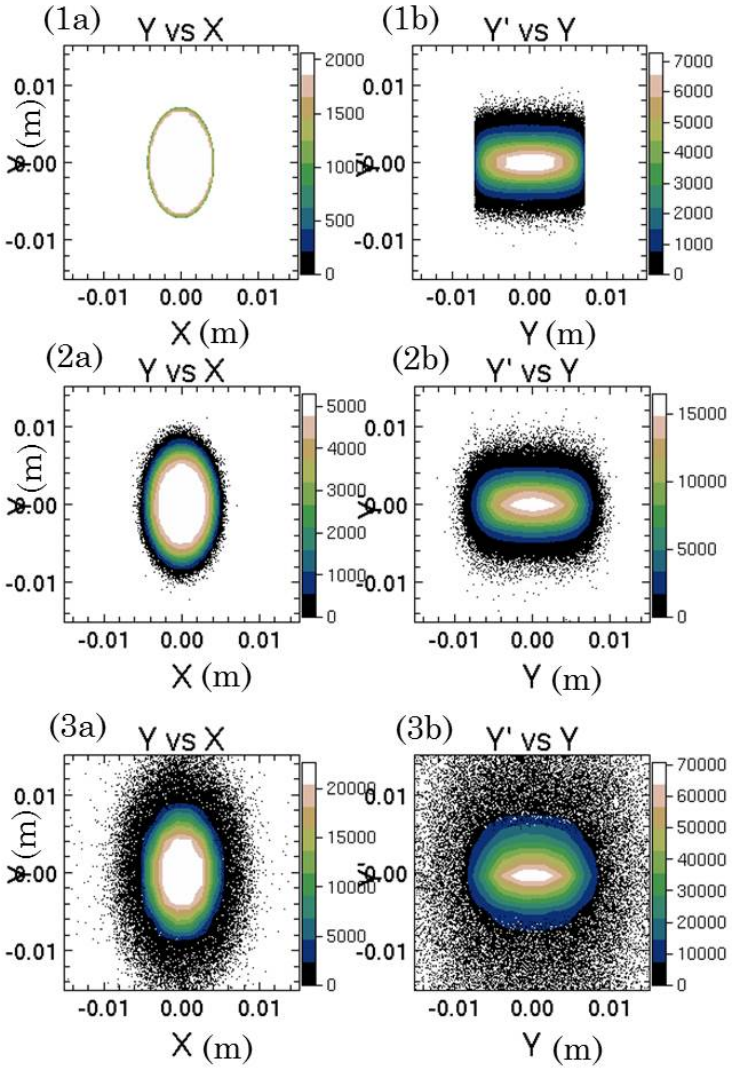

Figure 3.15: WARP PIC results for 500,000 particles perturbed for 20 turns. Configuration space (a) and phase space (b) is plotted for a beam perturbed off resonance (2) and on resonance (3) from its initial conditions (1).

Chapter 4: Experimental Apparatus

An electric quadrupole was built and installed into the University of Maryland Electron Ring (UMER). A tuned tank circuit in an rf box drives the quadrupole. UMER is described followed by a detailed discussion of both the quadrupole and the tank circuit.

4.1 The University of Maryland Electron Ring

The University of Maryland Electron Ring (UMER) is a facility used to study scaled dynamics of intense electron beams over long time scales. A diagram of the ring is shown in Figure 4.1. UMER is a 10 keV electron storage ring with the electron acceleration at the electron gun. The UMER beam parameters are given in Table 4.1.

Table 4.1: UMER Beam Parameters

Beam Energy	10 keV	Energy Spread	10 eV
Circumference	11.52 m	Pipe Diameter	2 in
Circulation Period	197 ns	Initial Pulse Length	∼100 ns
FODO Period	0.32 m	Bunch Repetition Rate	60 Hz

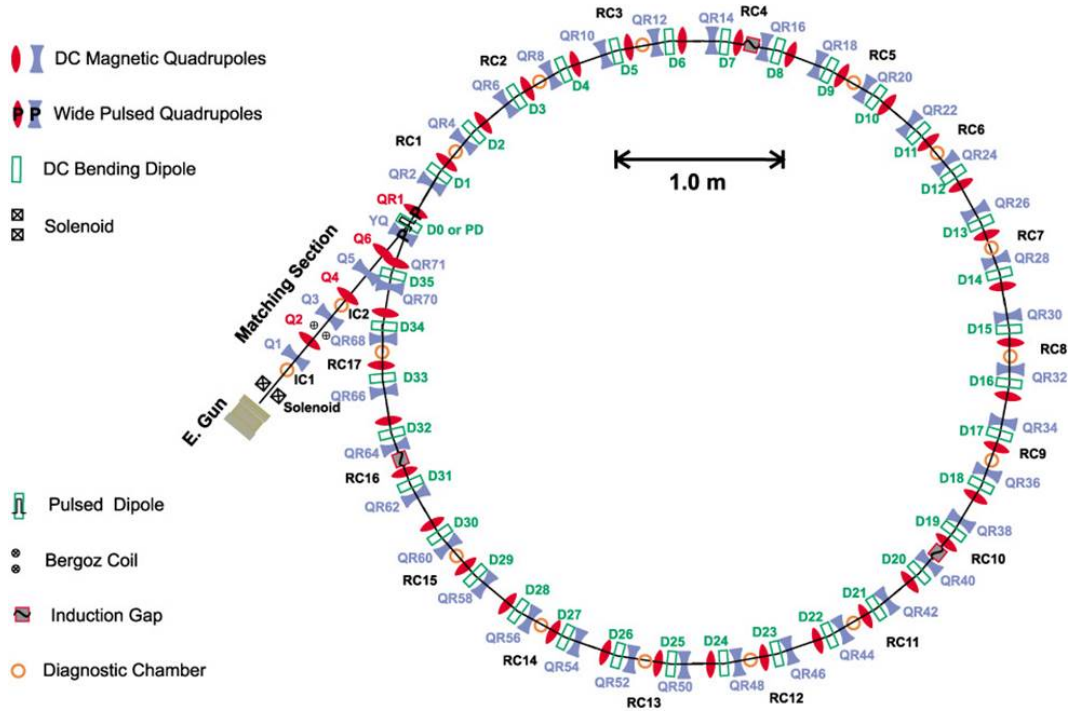

Figure 4.1: Diagram of the University of Maryland Electron Ring (UMER).

The electron beam is injected using thermionic emission from a gridded Pierce-type e-gun. A schematic of the gun circuit is shown in Figure 4.2. A voltage of 10 kV is applied between the cathode and the anode, and a negative bias voltage is applied to the cathode grid to control the beam's current and shape. A pulsed voltage is applied to the cathode, overpowering the bias voltage and allowing electrons to pass. The typical pulse length is 100 ns at injection, but this can be adjusted over a range of 25 to 140 ns. The cathode grid is a mesh of 0.0254 mm diameter wires spaced 0.15 mm apart. As the beam passes through this mesh, part of the beam gets intercepted by the grid, directly affecting the transverse particle distribution. The space-charge-dependent line density in the region between grids creates a "virtual

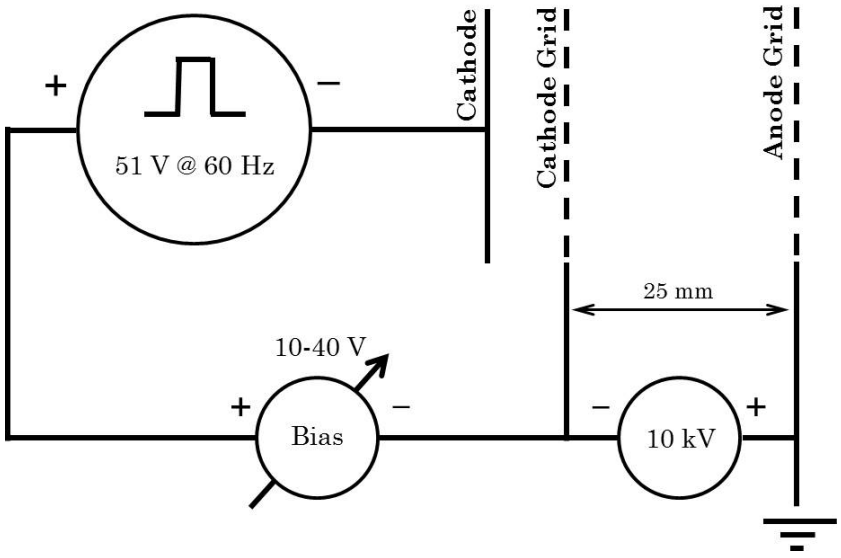

Figure 4.2: Simplified diagram of the UMER gridded gun. The cathode is pulsed at 60 Hz for 100 ns to allow beam injection into the ring. A variable bias voltage is used to test an assortment of emittance values.

cathode" that affects the transverse velocity distribution of the beam [49]. This velocity distribution depends on the bias voltage of the cathode grid that can be adjusted between 10-40 V. Hence, changing the bias voltage will change the emittance. This phenomenon has been carefully studied through analytic calculations and WARP simulations [28, 48].

An aperture wheel downstream from the cathode contains several aperture settings for beam current selection. Current scales with the square of the beam radius, so doubling the aperture size increases the current by a factor of 4. The UMER mask settings are listed in Table 4.2.

The injection section contains several dipole and quadrupole magnets used for matching and steering. Injection steering is described in detail in Appendix

Table 4.2: UMER Aperture Settings

Apert. Radius r_0 (mm)	Current I (mA)	Emitt. ϵ (mm-mrad)	Intensity χ
0.25	0.6	7.6	0.275
0.875	6	25.5	0.605
1.5	21	30.0	0.901
2.85	78	86.6	0.968
Full Beam	104	97.3	0.978

A. Downstream from the injection line, a pulsed dipole steers the beam on to the equilibrium orbit of the ring. The ring itself is structured as a 36-sided polygon, with each side consisting of a single alternating-gradient lattice (FODO) period. Each polygon "corner" contains a 10° dipole bending magnet for steering, see Figure 4.1. At the beam energy of 10 keV, the Earth's magnetic field accounts for 20% of the ring steering. Diagnostic chambers consist mostly of beam position monitors (BPMs) to measure the beam transverse displacement. In ring chamber (RC) 10, an ac-coupled wall current monitor (WCM) tracks the beam current turn-by-turn. The diagnostics used in this dissertation are described in detail in Chapter 5.

For the work detailed in this dissertation, an rf-driven electric quadrupole was built and installed in RC9. The next section details the design and construction of the quadrupole.

4.2 The Electric Quadrupole

4.2.1 The Design of the Quadrupole

A time-varying rf electric quadrupole provides the necessary fields to drive the quadrupole envelope mode in the electron beam. The quadrupole consists of four electrodes with surfaces that approximate hyperbolas placed symmetrically around the center of the beam pipe. To produce the fields that hyperbolic surfaces generate near the center of the pipe, cylindrical surfaces with an electrode-to-gap radius ratio of 1.1468 are used [59, 60]. Since the beam pipe radius is 1 inch, the electrode radius must be machined to 1.1468 inches. The electrodes can be machined within a tolerance of $\pm$ 0.001 inches. The electrode-to-gap radius ratio is 1.147 as shown in Figure 4.3.

The quadrupole replaces the Beam Position Monitor (BPM) located at Ring Chamber 9 (RC9). The chamber has a diameter of 3.74" with a longitudinal opening of 2.8".

The quadrupole fits within the ring chamber and produces the necessary fields to excite the beam resonance. CAD drawings for the designed quadrupole are shown in Figures 4.4 and 4.5. Ceramic washers are used to electrically isolate the four electrodes, and a ceramic shelf provides the necessary structure to rigidly align the quadrupole in the chamber. Two holes in the ceramic shelf fit over 0.125" rods in the ring chamber for additional alignment and stabilization. The electrodes themselves are designed with angled edges to conform to the structure of the chamber. Opposing

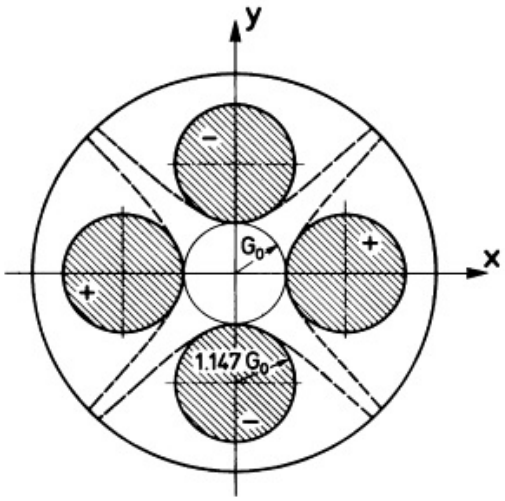

Figure 4.3: To approximate the quadrupole fields produced by hyperbolic surfaces, electrodes with cylindrical surfaces with an electrode-to-gap radius ratio is 1.147 are used [59].

electrodes are connected electrically to each other by using 0.01" thick copper sheet and each set of electrodes is electrically connected to the rest of the circuit by copper wires crimped and soldered to the back of the electrodes and fed up and out of vacuum through a 2.75" 2-pin ceramic feedthrough. The final assembly is shown in Figure 4.6.

The quadrupole is a capacitor in the tank circuit. To estimate the quadrupole capacitance, it is necessary to examine all the components contributing to its value. Figure 4.7 shows the capacitance between the elements of the quadrupole, where the solid green lines represent the capacitance between the electrodes and the dashed red lines represent some of the parasitic capacitances. The capacitive components

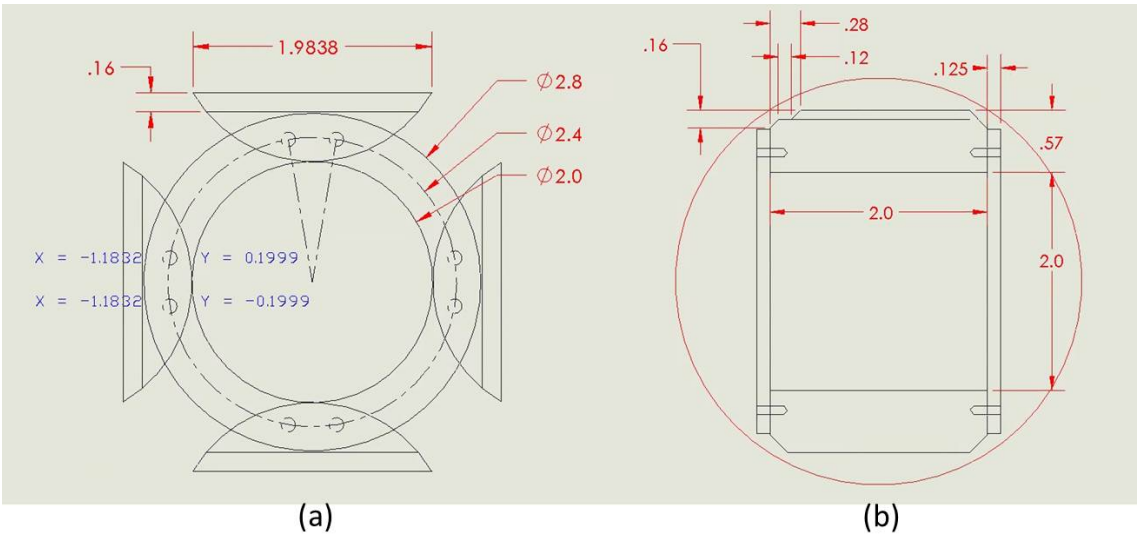

Figure 4.4: CAD drawing showing side (a) and top (b) of the quadrupole inside the BPM chamber. All dimensions are in inches.

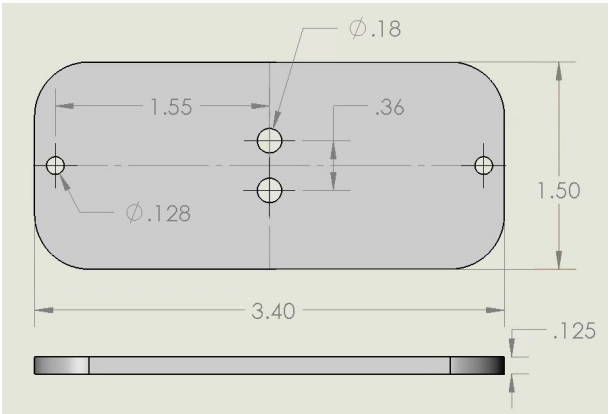

Figure 4.5: Solidworks [51] drawing showing the ceramic shelf dimensions. This shelf is bolted to the top quadrupole electrode and rests on the BPM chamber shelf, with holes for the chamber's 0.125" pins cut wider for easier installation and to account for thermal expansion. All dimensions are in inches.

of the quadrupole are in parallel so the equivalent capacitance is

$$C_{EQ} = C_{12} + C_{13} + C_{24} + C_{34} + C_{para}, \tag{4.1}$$

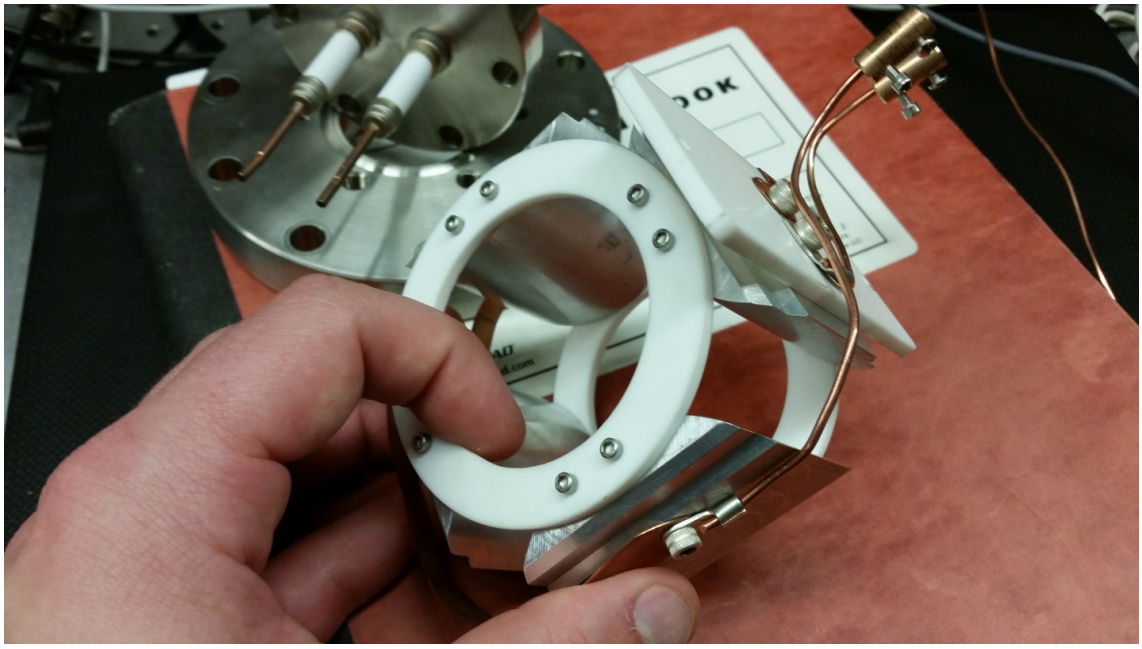

Figure 4.6: The electric quadrupole

where $C_{12} = C_{13} = C_{24} = C_{34} = C_{elec}$ are the capacitances between the electrodes and C_{para} are the lumped parasitic capacitive components. Thus C_{EQ} becomes

$$C_{EQ} = 4C_{elec} + C_{para}. \tag{4.2}$$

4.2.2 Required Electrode Voltage

The electric field must be large enough to deflect the beam and produce a net angular change between $\Delta x' = 10^{-3}$ rad and $\Delta x' = 10^{-1}$ rad after traversing the quadrupole. During a single pass, a particle in the beam is acted upon by the quadrupole field for ~ 0.857 ns, and the quadrupole can be treated as a thin lens. The trace space change in x and x' for a charged particle traversing the quadrupole

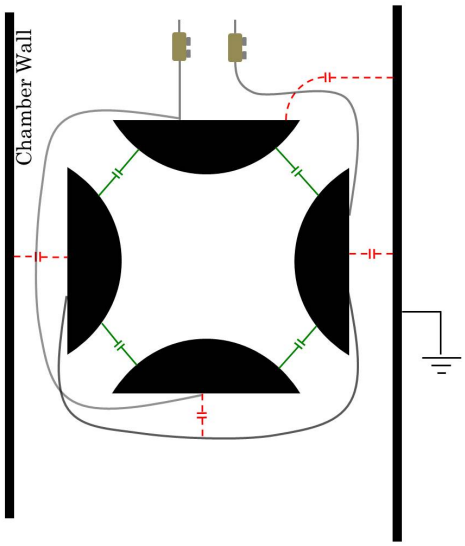

Figure 4.7: Circuit diagram of most of the capacitive components of the quadrupole. The solid gray lines represent the electrical connections made by copper sheet and wire, while the green and red lines represent the capacitances. The dashed lines represent the parasitic capacitance due mostly to the close proximity of the chamber wall.

is

$$\begin{pmatrix} x_2 \\ x_2' \end{pmatrix} = \begin{pmatrix} 1 & 0 \\ \frac{1}{f} & 1 \end{pmatrix} \begin{pmatrix} x_1 \\ x_1' \end{pmatrix}. \tag{4.3}$$

Since the transverse displacement of the particle does not change, only the slope is considered. The change in slope is derived as

$$\begin{aligned} x_2' &= \frac{x_1}{f} + x_1', \\ x_2' - x_1' \equiv \Delta x' &= \frac{x_1}{f}, \\ \Longrightarrow \quad \frac{\Delta x'}{x_1} &= \frac{1}{f}, \end{aligned} \tag{4.4}$$

where $\frac{1}{f} = \kappa l$. l is the length of the quadrupole[1] and Reiser [37] shows that the focusing strength κ is

$$\kappa = \frac{qE_0}{\gamma mav^2} = \frac{V_0}{V_b a^2}. \tag{4.5}$$

Here, V_b is the beam voltage (10 kV), a is the beam pipe radius (2.54 cm), and V_0 is the voltage on the electrodes. Making the appropriate substitutions and solving for V_0,

$$V_0 = \frac{\Delta x'}{x_1 l} V_b a^2. \tag{4.6}$$

For a maximum beam radius of 5 mm, an applied voltage between $V_0 = 25.4$ V and $V_0 = 2.54$ kV is needed on each electrode. In order to achieve this voltage, the quadrupole will be connected to a resonant circuit, driven with a function generator in series with a small amplifier.

4.2.3 Quadrupole Simulations

ANSYS® Maxwell 3D [52] provides an electrostatic simulation of quadrupole fields. With this program, the contribution of both the fringe fields from the quadrupole and the parasitic capacitance from the beam chamber walls can also be simulated. A picture of the simulated quadrupole inside the BPM chamber is shown in Figures 4.8 and 4.9.

The results of the simulations are shown in Figures 4.10 and 4.11. Figure 4.10 shows the transverse electric field as a function of longitudinal displacement at different transverse displacements on the y=0 axis. The nearly flat top field shown

[1] 2" or 5.08 cm

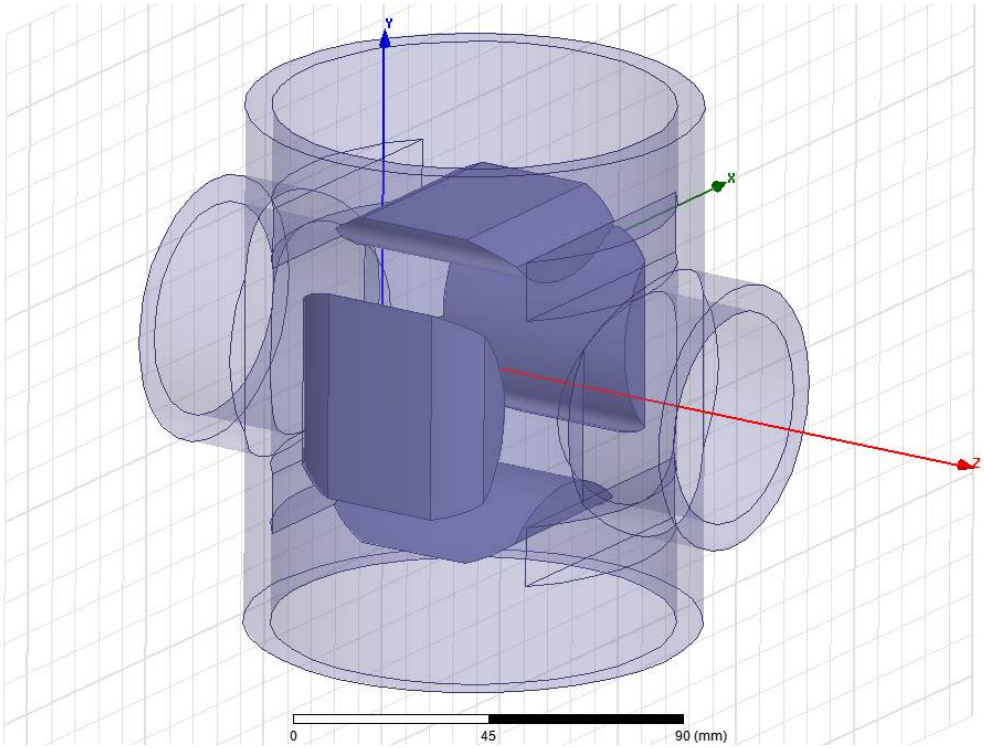

Figure 4.8: Maxwell 3D simulation of the electric quadrupole in the chamber pipe. The quadrupole electrodes are depicted as solid surfaces while the chamber is mostly transparent.

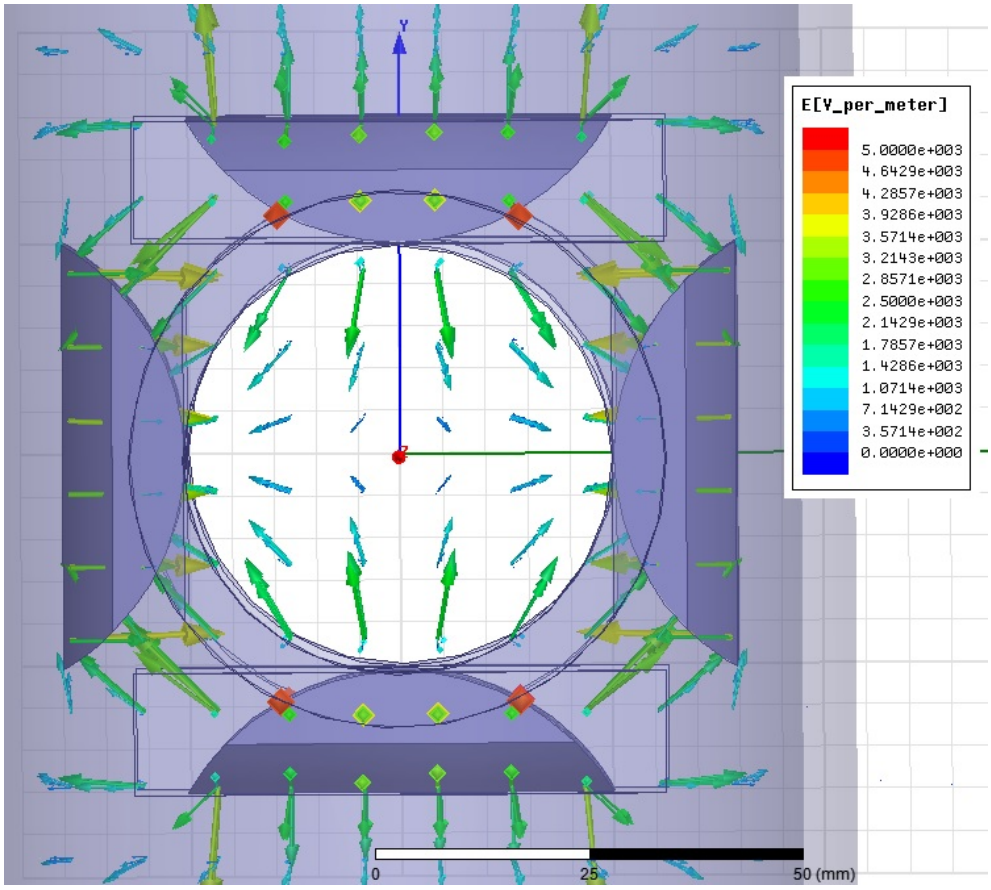

Figure 4.9: Maxwell 3D simulation of the electric fields from the quadrupole. This view is looking down the beam pipe through the quadrupole.

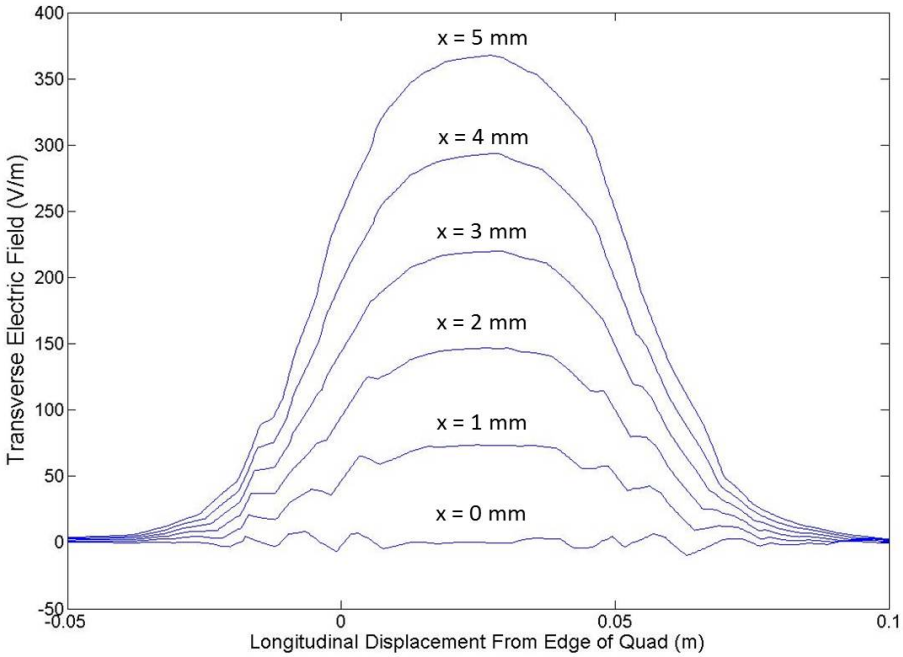

Figure 4.10: Maxwell 3D simulation results. Transverse electric field is plotted as a function of longitudinal displacement. Transverse displacement is confined to one dimension, labeled as x.

in this figure reflects the uniform field experienced by the beam as it traverses the quadrupole. Figure 4.11 shows the longitudinal electric field along the same integration paths. This figure shows the electric fringe fields in the quadrupole, applying a longitudinal perturbation to the beam. An analysis of this perturbation is explored in the following section.

The voltage as a function of transverse displacement from the center axis of the quadrupole was also simulated. The longitudinal position is fixed at the center of the quad. The results are shown in Figure 4.12.

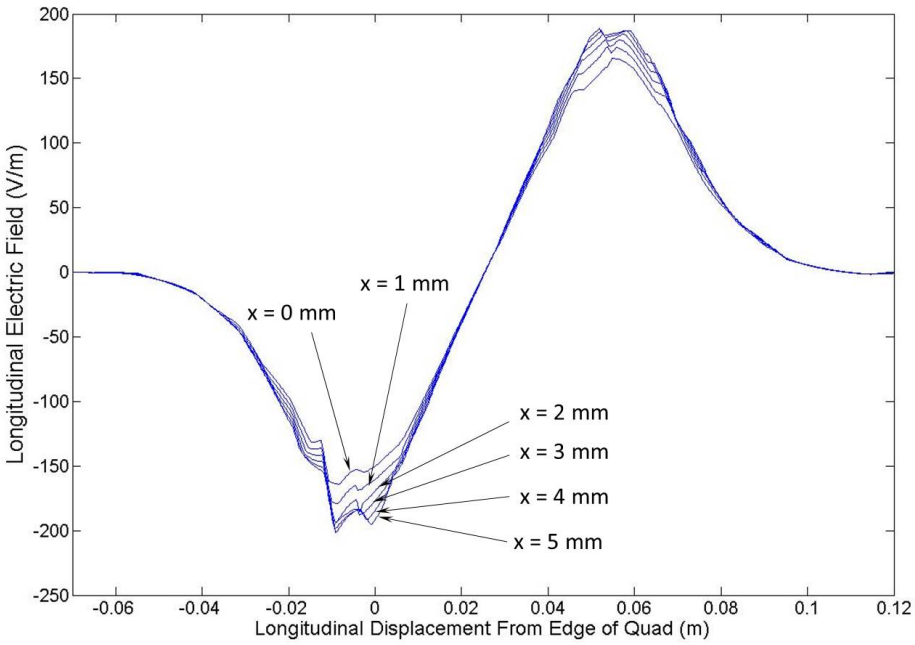

Figure 4.11: Maxwell 3D simulation results. Longitudinal electric field plotted as a function of longitudinal displacement. The separate lines represent different transverse displacements from 0 to 5 mm, confined to one dimension.

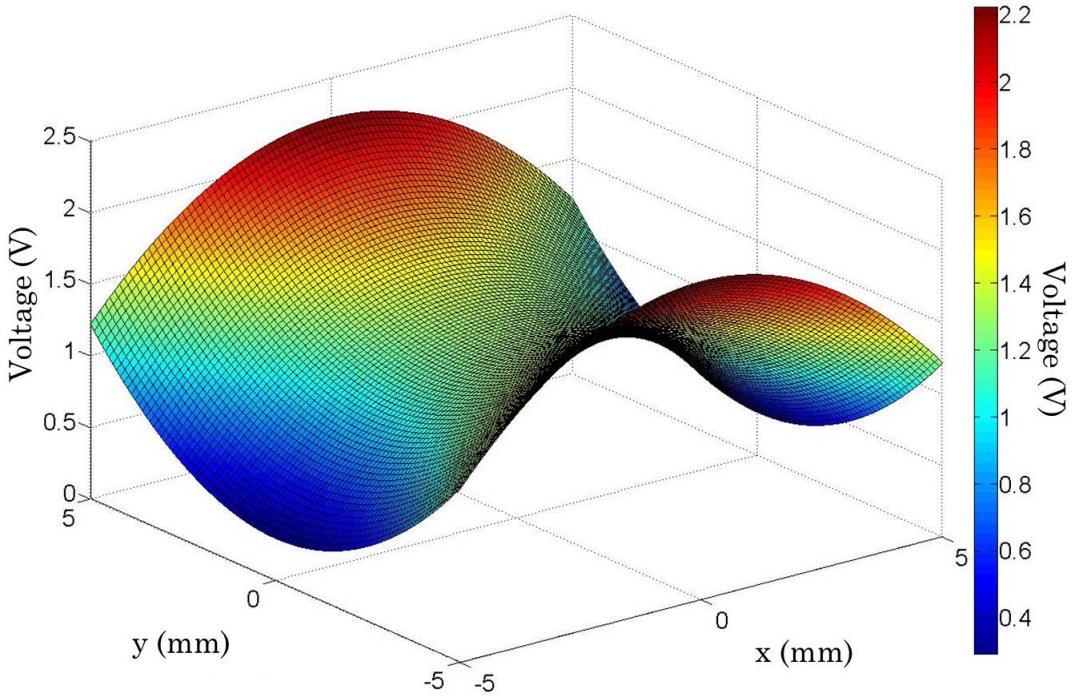

Figure 4.12: Maxwell 3D simulation of the voltage inside the quadrupole as a function of transverse displacement from the center.

4.2.4 Magnetic Fringe Fields

Electromagnetic fields affect the charged particles in the beam according to the Lorentz force

$$\vec{\mathbf{F}} = e(\vec{\mathbf{E}} + \vec{\mathbf{v}} \times \vec{\mathbf{B}}), \tag{4.7}$$

where e is the elementary charge due to an electron and $\vec{\mathbf{v}}$ is the beam's velocity, with magnitude βc.

To completely understand how the fields generated by the quadrupole affect

the beam dynamics, it is necessary to calculate the magnetic fields generated by the time-varying electric fringe fields. For the 21 mA beam, the quadrupole fields will oscillate at a frequency near 37 MHz, giving an oscillation period of 27 ns. Since a particle takes 0.857 ns to traverse the quadrupole, it only experiences 0.031 field oscillations in a given pass. Even at the zero space charge limit for envelope mode frequencies (56.5 MHz), a particle only experiences 5.6% of a field oscillation on a single pass. Thus, for a simplified analysis, it is assumed that the particle experiences a static quadrupole field. However, for generality, the time-dependance of the fields is considered.

Maxwell's equations in vacuum are

$$\nabla \cdot \vec{\mathbf{E}} = 4\pi\rho, \tag{4.8a}$$

$$\nabla \cdot \vec{\mathbf{B}} = 0, \tag{4.8b}$$

$$\nabla \times \vec{\mathbf{E}} = -\frac{\partial \vec{\mathbf{B}}}{\partial t}, \tag{4.8c}$$

$$\nabla \times \vec{\mathbf{B}} = \mu_0 \left(\epsilon_0 \frac{\partial \vec{\mathbf{E}}}{\partial t} + \vec{\mathbf{J}} \right). \tag{4.8d}$$

The static electric fields shown in Figures 4.10 and 4.11 provide the basis for the magnetic field calculation. These are the spatially-varying amplitudes of an electric field that varies sinusoidally in time. The time-dependence is

$$\vec{\mathbf{E}}(x, y, s, t) = \tilde{\vec{\mathbf{E}}}(x, y, s) e^{i\omega t}. \tag{4.9}$$

The magnetic field takes the same form. Thus,

$$\vec{\mathbf{B}}(x, y, s, t) = \tilde{\vec{\mathbf{B}}}(x, y, s) e^{i\omega t}. \tag{4.10}$$

The most direct way to calculate the magnetic fields in this case is to use Faraday's Law (Equation 4.8c). Since the time-dependence of $\vec{\mathbf{B}}$ is known, the right-hand side is directly linearized to

$$-\frac{\partial \vec{\mathbf{B}}}{\partial t} = -i\omega \vec{\mathbf{B}}. \tag{4.11}$$

The curl of $\vec{\mathbf{E}}$ is evaluated with the Levi-Civita tensor as

$$\nabla \times \vec{\mathbf{E}} = \varepsilon_{ijk} \nabla_j E_k \mathbf{e}_i = (\partial_y E_s - \partial_s E_y)\hat{x} - (\partial_x E_s - \partial_s E_x)\hat{y} + (\partial_x E_y - \partial_y E_s)\hat{s}, \tag{4.12}$$

where $\mathbf{e}_i = (\hat{x}, \hat{y}, \hat{s})$ is the orthonormal basis spanning the coordinate system described in section 2.1.1. The term $\partial_y E_s$ determined from the data in Figure 4.11 is approximately 6.5% of the value of $\partial_s E_y$ at its maximum value. Similarly, the term $\partial_x E_s$ is approximately 9.2% of the value of $\partial_y E_s$. Thus, to first order, $\partial_y E_s \approx 0$ and $\partial_x E_s \approx 0$. Furthermore, using the paraxial approximation introduced in chapter 2, it can be assumed that the beam's velocity is directed in the s-direction. By inspection of equation 4.7, the s-component of the magnetic field will not apply a force to the beam. Thus, the $\hat{s}$ terms of equation 4.12 can be neglected. Finally, the left-hand side of equation 4.8c is

$$\nabla \times \vec{\mathbf{E}} = \partial_s E_x \hat{y} - \partial_s E_y \hat{x}. \tag{4.13}$$

Solving for $\vec{\mathbf{B}}$,

$$\vec{\mathbf{B}} = \frac{i}{\omega}(\partial_s E_x \hat{y} - \partial_s E_y \hat{x}), \tag{4.14}$$

where i represents the $\frac{\pi}{2}$ temporal phase shift between the magnetic and electric fields. This magnetic field will be used in the next section to show the affect of the beam's trajectory on these fringe fields.

4.2.5 Particle Tracing

Using the fields from the Maxwell 3D simulations for both the x and y displacements, the electric fields are numerically differentiated using the finite difference method

$$\partial_s E_{x,y} = \lim_{ds \to 0} \frac{E_{x,y}(s + ds) - E_{x,y}(s)}{ds}. \tag{4.15}$$

After solving for the magnetic field within the quadrupole using equations 4.14 and 4.15, equation 4.7 is used to find the force acting on a particle at any point in space. The leapfrog integration method is then used to trace the particle's path as it passes through the magnetic fields generated by the quadrupole. The results are shown in Figure 4.13.

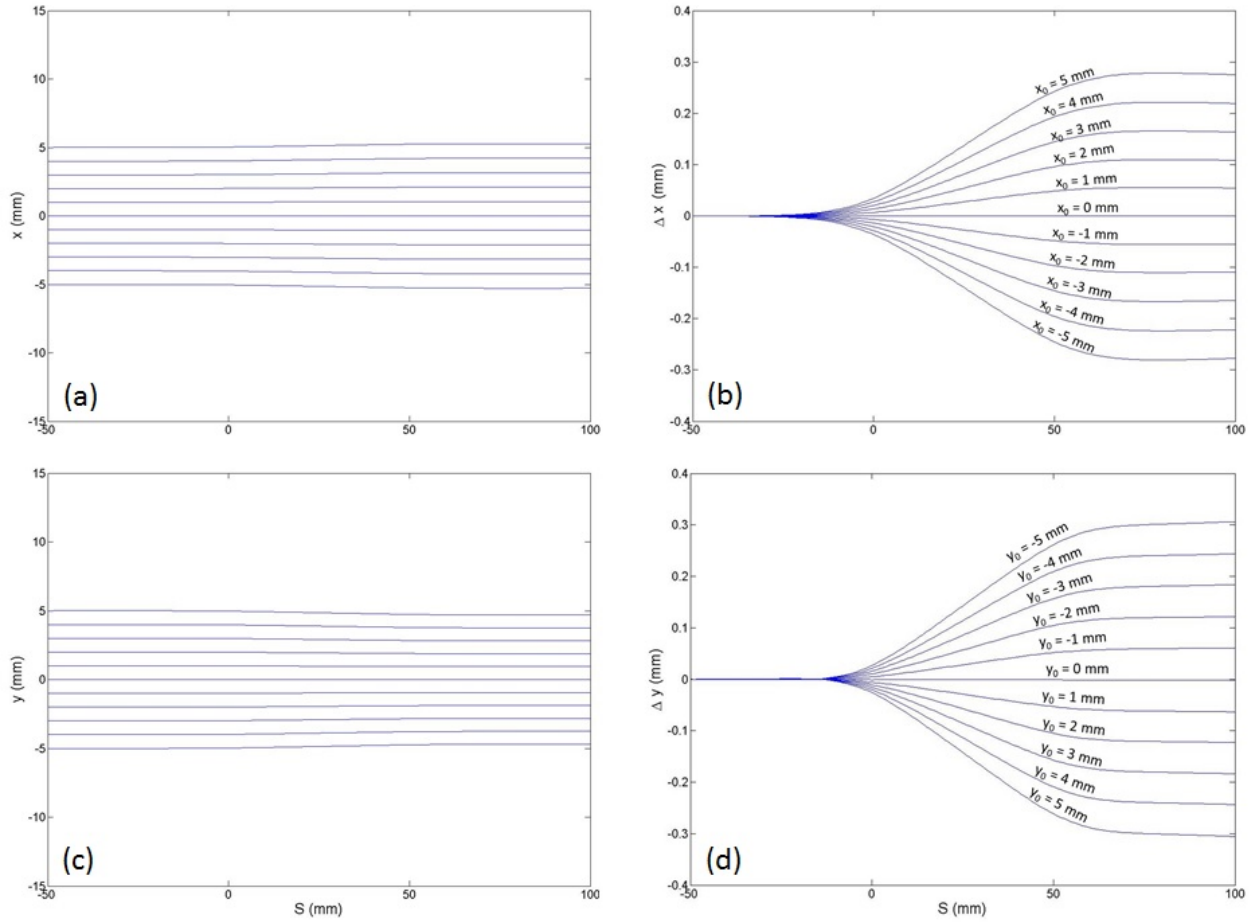

Figure 4.13: Leapfrog particle tracing of an electron passing through the magnetic fringe fields generated by the quadrupole for initial displacements in (a) x (for y=0) and (c) y (for x=0). The change in the particles trajectories is shown in plots (b) and (d). The force due to electric fields, space charge, and the Earth's magnetic field are not included.

For this particular case, the force due to electric fields, space charge, and the Earth's magnetic field are neglected in order to investigate how the magnetic fields generated by the quadrupole influence the particle's motion. By inspection of equations 4.14 and 4.7, a particle initially displaced in x or y will experience a force in the same direction as its displacement. Therefore the horizontal and vertical fringe field effects are uncoupled.

Two interesting observations are made about the particle trajectories. First, the magnetic fringe fields cause the beam spot size to increase in x but decrease in y, creating an ellipse in configuration space. However, this effect is small compared to the beam radius. For the amplitude of the fields, a particle initially displaced 5 mm will experience approximately a 0.3 mm transverse displacement. A 5 mm radius beam entering with a circular transverse cross section will exit with an elliptical cross section with an eccentricity of 0.45. For particles entering parallel to the axis, they will exit with a $\Delta x' \approx 0$. This result ensures no halo growth due to the magnetic fields in the quadrupole.

4.3 Bench Measurements of the Quadrupole

To get an accurate measurement of quadrupole capacitance and voltage applied to the electrodes, the quadrupole was placed inside a BPM bench chamber that has identical dimensions to the vacuum chamber at RC9. A picture of the quadrupole in this bench chamber is shown in Figure 4.14.

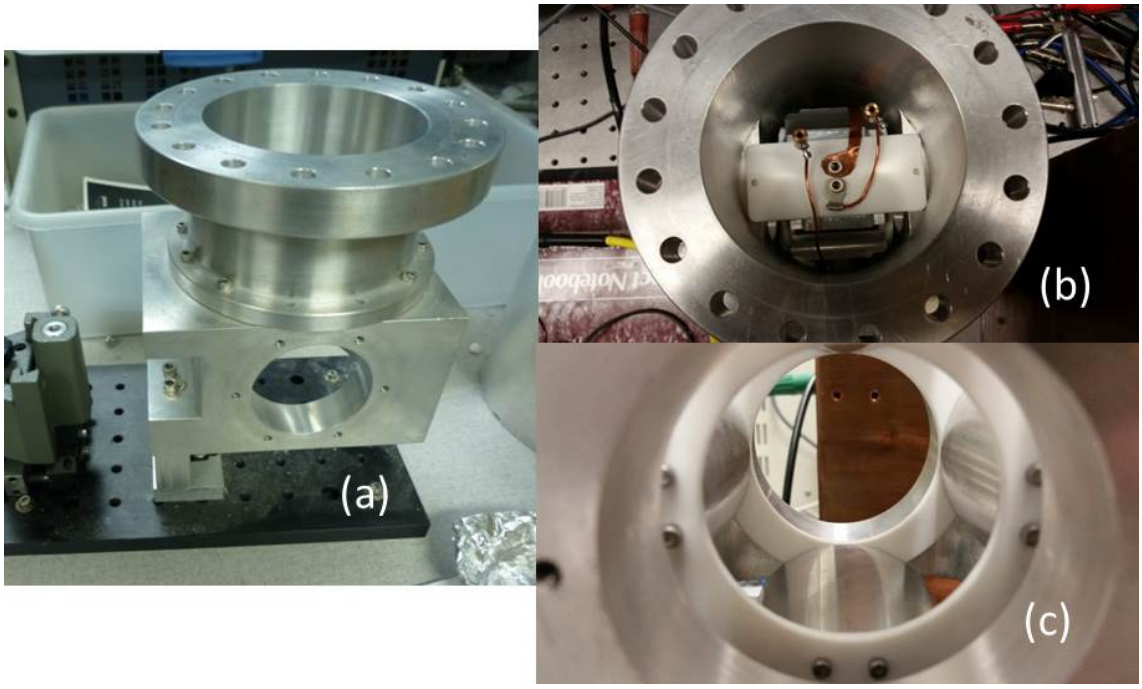

Figure 4.14: (a) BPM bench chamber, (b) a top-down view of the quadrupole, and (c) a side "beam view" of the quadrupole inside the chamber.

4.3.1 Capacitance Measurement

An Agilent E5061B impedance analyzer [63] was used to evaluate the capacitance of the quadrupole as a function of frequency after installation. Measurements were taken over the range of frequencies used in the experiment, and the capacitance increases monotonically with frequency. At 36.9 MHz[2] the quadrupole capacitance is about 23.7 pF.

[2]the predicted resonant frequency for the 21 mA quadrupole mode

4.3.2 Quadrupole Potentials and Circuit Tuning

An oscilloscope was used to measure the voltages applied to the quadrupole elements. The oscilloscope is triggered by the sinusoidal signal produced by the function generator; oscilloscope probes were attached to the screws of the electrodes for a measurement of the applied voltage to the electrode from the function generator through the tank circuit.

There is an 8.6% difference in electrode amplitudes due to the greater parasitic capacitance on the left and right electrodes compared to the top and bottom electrodes. To investigate this further, a copper wire probe was used to measure the peak-to-peak (p-p) voltage inside the quadrupole. The result is shown in Figure 4.15. There are still quadrupole fields, but the saddle point of the Voltage mesh plot is 4.27 ± 0.05 mV for an applied primary circuit p-p voltage of 5 V, providing an unwanted voltage difference between the center of the quadrupole and the beam pipe outside of the quadrupole. This voltage bias is also shown in the Maxwell 3D simulations (Figure 4.12). Since electric fields (and force) are proportional to the gradient of the electric potential, a particle experiences an undesired longitudinal force as it enters and exits the quadrupole. This force is small compared to the desired result, but a series of measurements confirm that it grows linearly with the input voltage to the quadrupole. When enough voltage is applied to the quadrupole to drive the resonance as simulated in Figure 4.12, we get a potential of greater than 1 V at a zero transverse displacement, providing a substantial gradient "potential hill" as the beam traverses the quadrupole.

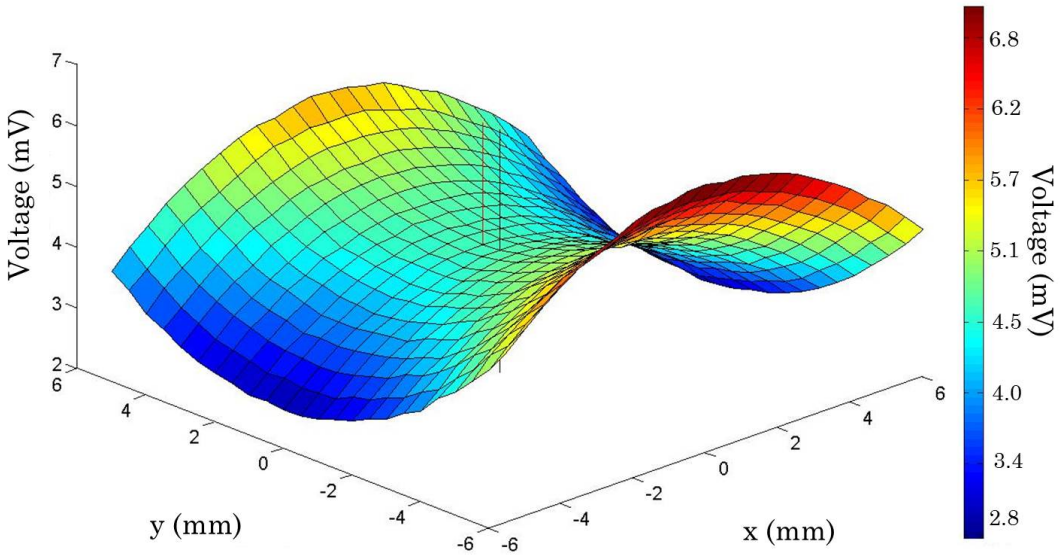

Figure 4.15: Measured voltage inside the quadrupole as a function of transverse displacement from the center. The black line and red line represent the geometric and electrical centers, respectively. The displacement between these centers is 0.7 ± 0.2 mm.

To correct for the electrode voltage imbalance, an additional trim capacitor is added to the side of the circuit with the greater peak-to-peak voltage value on the electrodes. This capacitor is fixed to the floor of the rf box and stabilized with a ceramic standoff.

A Poisson Superfish [61] simulation was run with mismatched electrode voltages to further explore the impact of the mismatch. The results of the simulation show that the mismatch causes the zero potential lines to shift outward from the center, forming hyperbolas. This is shown in Figure 4.16.

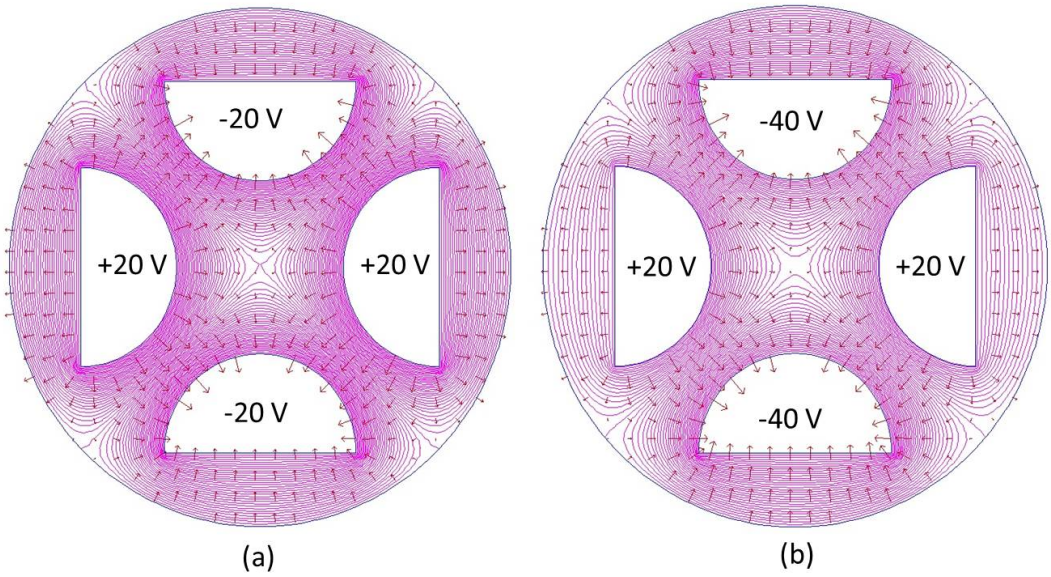

Figure 4.16: Poisson Superfish simulation of (a) a standard electric quadrupole and (b) a significant voltage mismatch between the electrodes.

The bench tests showed the difficulty in having the center of the quadrupole at zero volts. A series of simulations were run with Poisson Superfish to explore this phenomenon. It is found that balancing the voltages on the electrodes is a very sensitive adjustment. This is illustrated in Figure 4.17. After setting the center quad voltage as close to zero as possible, new probe data were taken. These data are shown in Figures 4.18 and 4.19.

In addition to the voltage imbalances between the electrode pairs, there is a small (9.75% and 14.26%) mismatch between the horizontal and vertical electrodes due to the different electrical connections. The copper sheet that connects the electrodes in the bench chamber produces capacitive component to the electrodes close to the sheet. Poisson Superfish simulations were run to see the effect this would

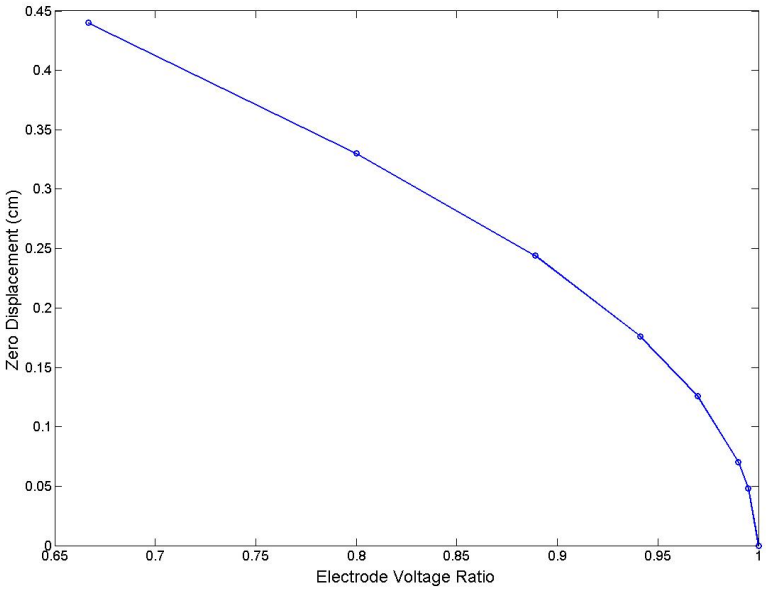

Figure 4.17: The zero voltage displacement from the center of the quadrupole is plotted as a function of electrode voltage ratio. A small difference from a matched electrode voltage produces a substantial displacement of the zero voltage.

have on the quadrupole voltages and fields, and no measurable effect was found.

In the next section, the rf box setup used to drive the rf electric quadrupole will be described in detail.

4.4 The Radio-Frequency (rf) Box

The electric quadrupole is driven by a tank circuit enclosed in an rf box. It is imperative to maintain a constant peak voltage across the quadrupole electrodes at all driving frequencies.

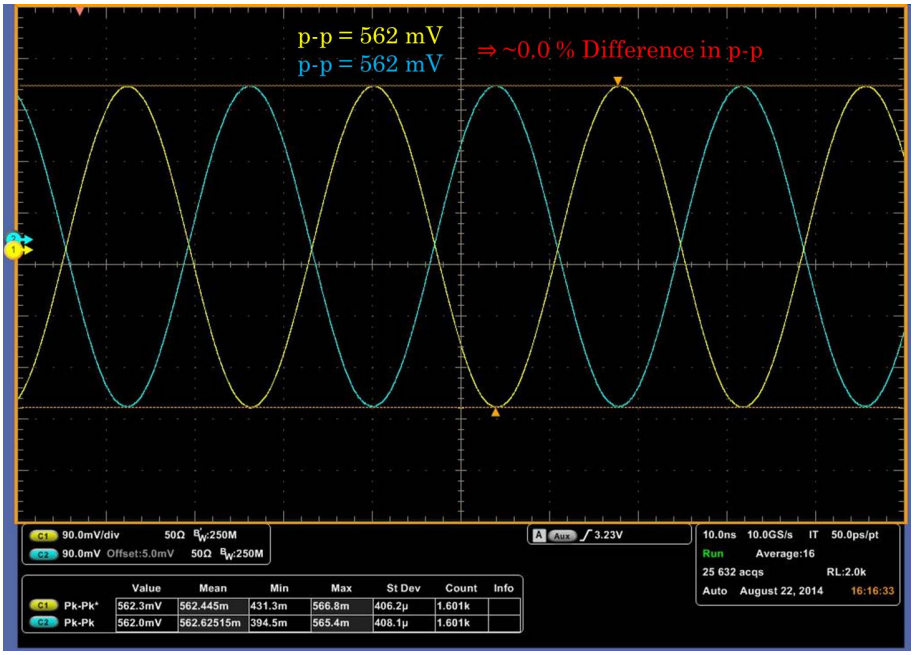

Figure 4.18: Voltage on the Top and Left electrodes from Ch. 1 and 2, respectively, after adjusting for the parasitic capacitance.

4.4.1 Introduction to Resonant Tank Circuits

A tank circuit is a driven resistor, inductor, capacitor (RLC) circuit that resonates at a characteristic frequency. The inductance of the circuit has a reactance proportional to the driving frequency, while the capacitance of the circuit has a reactance inversely proportional to the driving frequency. The complex impedance of a series RLC circuit [55] is

$$z = R + i\left(\omega L - \frac{1}{\omega C}\right), \tag{4.16}$$

with magnitude

$$Z = \sqrt{R^2 + \left(\omega L - \frac{1}{\omega C}\right)^2}. \tag{4.17}$$

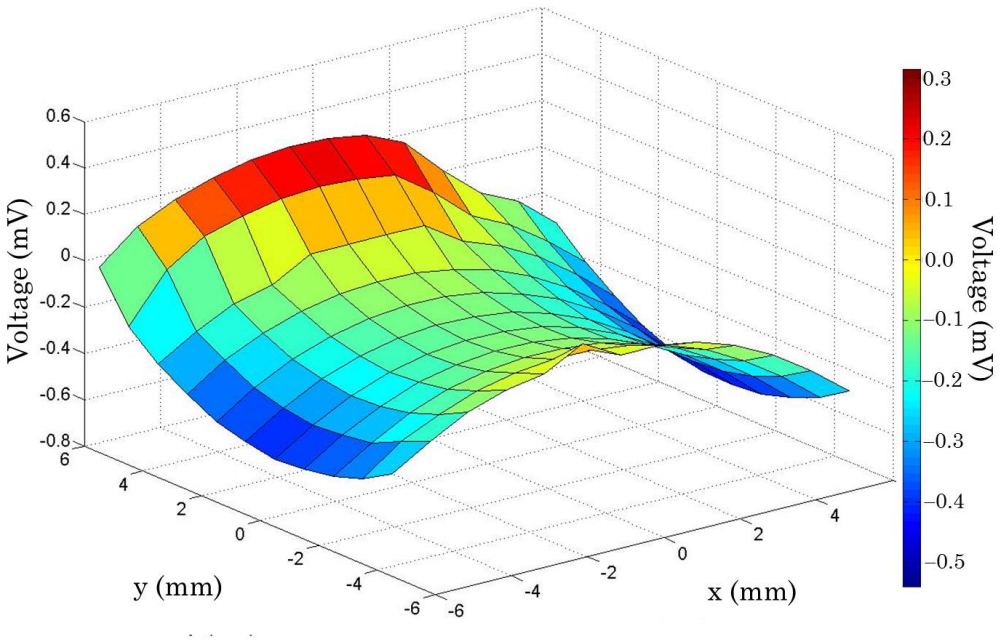

Figure 4.19: Measured voltage inside quadrupole after compensating for parasitic capacitance. The center voltage is now -0.2 ± 0.05mV for a voltage input of 400mV. The bumpiness in the plot reflects the noise in the pk-pk oscilloscope measurement near V=0.

Here, R is the effective "ac" resistance of the circuit, ω is 2π times the driving frequency, and $\omega L = X_L$ and $\frac{1}{\omega C} = X_C$ are the inductive and capacitive reactances, respectfully. The impedance is minimized when the reactances are equal and $\omega_0 L = \frac{1}{\omega_0 C}$, where $\omega_0 = 2\pi f_0$ is the value of the resonant frequency. The resonant frequency is

$$f_0 = \frac{1}{2\pi\sqrt{LC}}. \tag{4.18}$$

Since losses in the series tank circuit primarily occur in the inductive coil, the quality factor Q of the circuit primarily depends on the inductance of the coil [55]

and is given by

$$Q = \frac{\omega L}{R} = \frac{f_0}{\Delta f}. \tag{4.19}$$

This is a measure of the quality of the resonant peak. It is the inverse of the fractional bandwidth and is defined as the ratio of energy stored in the circuit to energy dissipated per cycle at resonance [57]. The Q value is also important in determining the attenuation rate α and exponential time constant τ of the circuit. They are related by

$$\alpha = \frac{1}{\tau} = \frac{\omega_0}{2Q}. \tag{4.20}$$

In an RLC circuit, there is a time-varying voltage drop across each component. However, the voltages are out of phase with each other. The phasor diagram provided in Figure 4.20 illustrates this. The length of the phasor corresponds to the voltage amplitude, while its projection on the y-axis as it rotates at the driving frequency ω corresponds to the voltage value at time t.

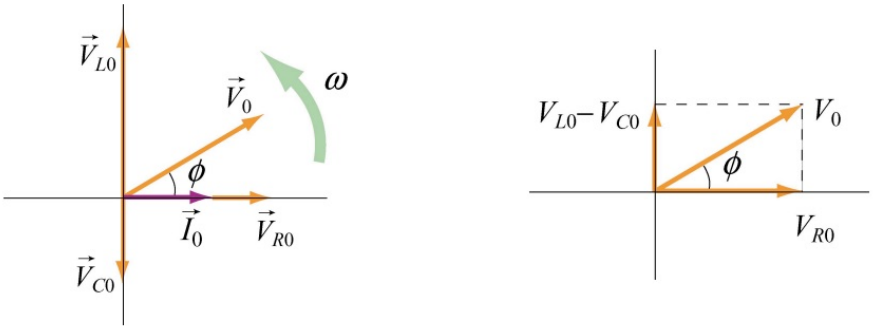

Figure 4.20: Phasor diagram for the series RLC circuit [56].

The resistive phasor is in phase with the current phasor. However, the current

phasor is out of phase with both the inductive and the capacitive phasors by $\pi/2$, lagging and leading, respectively. Since the phasors are out of phase, their amplitudes cannot be added as scalars. The phasors are added as vectors. The angle that the summed voltage phasor makes with the current phasor is denoted ϕ, and this value goes to 0 at resonance as the capacitive and inductive voltage amplitudes match [56].

$$\begin{aligned} V_0 = |\vec{V_0}| = |\vec{V_R}0 + \vec{V_L}0 + \vec{V_C}0| = \sqrt{V_R 0^2 + (V_L 0 - V_C 0)^2} \\ = \sqrt{(I_0 X_R)^2 + (I_0 X_L - I_0 X_C)^2} = I_0 \sqrt{(X_R)^2 + (X_L - X_C)^2} \end{aligned} \tag{4.21}$$

The amplitude of the time-varying current is

$$I_0 = \frac{V_0}{\sqrt{R^2 + (\omega L - \frac{1}{\omega C})^2}} = \frac{V_0}{Z}. \tag{4.22}$$

At the resonant frequency, the current is $I_0 = \frac{V_0}{R}$.

To simplify the tank circuit used in the experiment, the circuit components are first considered as a lumped inductance, capacitance, and resistance in series. The values of these components will be revisited in a later section. To minimize the resistance in the circuit, the secondary (or main) circuit is inductively coupled to a primary driving circuit that provides the power necessary to excite the resonance. The driving term in the secondary circuit is the mutual inductance from the primary circuit. The circuit diagram is shown in Figure 4.21.

The time-dependent equation is

$$V(t) - V_R(t) - V_L(t) - V_C(t) = 0. \tag{4.23}$$

The voltage values across the lumped circuit components are $V_R(t) = I(t)R$, $V_L(t) = L\frac{dI(t)}{dt}$, and $V_C(t) = \frac{Q(t)}{C} = \frac{\int I(t)dt}{C}$. The driving circuit components will be denoted

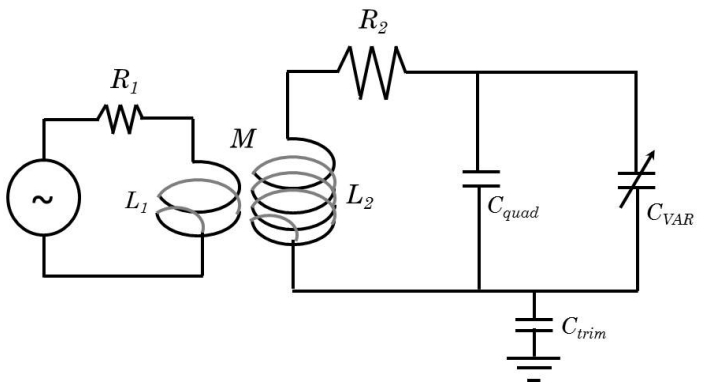

Figure 4.21: Simplified tank circuit diagram with lumped circuit components.

with subscript 1 and the secondary circuit components with subscript 2. Applying equation 4.23 to the circuit in Figure 4.21,

$$V(t) - I_1 R_1 - L_1 \frac{dI_1}{dt} + M \frac{dI_2}{dt} = 0, \tag{4.24}$$

$$M \frac{dI_1}{dt} - I_2 R_2 - L_2 \frac{dI_2}{dt} - \frac{\int I_2 dt}{C_2} = 0. \tag{4.25}$$

M is the mutual inductance between circuits 1 and 2, and thus the inductance term in equation 4.25 is the driving term for the circuit. In the first circuit, the driving voltage $V(t)$ produced is sinusoidal, and can be represented as $V(t) = Re[V_0 e^{i(\omega t + \phi)}]$, where ϕ is the phasor angle shown in Figure 4.20. At resonance, $\phi = 0$ without loss of generality. To find the currents in the two circuits, an ansatz,

$$I_1 = Re[A e^{i\omega t}], \tag{4.26}$$

$$I_2 = Re[B e^{i\omega t}], \tag{4.27}$$

is made for the solution of equations 4.24 and 4.25. After substituting equations

4.26 and 4.27 into equations 4.24 and 4.25,

$$[A(R_1 + i\omega L_1) - Bi\omega M]e^{i\omega t} = V_0 e^{i\omega t}, \tag{4.28}$$

$$[B(R_2 + i(\omega L_2 - \frac{1}{\omega C_2})) - Ai\omega M]e^{i\omega t} = 0. \tag{4.29}$$

By inspection, it is seen that the first few terms of each of these equations contain the complex impedances of each circuit, $z_1 = R_1 + iX_1$ and $z_2 = R_2 + iX_2$, where $X_1 = \omega L_1$ and $X_2 = \omega L_2 - \frac{1}{\omega C_2}$. Therefore, 4.28 and 4.29 simplifies to

$$Az_1 - BiM\omega = V_0, \tag{4.30}$$

$$Bz_2 - AiM\omega = 0. \tag{4.31}$$

Solving this system of equations,

$$A = \frac{V_0}{z_1 + \frac{\omega^2 M^2}{z_2}}, \tag{4.32}$$

$$B = \frac{i\omega M V_0}{z_1 z_2}. \tag{4.33}$$

These are the current amplitudes in circuits 1 and 2, respectively.

4.4.2 Design of the rf Box

A copper box (12"x12"x12") was constructed to enclose the rf circuit and isolate the radio frequency. 0.25" aluminum angle was used to form a rigid structure for the copper, with 0.01" gauge copper sheet bolted and soldered around the inside edges of the box to maintain uniform conductivity.

The rf circuit consists of an air-core inductor in parallel with both capacitor components: the capacitive quadrupole and a vacuum-variable capacitor. The variable capacitor serves to tune the resonant frequency of the circuit, spanning about

5 MHz in the frequency domain. An Agilent E5061B impedance analyzer [63] was used to measure the capacitive range for the variable capacitor in the frequency ranges of the experiment. The measurement shows a range of capacitance values between 33.7 pF and 89.4 pF at a frequency of 36.9 MHz. This capacitor is suspended in the rf box with ceramic standoffs, and an insulated plastic rod to tune the circuit is fed through to the outside of the box and connected to the capacitor's tuning knob with a barrel connector.

The air-core inductor in the primary circuit was constructed with 0.25" copper tubing wound around a 2" diameter mandrill on a lathe. A series of inductors were made for each resonant value as determined in envelope simulations of Chapter 3. As long as the coil length-to-radius ratio is greater than 0.67, the inductance (in μH) of a single-layer air-core inductor is

$$L = \frac{0.394 r^2 N^2}{9r + 10l}, \tag{4.34}$$

where r is the coil radius in cm, N is the number of turns in the coil, and l is the coil length in cm [62]. This equation is used to construct the inductor using the capacitance values that have already been measured.

As an example, the inductance value for the 21 mA beam resonance is found by adding the measured lumped quadrupole capacitance and the median value of the variable capacitance, using equation 4.18, and solving for L. This value is

$$\begin{aligned} L &= \frac{1}{(C_{quad} + C_{var})(2\pi f_0)^2} \\ &= \frac{1}{(23.7pF + 61.5pF)(2\pi(36.9MHz))^2} = 0.32\mu H. \end{aligned} \tag{4.35}$$

A 2" diameter mandrill is used to construct the inductors, and the length and

number of turns must be varied in order to achieve the desired inductance. The Q value is largely determined by the inductive component in a resonant circuit, and the optimal Q occurs when the length of the coil is equal to its diameter [62]. Thus, an inductor of length 2" is used, and the necessary number of turns is

$$N = \frac{\sqrt{L(9r + 10l)}}{r\sqrt{0.394}} = \frac{\sqrt{0.22(9(2.54) + 10(5.08))}}{2.54\sqrt{0.394}} = 2.52. \tag{4.36}$$

To form the inductor of the primary circuit, 0.25" copper tubing was formed into a 3" diameter half-turn. This inductance provides the driving mutual inductance of the secondary circuit. A schematic of the rf tank circuit is shown in figure 4.22. After all of the circuit components were constructed, ceramic standoffs were used to position the components near the center of the box. Carefully cut 0.01" copper sheet with rounded corners is used as the wiring between circuit components. To position the rf box on the 6" flange at RC9, "Fingers" are cut into the bottom of the box alongside an array of holes for the screw heads of the flange. The fingers are bent up and the $2\frac{3}{4}$" flange fits in the opening, secured with a hose clamp. A picture of the constructed circuit is shown in Figure 4.23.

4.4.3 Required Power Input

Using the values from the previous section for the rf box design, the power input needed for the circuit and the expected Q value is determined. Ohm's power law for an AC circuit states that

$$P = I_{rms}^2 R_{AC}. \tag{4.37}$$

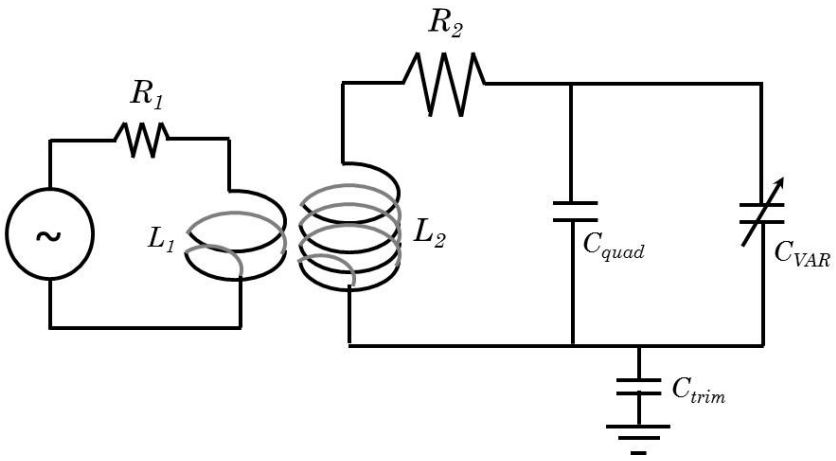

Figure 4.22: Schematic of the rf tank circuit.

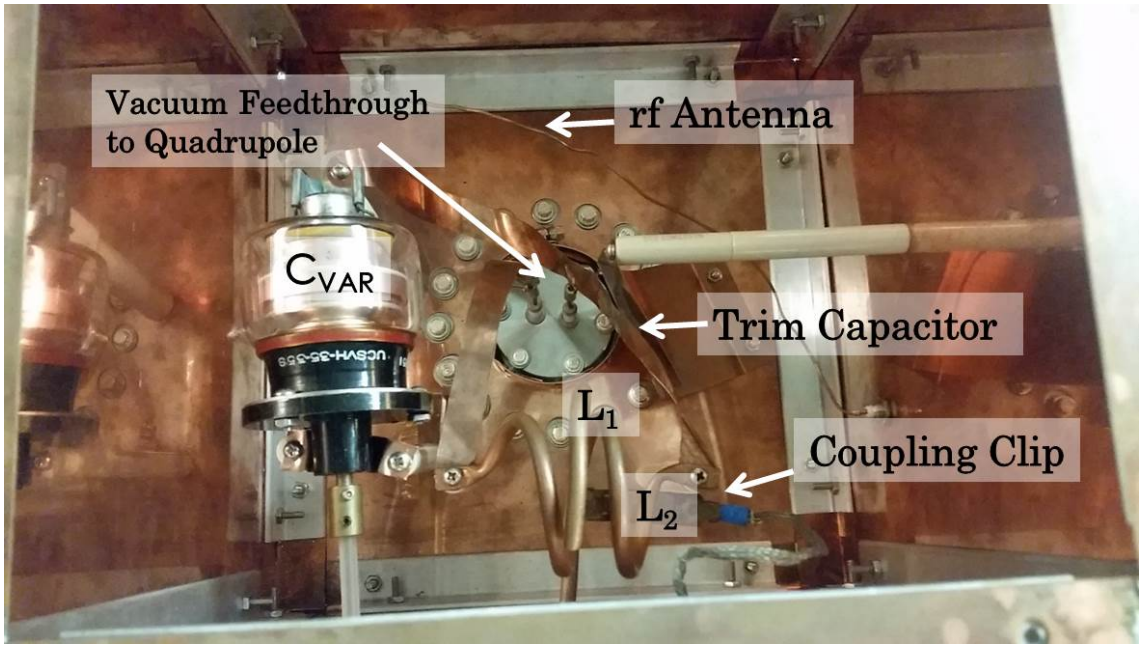

Figure 4.23: Constructed rf tank circuit.

At resonance, the coupling impedance between the primary and secondary circuits is a purely resistive 50Ω. This means that all power is transmitted to the secondary circuit, and there is no reflected power. In this case, P is the input power from

the primary circuit, and is the power dissipated in the resistance of the secondary circuit. Because the current density in the capacitors is much smaller than the current density in the inductor, it can be assumed that the resistive losses primarily occur in the inductor [58].

The resistance in the inductor's copper tubing is due to the skin effect [54]. This resistance is due to the frequency dependent skin depth in the copper tubing, and is described by

$$\frac{R_{AC}}{d} = \frac{1.044}{\pi}\sqrt{f_0}. \tag{4.38}$$

This resistance density, in mΩ/inch, is for 0.25" copper tubing of length d at frequency f_0, in MHz. Using the conservation of energy,

$$\frac{1}{2}LI^2 = \frac{1}{2}CV^2, \tag{4.39}$$

and substituting $V_{peak} = \sqrt{2}V_{rms}$, the required input power (4.37) is written as

$$P = \frac{R_{AC}CV_{peak}^2}{2L}. \tag{4.40}$$

With the inductor example used for equations 4.35 and 4.36 (0.22 μH), $R_{AC} \approx 31.3$ mΩ. Substituting this and $C = 85.2$ pF into equation 4.40, the power input needed is between 4.87 mW and 26.9 W. Using equation 4.19, the theoretical Q value is 1556. This value will be compared to the measured value in the next section.

4.5 Bench Tests of the rf System

Using an Agilent E5071C Network Analyzer, bench tests were performed on the tank circuit. In network theory, S-parameters measure the power transmitted to

the load. S11 measures the reflected power at the same port as the input, and S12 measures the power received at port 1 relative to the power input at port 2. The FWHM of the resonant peak in an S12 measurement provides a measured value of Q. The results of these measurements are shown in Figure 4.24.

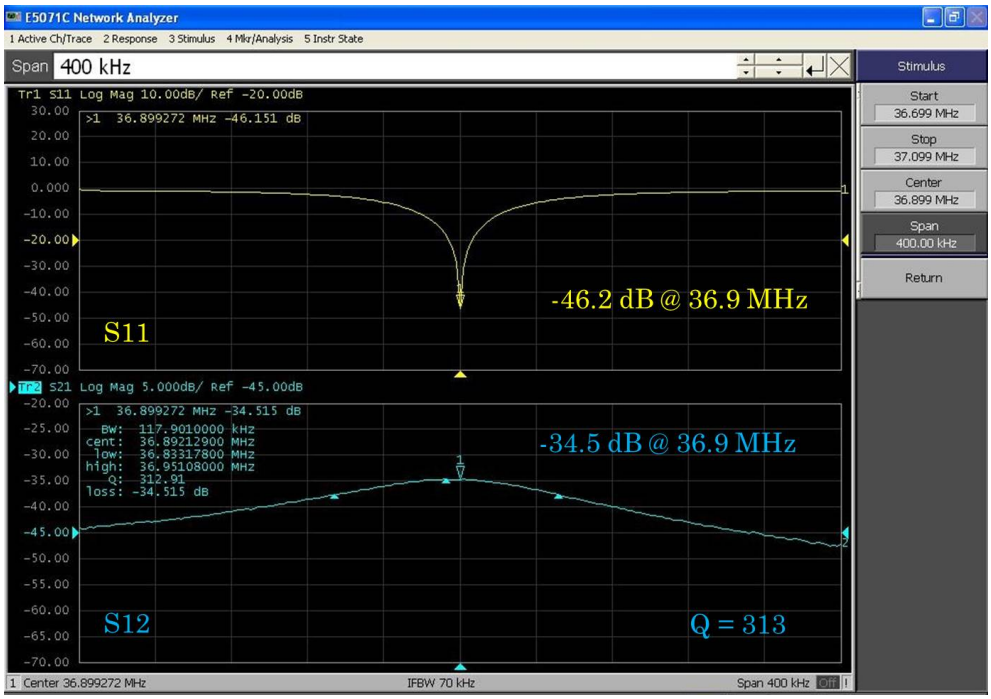

Figure 4.24: S11 and S12 measurements of the circuit at 36.9 MHz. The measured Q value is 313.

Another way to determine the Q of the circuit is to measure the time it takes, τ, for the voltage to drop by $1/e$ after removing power to the circuit. This time can be measured on the oscilloscope.

$$Q = \frac{1}{2}\tau\omega_0. \tag{4.41}$$

At 36.9 MHz, the oscilloscope output from the rf antenna is plotted in Figure 4.25. The time constant is consistent with the measurement by the network analyzer

shown in Figure 4.24, a Q of ~ 310

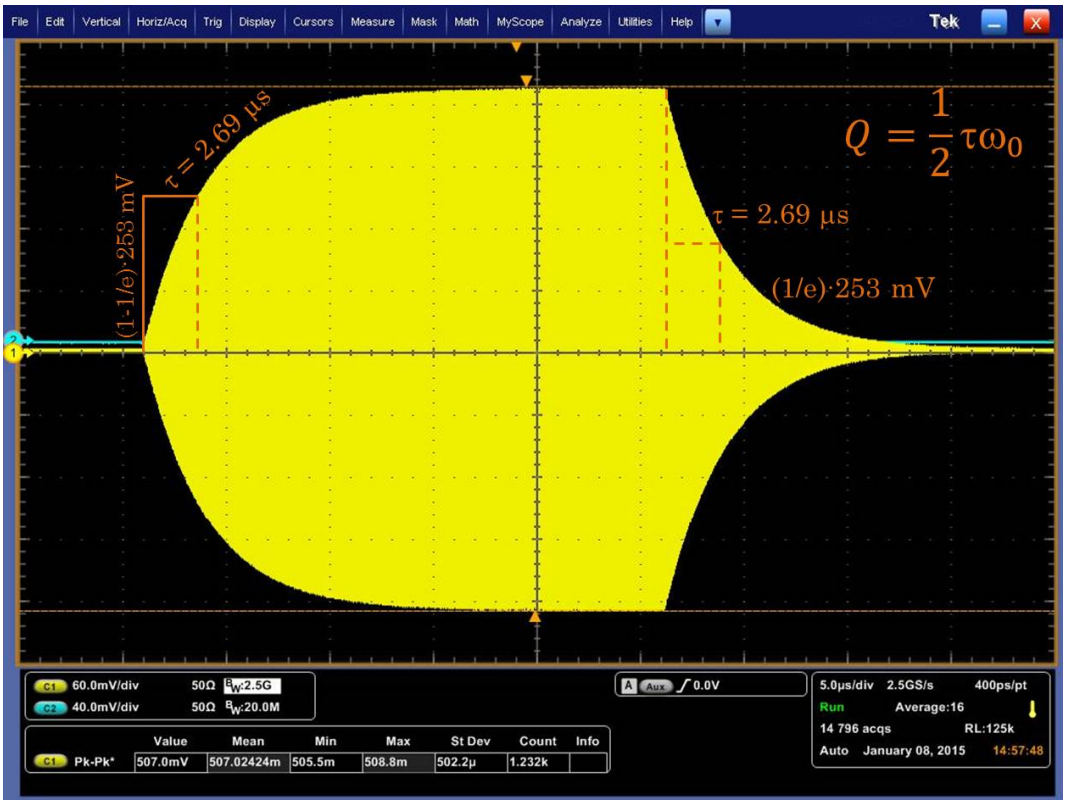

Figure 4.25: Scope measurement of the rf circuit using the rf antenna. The measured Q value is $\sim$310.

Using the measured Q, $R_{AC} = 37.7$ mΩ, a more accurate value calculated using equation 4.19. The input power into the tank circuit is 2 W by direct measurement. The voltage on each quadrupole electrode can be determined using

$$V_0 = \frac{2LP}{CR_{AC}}. \tag{4.42}$$

$V_0 = 630$ V. Using the conservation of energy, $I_0 = 10.3$ A. In terms of the required electrode voltage described in section 4.2.2, the induced $\Delta x' = 0.025$ radians, which falls between the predicted values of $\Delta x' = 0.001$ radians and $\Delta x' = 0.1$ radians.

Another measure of power transfer is the Standing Wave Ratio (SWR). The SWR is the ratio of power transmitted to the circuit of the power reflected from the circuit. At resonance, this value should be 1.0. The geometry of the coupling loop from the primary circuit dictates the robustness of the resonance. Therefore, a coupling clip as seen Figure 4.23 is adjusted until the SWR is 1.0. The measurement is shown in Figure 4.26. This is a quick way to see how much power is being transmitted to the circuit at a given frequency, and therefore it is used while collecting data during an experiment. This will be outlined in Chapter 6.

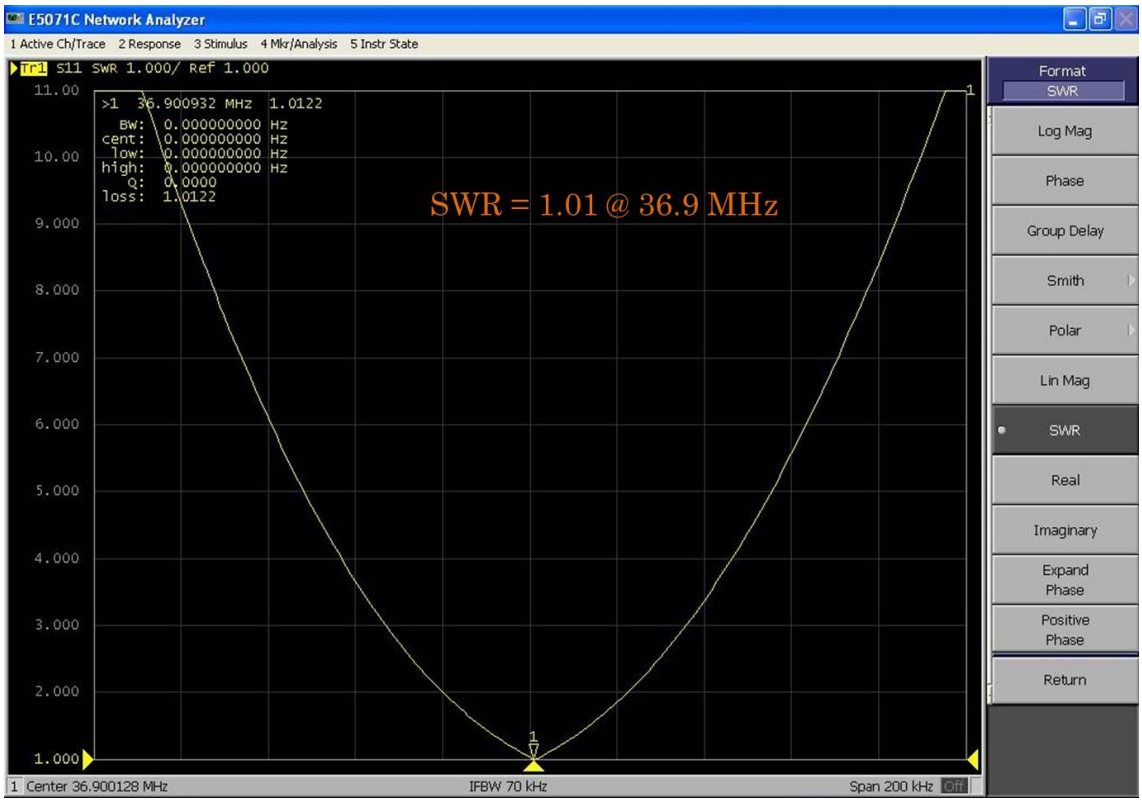

Figure 4.26: SWR Measurement of the power transfer at the 36.9 MHz resonance. With an SWR of 1.01, nearly all power is transmitted from the primary to the secondary circuit.

4.6 Installation in UMER

To prepare the quadrupole for installation into vacuum, it was chemically cleaned at the UMD Fablab using acetone, methanol, deionized water, and dry nitrogen.

The quadrupole was installed into RC9 as depicted in Figure 4.27. A Hipot test was used to ensure there was no dielectric breakdown up to 700 V between the quadrupole electrodes and ground and the electrodes themselves. After verifying the soundness of the electrical connections, the vacuum was brought down to 1.0e-5 Torr using first a roughing pump and a turbo pump. After the vacuum reached 1.0e-5 Torr, a series of ion pumps at each ring station were turned on around UMER to reach the final pressure of 2.0e-8 Torr.

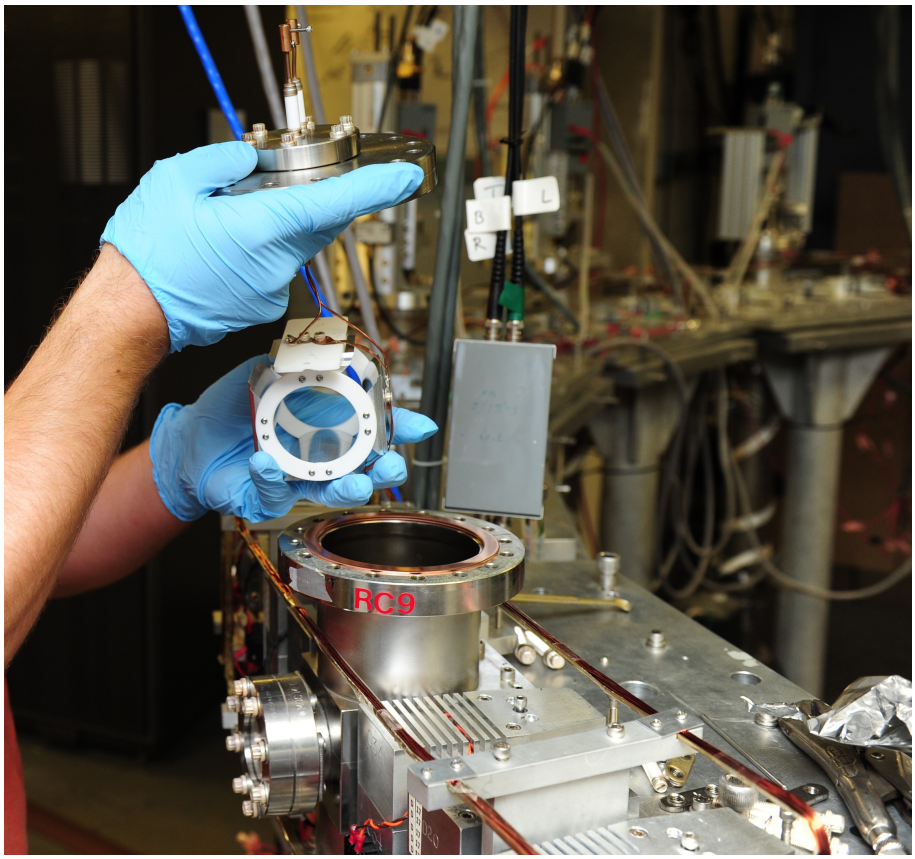

Figure 4.27: Installing the quadrupole at RC9.

Chapter 5: Diagnostics

5.1 The Knockout Imaging Method

Upon exciting the quadrupole envelope mode in the electron beam, it is necessary to measure the growth of R_- to characterize the mode. An effective imaging diagnostic of the UMER beam called the knockout method [23] is used. This method has been shown to accurately measure the beam loss profile in the electron beam [65]. A diagram of the knockout method is shown in Figure 5.2. By using a digital timing system, a 300 ns, 3 kV electric dipole pulse can knock the entire beam from its equilibrium orbit and into a fast phosphor screen. This screen does not have any image hysteresis or "memory", thus a properly timed gated camera can capture a 3 ns time slice profile of the beam.

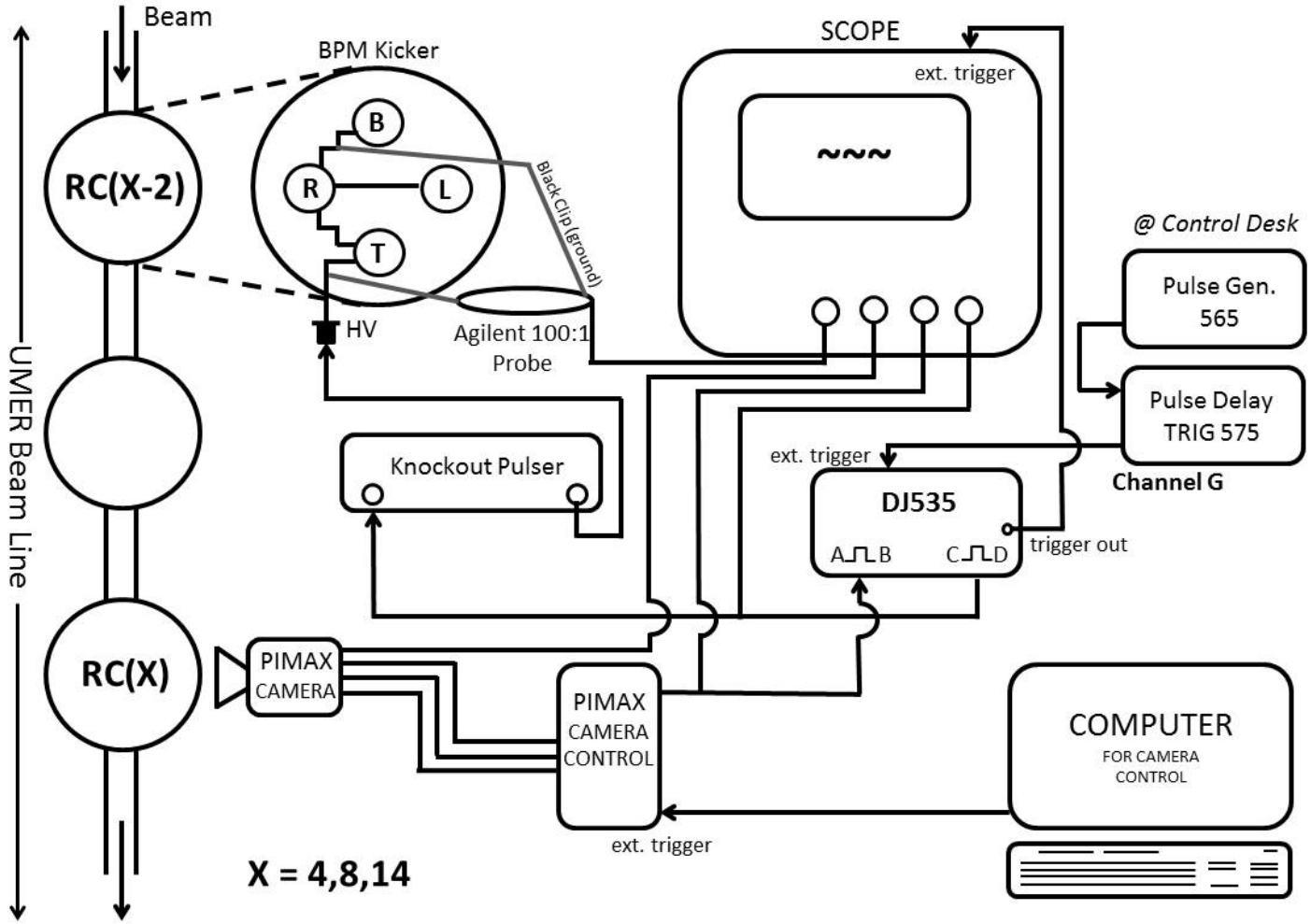

Figure 5.1: Circuit diagram of the timing system for the knockout pulser and camera.

5.1.1 Timing System

A well-choreographed timing system for the knockout method was put into place to capture precise images of the electron beam slices. This is detailed in Figure 5.1. The values for the delay box are given in Table 5.1. Using this time delay, the beam can be knocked out at any turn.

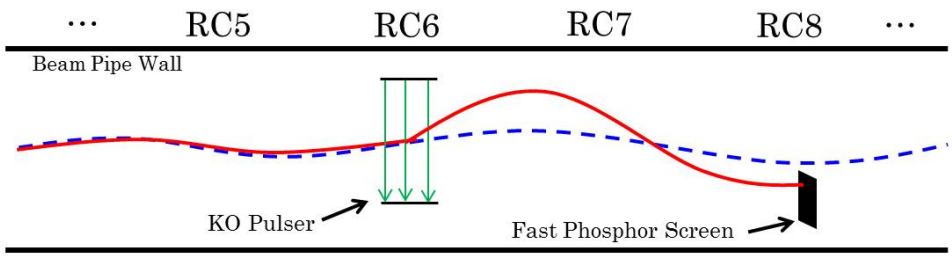

Figure 5.2: Schematic drawing of the beam knockout method. The blue dashed line represents the beam on a previous turn where the electric dipole field is off. The dipole is pulsed for 300 ns, deflecting the entire beam into the phosphor screen.

5.1.2 Fast Phosphor Screens

The fast phosphor screens used in this experiment produce light with intensity proportional to the intensity of the incident electron beam. The light is produced within a 3 ns response time, permitting very precise time slice images of the beam. There are three fast phosphor screens installed in UMER located at RC4, RC8, and RC14. In Chapter 3, it was shown how the data for this experiment can be collected from one location in the ring. For this dissertation, only the phosphor screen at RC8

Table 5.1: Time Delay Box Settings

Channel	Width (μs)	Delay (s)
A	4.96	0.00834754
B	0.850	0.00834654
C	136	0.00824115
D	295	0.0080886
E	15.0	0.008347481
F	0.200	Variable/Phase locking
G	0.500	0.00834833 (5^{th} turn KO)
H	0.500	0.00834713

is used.

It is necessary to align the phosphor screens at a 45 degree angle between the electron beam and the camera to get the most accurate picture of the beam. To calibrate this angle, the backside of the screen is equipped with fiducial marks as shown in Figure 5.3. Each fiducial mark is 5 mm across, but by perspective the horizontal marks are imaged more closely together. Using a simple geometric argument, the screen is at the desired 45 degree angle when the horizontal fiducial marks are $\frac{5}{\sqrt{2}}$ mm apart. This is found from imaging the fiducial marks with the PIMAX camera as shown in Figure 5.3, and measuring the pixel distances. Once the 45 degree angle is found, the screen must be rotated 180 degrees so that it is ready to image the beam. This 180 degree angle is added (or subtracted) from the

position of the screen that was empirically determined to be at 45 degrees.

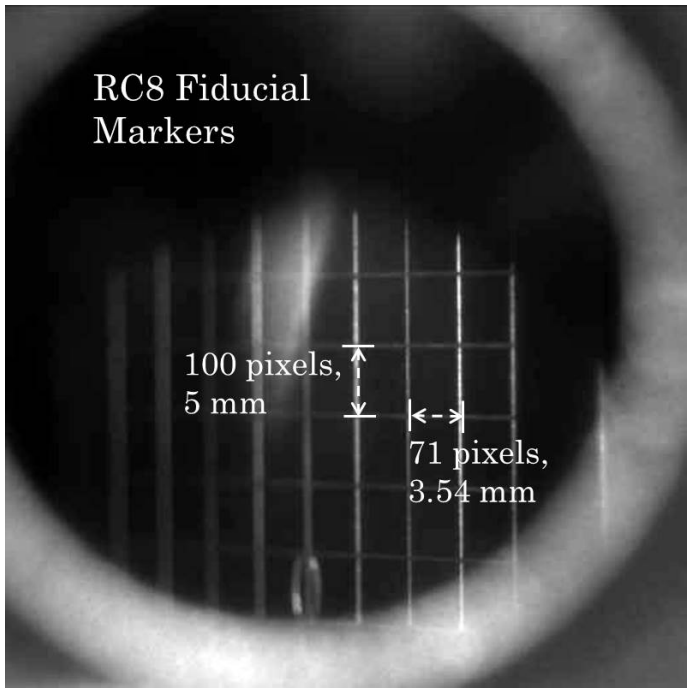

Figure 5.3: Fiducial marks on the back of the phosphor screen located at RC8. These are used to ensure there is a 45° angle between the camera and screen.

To position the phosphor screen, the beam position monitor (BPM) is first lifted up out of the beam pipe line. The phosphor screen is then slowly raised until it intercepts a portion of the beam, called scraping. A good diagnostic to measure the beam scraping is from the wall current monitor (WCM) located at RC10. Ideally the phosphor screen should be as close to the beam as possible without scraping it on any turn.

5.2 PIMAX Camera

Once the screen was in place, a 16-bit PIMAX2 ICCD camera developed by Princeton Instruments was used to image the beam [66]. This camera has a 512 x 512 pixel imaging array with pixel resolution on the order of 50 μm. The pixel resolution was determined by the number of pixels across the 5 mm vertical separation of the fiducial marks in Figure 5.3. This camera is also equipped with a 3 ns minimum gate width, permitting thin time slice images of the 100 ns[1] beam bunch.

The PIMAX camera was secured in place on an optical breadboard as shown in Figure 5.4. The camera is angled down to get a clear picture of the off-line fast phosphor screen. A black cloth (not pictured) is used to shield the camera from external light.

5.2.1 Camera Noise

To determine camera noise, light from the beam incident on the phosphor screen, a piece of computer paper was stapled to a piece of black construction paper with a hole punched in it. A flashlight illuminated the paper from behind, and the contrast provided a round beam-like image similar to the light produced by the phosphor from incident electrons. The setup is shown in Figure 5.5. Images were taken every 1.5 s for 30 minutes to see whether there is any noise in the electronics.

From the images, the moments of the "beam-like" image were taken. The centroids are shown in Figure 5.6 and the sizes are shown in Figure 5.7. It is shown

[1] at injection

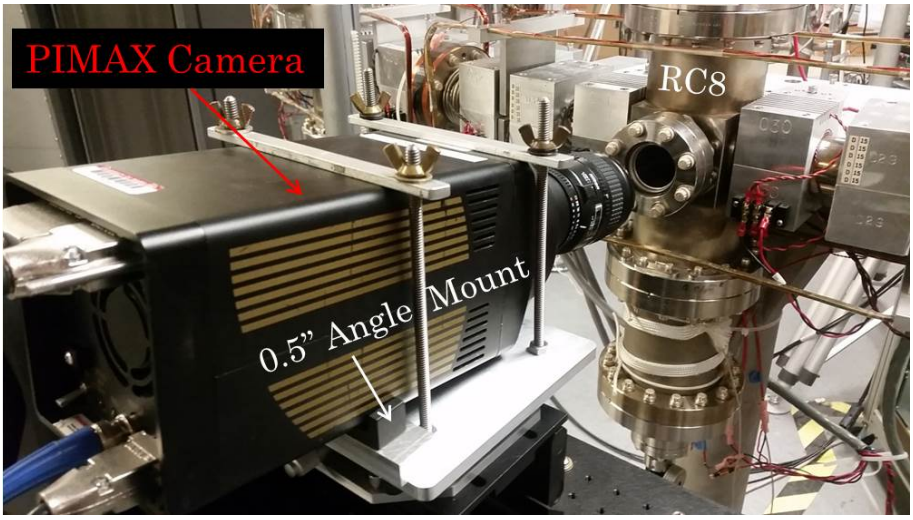

Figure 5.4: Camera setup for the experiment. Camera is angled down to capture the beam on the phosphor screen. During experiments, a black cloth (not pictured) is used to shield the camera from external light.

that the error fluctuation is smaller than a pixel size, suggesting consistent shot-to-shot data collection. This result shows that errors in the phosphor screen beam measurements are not due to the camera apparatus.

5.3 Other UMER Diagnostics

This section describes other necessary UMER diagnostics. These include the wall current monitor (WCM) and beam position monitors (BPMs). Current measurement in the WCM is important for calculating the space-charge ratio I/ϵ, and the BPMs helped to steer and match the beam (see Appendices A and B).

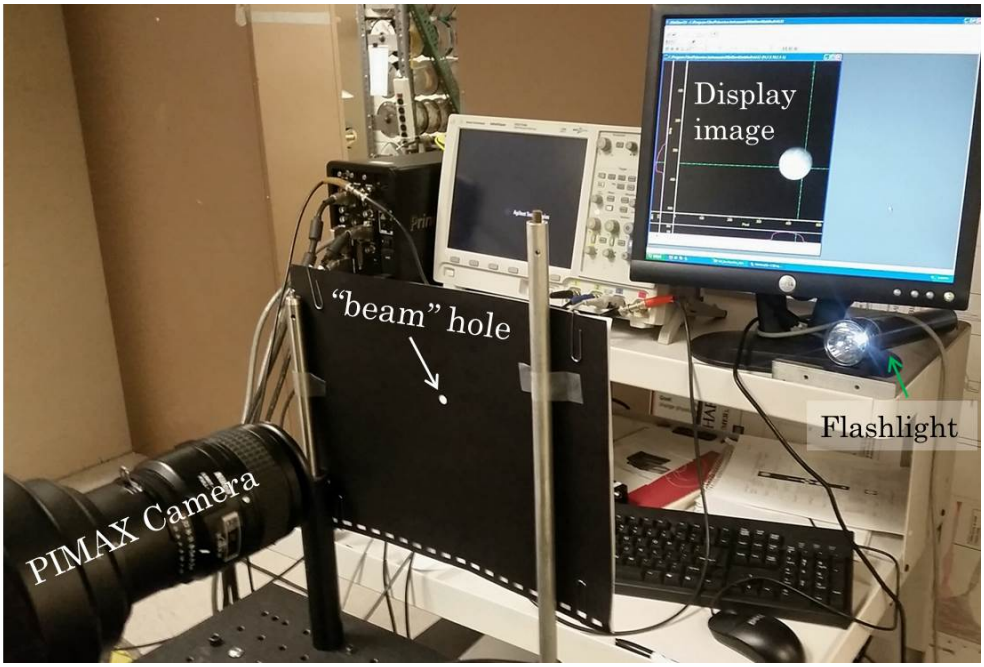

Figure 5.5: Experimental setup to measure the noise in the camera. The flashlight shining on the construction paper provides a beam-like image for the camera to capture. A black cloth (not pictured) is used to shield the camera from external light.

5.3.1 Wall Current Monitor (WCM)

A Wall Current Monitor (WCM) is used to measure electron beam current in UMER. Located in RC10, a diagram of the WCM is shown in Figure 5.8. The beam generates an image current in the beam pipe wall as it travels past the WCM. The equivalent resistance value of the WCM is 4.545 Ω, so the current is calculated from the scope by the equation

$$I_{WCM} = \frac{V_{WCM}}{4.545\Omega}. \tag{5.1}$$

The WCM is "ac-coupled" and can only measure the change in current over time, thus making it difficult to measure a "dc" beam. In UMER, bunch-end erosion

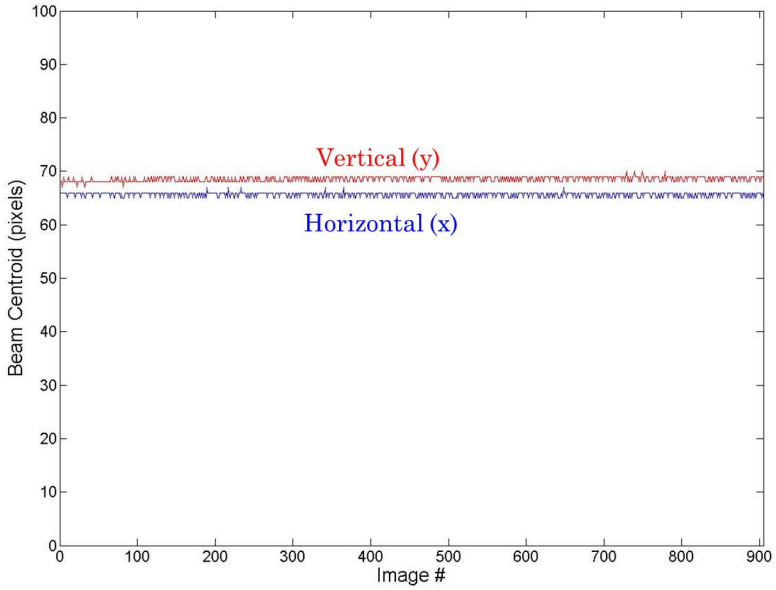

Figure 5.6: Centroids of the "beam-like" camera images. Images were taken at 2 second intervals for 30 minutes.

causes the head and tail of the beam to expand and pass through each other, losing information about the current [23]. However, it has been shown that this information is recovered using the knockout method [65].

5.3.2 Beam Position Monitors (BPMs)

Beam position monitors (BPMs) are housed at nearly every diagnostic ring chamber in UMER. An image of the BPM assembly is shown in Figure 5.9. Four BPM electrodes are arranged in a quadrupolar configuration around the beam pipe, labeled top, bottom, left, and right. As the beam passes through a BPM, the BPM picks up a voltage between each electrode and the charges in the bunch. This voltage is proportional to the distance between the beam bunch and the electrode.

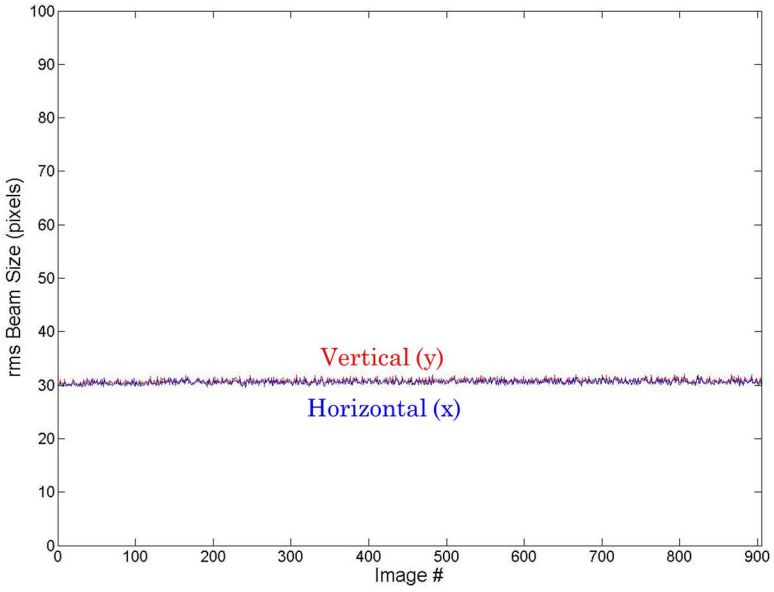

Figure 5.7: Sizes of the "beam-like" camera images. Images were taken at 2 second intervals for 30 minutes.

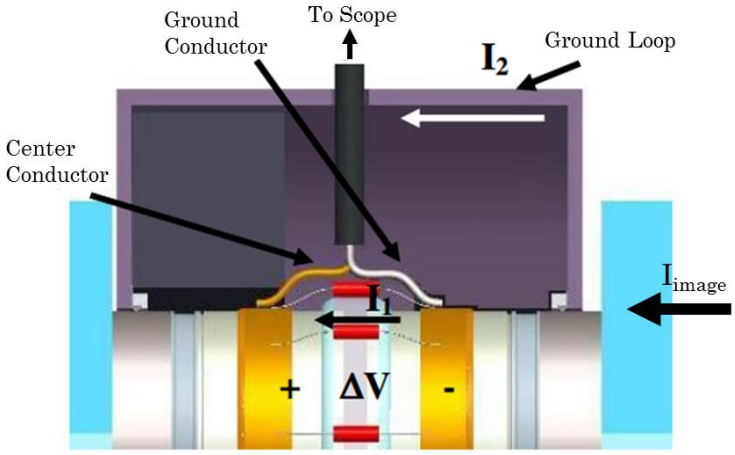

Figure 5.8: Diagram of UMER's wall current monitor (WCM) located at RC10. The image current from the beam divides through the ground loop and resistors (red), and the resulting voltage drop is measured by the scope [25].

A scope records the voltages from each of these electrodes. A comparison between the voltage values of the top and bottom electrodes and the right and left electrodes provide information about the location of the beam centroid to the center of the pipe. Once again, the BPMs are ac-coupled diagnostics, so it becomes difficult to measure beam displacement after the beam fills the ring.

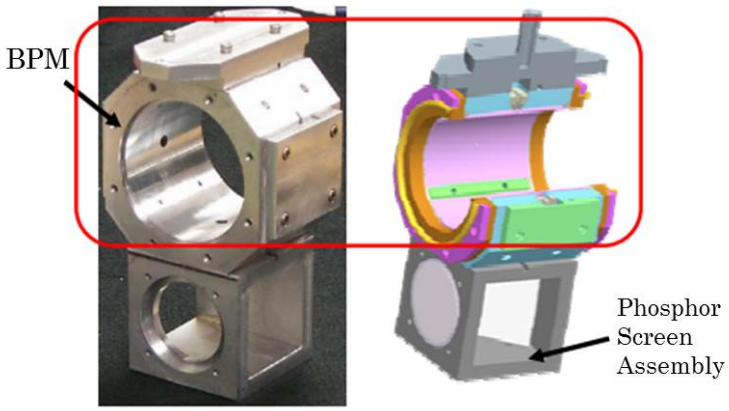

Figure 5.9: Diagram of beam position monitor (BPM) in UMER. A phosphor screen assembly is attached the bottom for use in first-turn matching experiments (see Appendix B) [25].

It doesn't matter how beautiful your theory is, it doesn't matter how smart you are. If it doesn't agree with experiment, it's wrong.

–Richard P. Feynman

Chapter 6: Experimental Observations of Envelope Resonance

In this chapter, experimental techniques are detailed and agreement to theory and simulations is explored. Multi-turn resonance is experimentally demonstrated using the rf-driven quadrupole and tank circuit described in Chapter 4 and the knockout imaging method described in Chapter 5.

6.1 Measurement Methods

Upon aligning UMER's knockout diagnostic system, beam measurements were taken. First, a background image is taken with the beam turned off. The intensity values from this image are subtracted from each beam image such that the image only contains intensity from beam-generated light. This background image contains less than 0.1% of the light intensity produced by the phosphor screens in an experiment.

The current from the wall current monitor (WCM) was then recorded. A sample picture of the 21 mA beam WCM signal[1] of the $V_{bias} = 30$ V beam is shown

[1] converted to current using $R = 4.545\ \Omega$

in Figure 6.1. Though reproducible, the zero-current baseline drifts in time. It is believed that this is due to ground loops in the electronics. Since the experiment is performed on a time-slice in the center of the beam, the current of the beam for each turn is measured from the center of the beam pulse to the zero-current baseline. The WCM data shows a longitudinal space-charge rarefaction wave that reaches the center of the beam pulse by turn 6. Due to this effect, the beam current in the center of the beam is reduced by 5.3% between turns 5 and 6. Since the space-charge-depressed normalized phase advance σ/σ_0 scales by I/ϵ (see equation 2.13), the space-charge-dependent envelope mode frequencies are affected by current loss. This greatly complicates the experiment. Thus, to avoid a time-dependent envelope mode frequency, the beam measurements for this experiment were taken before turn 6. Simulation results suggest that the resonance peaks become more well defined (taller, narrower) as the number of quadrupole perturbations, n, tends to infinity. Therefore, it is best to choose an n as large as possible. Limited by longitudinal space-charge effects, the data were collected on turn 5, following four consecutive quadrupole perturbations in turns 1-4. The time delay settings for the knockout image at turn 5 are shown in Table 5.1.

The knockout imaging method was used to collect beam slice images. Due to both the response time of the fast phosphor screen and the time-resolution of the PIMAX camera, 3 ns beam slice images of the beam are resolved. For a bunch length of 100 ns, this is 3% of the beam pulse, sampled at the center of the pulse to avoid the longitudinal space-charge effects at the ends. These beam slice images were taken on turn 5. To check the reproducibility of the beam measurements,

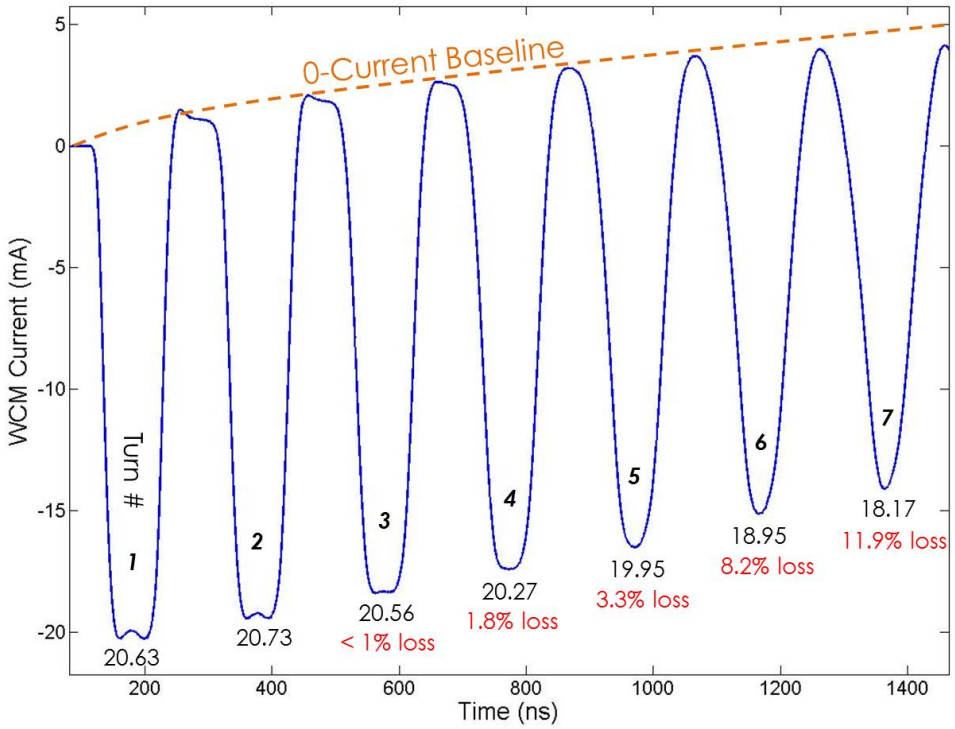

Figure 6.1: 21 mA beam current measured from the WCM. Bias voltage is 30 V. Beneath each beam pulse turn is the peak beam current, in mA, measured from the center of the beam to the time-dependent 0-current baseline. The red percentages represent the current lost from injection.

images were collected every 1.8 seconds for 30 minutes and image moments[2] were computed. The results are shown in Figures 6.2 and 6.3. There is a long-term drift in the beam centroids on the order of 4.8% over 30 minutes, however, the rms beam size does not drift. This is a desirable result because the valuation of the envelope mode resonance depends on precise measurements of the X_{rms} and Y_{rms} beam size. The standard deviations calculated from these data are $\sigma_{X,rms} = 0.137$ pixels and $\sigma_{Y,rms} = 0.174$ pixels, where each pixel is 50 μm. These values are used for rms

[2]beam centroid and size

beam size error analysis.

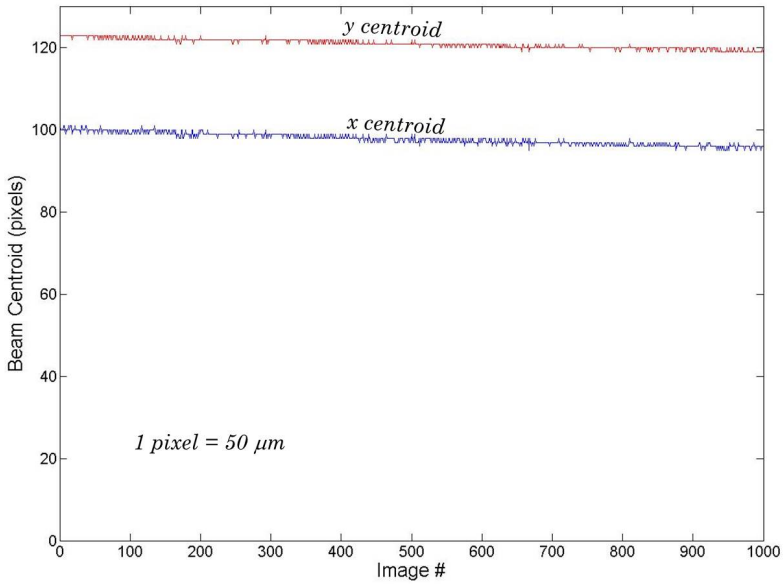

Figure 6.2: Drift behavior in the centroid moments of the 5^{th} turn knock-out images. Images were taken at 1.8 second intervals for 30 minutes.

After setting up the camera and recording a background image, the tank circuit in the rf box was tuned to the desired driving frequency. This was accomplished by measuring the standing wave ratio (SWR) of the secondary tank circuit by connecting the primary circuit inductor L_1 to the Agilent network analyzer. The average SWR value recorded during the experiment is 1.05, which means that 99.9% of the input power is transmitted to the circuit [71]. Transmitting all input voltage through to the rf circuit ensures that there is no impedance mismatch which can lead to transmission line losses.

The rf pulse train is phase locked to UMER's master oscillator and turned on sufficiently early to allow the tank circuit to attain a steady state before the beam

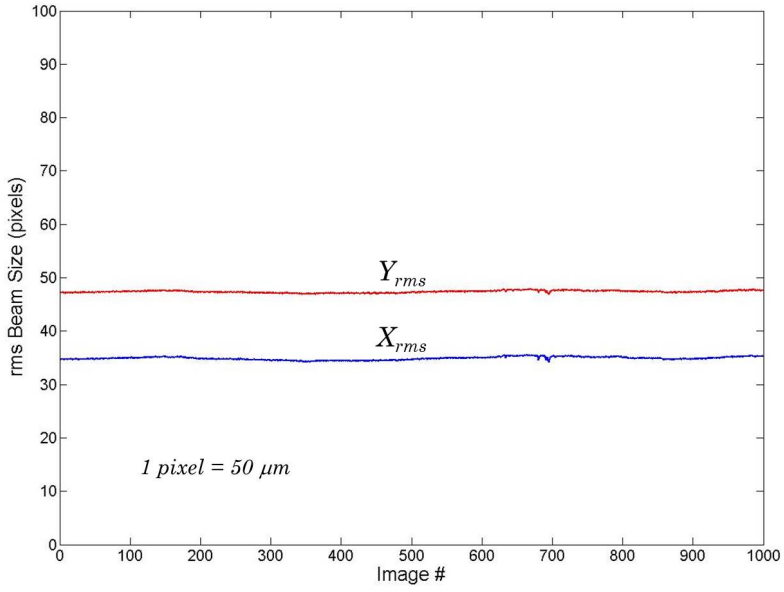

Figure 6.3: Drift behavior in the rms beam spot size moments of the 5^{th} turn knockout images. Images were taken at 1.8 second intervals for 30 minutes.

interacts with the quadrupole. The input power to the tank circuit is adjusted through the function generator. Each time the frequency is changed, the input power must be adjusted such that a constant peak voltage is maintained across the quadrupole electrodes. To monitor input power, an rf antenna measures the relative radiated power in the tank circuit and displays it as a voltage on an oscilloscope. A constant peak electric field at all rf driving frequency is the goal.

Unfortunately, there is no way to directly measure the voltage developed on the quadrupole. A probe directly attached to the electrodes would act as an electric load, consuming electric power. To determine the correct voltage to transmit to the tank circuit. The rf driving frequency was set to the calculated value of resonance

(36.9 MHz), and 3 ns transverse beam slice images were measured for a range of input voltages. The X_{rms} and Y_{rms} beam size moments were calculated and plotted as a function of peak-to-peak rf antenna amplitude in Figure 6.4. It is seen that after 500 mV, the envelope growth becomes nonlinear. Thus, to avoid nonlinearities, a peak-to-peak voltage output of 500 mV was chosen. This value provides the maximum rms envelope perturbation while remaining in the linear regime.

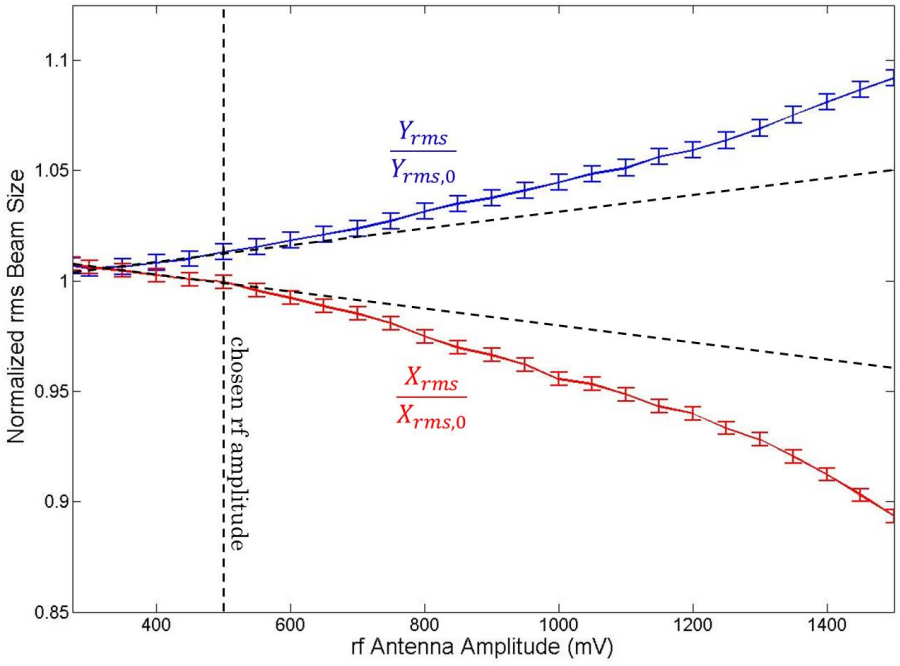

Figure 6.4: Normalized rms beam size as a function of peak-to-peak rf antenna amplitude for an applied rf frequency of 36.9 MHz. Horizontal dashed lines represent the linear regime, and the vertical dashed line represents the chosen rf amplitude, used for all experiments in this dissertation.

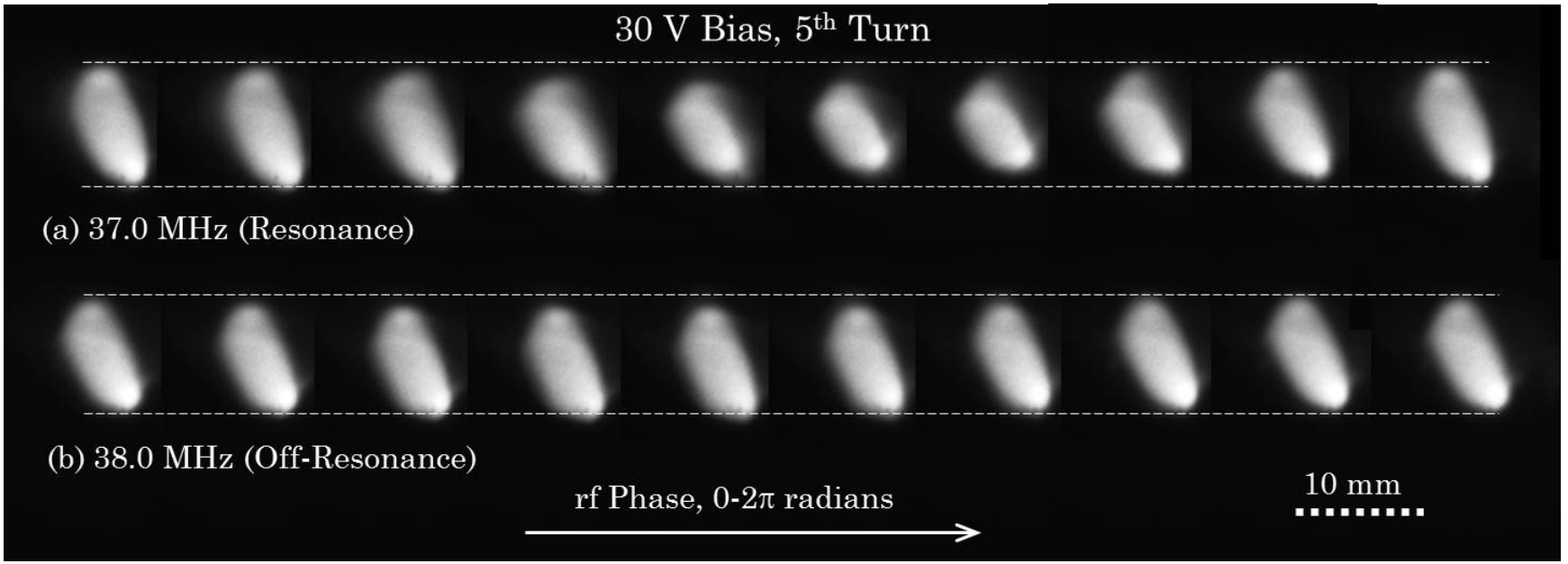

Figure 6.5: Images of 3 ns transverse beam slices after a small perturbation is applied for 4 turns over a range of applied rf quadrupole phases for the 21 mA beam excited (a) on resonance and (b) off resonance. Horizontal dashed lines are in place to train the reader's eyes to the applied perturbation. The UMER bias voltage is 30 V.

Since the tunable capacitor must be adjusted by hand, the experiment cannot be entirely automated. However, once the resonant frequency of the tank circuit is set to the desired value, a 360° sweep across rf phase is automated using a Matlab script, permitting an image collection rate of 10 images per minute. The lowest rf frequency (longest period) used in the experiment is 35.6 MHz, a period of 28.1 ns. The range is established by the inductor in the secondary tank circuit. For one phase scan, twenty images are captured, corresponding to a time delay step of $28.1/20 = 1.4$ ns. In terms of rf phase, this is $2\pi/20 = 0.31$ radians. The camera integrates over 50 iterations of 3 ns exposures to produce a single image. A 1.5 s delay is programmed between images to allow the camera to complete the integration.

In Figure 6.5, an rf phase scan of images is shown for two frequencies, 37 MHz (on resonance) and 38 MHz (off resonance). Each image represents an rf phase progression of 36°. Due to mismatch in the UMER beam, the beam is skewed and non-circular at RC8 on the 5^{th} turn. Since the beam has a larger vertical than horizontal rms size, the radially-dependent electric forces in the quadrupole[3] apply a greater perturbation to the beam in the vertical direction. As a result, the quadrupole mode perturbation shows up most prominently in the vertical axis. Vertical translations exist for both frequencies. This can be due to the beam not traversing the center of the quadrupole or the unstable adjustment of the quadrupole voltage (see section 4.3.2). However, a beam size perturbation is only evident in the resonant case. The applied peak-to-peak perturbation in the beam excited on

[3]see Figure 4.10

resonance is $\sim 22\%$ of the rms beam size in the vertical direction. This perturbation can be difficult to see, so a set of horizontal dashed lines are included to train the reader's eye to the applied perturbation. As the vertical perturbation compresses the beam (see images 4-8 in the top row), horizontal wisps resembling beam halo are seen. This is a simultaneous expansion in the horizontal rms beam size and compression in the vertical beam size, characteristic of a quadrupole perturbation.

The range of frequencies used in this experiment is 35.6 MHz to 40.6 MHz, with a frequency step of 0.2 MHz. With 20 images taken per frequency, 520 beam slice images are taken per experiment. The frequency range is limited to 5 MHz due to using a single inductor for the experiment. Multiple inductors could have been used to increase this range, but disturbing the rf box during an experiment may introduce errors in the circuit components (trim capacitor, rf antenna, etc.). A frequency range was empirically chosen to have two full resonant peaks present at $V_{bias} = 30$ V. Peak spacing is a good measure of agreement between simulation and experiment.

6.2 Data Analysis

The images are processed through a Matlab script. After the background image is subtracted from each beam slice image, the moments as described in Chapter 2 are calculated numerically using an algorithm from reference [72]. After the image moments are found, the beam is then cropped and the image moments are re-calculated. To ensure a consistent comparison between images, the cropping win-

dow is only calculated for the first image and then held constant. The cropping window is calculated by

$$w_{start} = w_{center} - 2.5w_{rms}, \tag{6.1a}$$

$$w_{length} = 5w_{rms}, \tag{6.1b}$$

where w represents x or y. The oversized window ensures that the entire beam is captured even for images from beams with resonant perturbations that exhibit large transverse centroid displacements.

After the moments are re-calculated, the rms beam size results for a single rf phase scan are plotted. This is shown in Figure 6.6. The out-of-phase rf oscillation between x and y is characteristic of a quadrupole perturbation. It is seen that the X_{rms} phase oscillation is not quite 180° out of phase as was shown in the envelope solver simulation. This is believed to be due to the skew of the beam. The magnet lattice of the ring imparts angular velocity to a skewed beam that couples x and y [44]. The larger perturbation in the y direction reflects what is seen in the transverse beam slice images of Figure 6.5. Since the perturbation is larger in y than in x, the following results will solely explore Y_{rms} values to identify the resonance structure of the quadrupole envelope mode.

For each phase scan as shown in Figure 6.6, the ΔY_{rms} value is recorded and plotted as a function of frequency. For $V_{bias} = 30$ V, the results of ΔY_{rms} as a function of rf frequency are plotted on top of normalized simulation results in Figures 6.7 and 6.8. Both Figures show good agreement between experiment and simulation. Figure 6.7 shows the peak displacement comparison between the

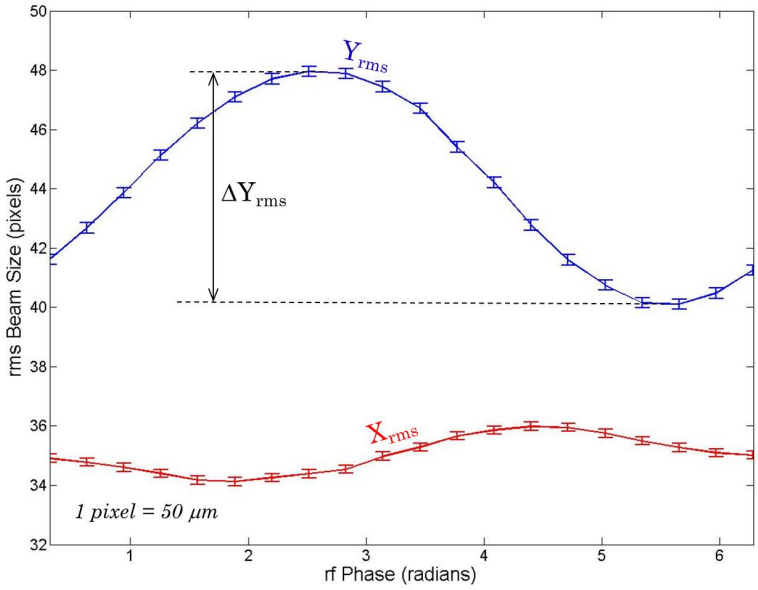

Figure 6.6: Example of rms beam size moment calculation of an experimental rf phase scan. The vertical (y) has a larger radius and thus a larger amplitude oscillation than the horizontal (x). The out-of-phase oscillation between the two dimensions is characteristic of a quadrupole mode perturbation.

envelope solver simulation and the experiment. They differ by 0.0 MHz and 7% for the frequency and peak widths, respectively. The peak displacement between the toy model simulation and the experiment is 0.25 MHz, and the peak widths differ by 21%. Figure 6.8 shows the peak displacement comparison between the envelope solver simulation and the experiment. They differ by 0.4 MHz and 7% for the frequency and peak widths, respectively. The peak displacement between the toy model simulation and the experiment is 0.2 MHz, and the peak widths differ by 9%. Considering the toy model is a simplified smooth focusing approximation, this is a remarkable result.

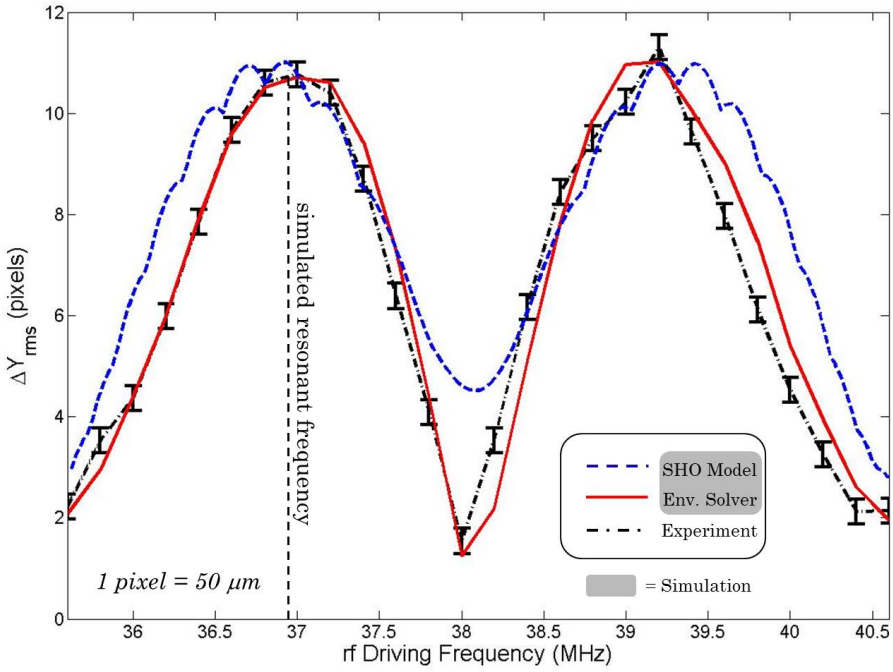

Figure 6.7: Experimental resonance structure for $V_{bias} = 30$ V plotted on top of normalized simulation results for $f_0 = 36.9$ MHz. Each point represents the change in rms beam size across a phase scan at each frequency.

The peaks in Figures 6.7 and 6.8 are not at the resonant frequency values, however their positions converge to delta functions at these values as the number of quadrupole perturbations tends to infinity.

It is seen that there is a degeneracy in determining the value of natural quadrupole mode frequency from the plots. This is further clarified in the dispersion relation plot of Figure 6.9. Using resonant mode excitation, it is not possible to determine the resonance peak that represents the true natural frequency. However, tomographic measurements of the emittance demonstrated at UMER [28] have

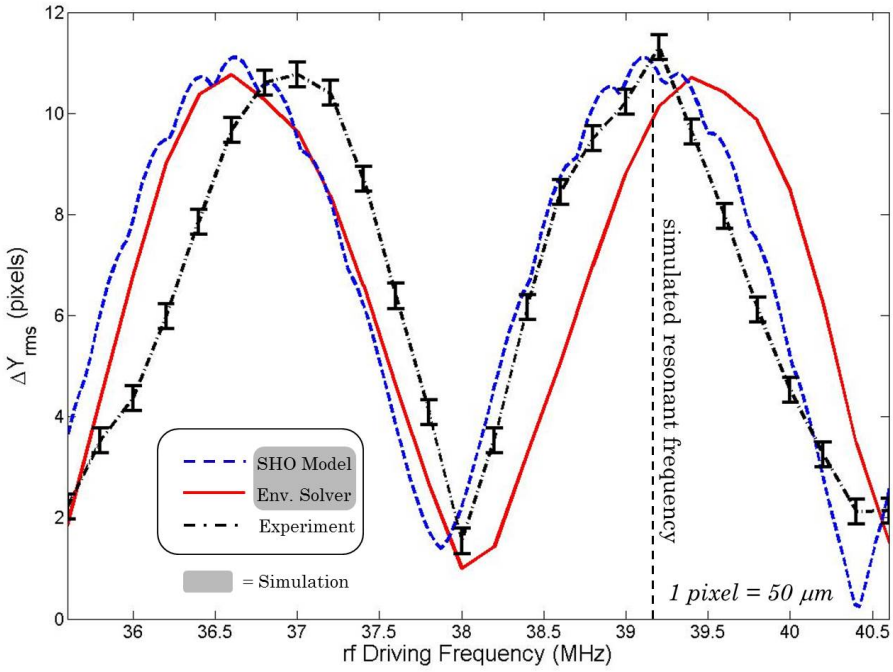

Figure 6.8: Experimental resonance structure for $V_{bias} = 30$ V plotted on top of normalized simulation results for $f_0 = 39.2$ MHz. Each point represents the change in rms beam size across a phase scan at each frequency.

determined that the natural mode frequency lies closest to the peak at 39.2 MHz, corresponding to the simulation results in Figure 6.8. An experimental measurement of the emittance at injection, called the pinhole scan method, will be used to confirm that the experimentally measured natural mode frequency corresponds to the peak at 39.2 MHz.

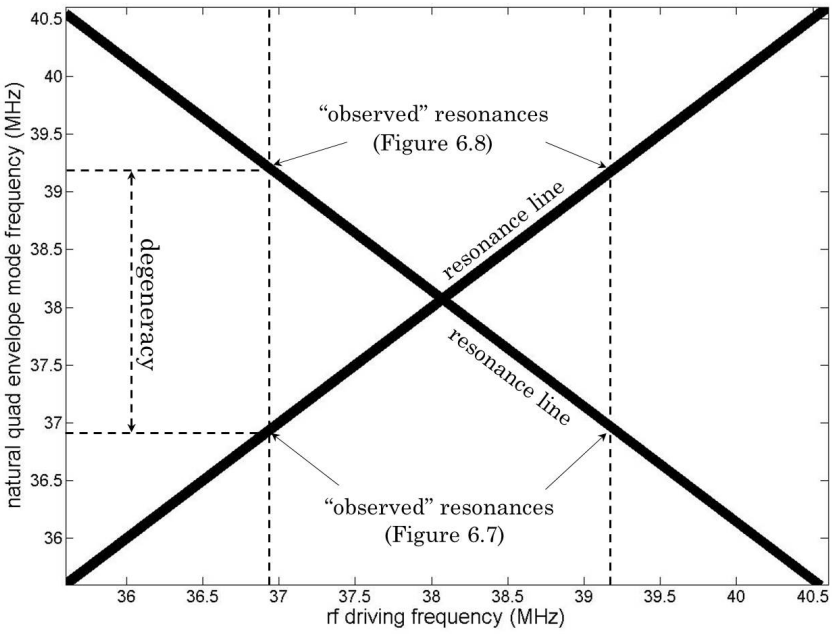

Figure 6.9: Resonance structure plot for the values of rf driving frequency used in this dissertation. Simulation values of natural frequency as used for Figures 6.7 and 6.8 reflect a degeneracy in the resonance structure.

6.3 Emittance Determination

Section 3.3.4 discussed how emittance can be inferred from the envelope solver simulations. Using the measured value of frequency f_0, the unnormalized emittance is calculated by

$$\epsilon_{I_0} = 4.58 f_0 - 138.8, \tag{6.2}$$

the units of which are in mm-mrad. This emittance is only valid for the current used in the simulation, I_0. To find the actual emittance, it must be normalized as

$$\epsilon = \epsilon_{I_0} \frac{I}{I_0}, \tag{6.3}$$

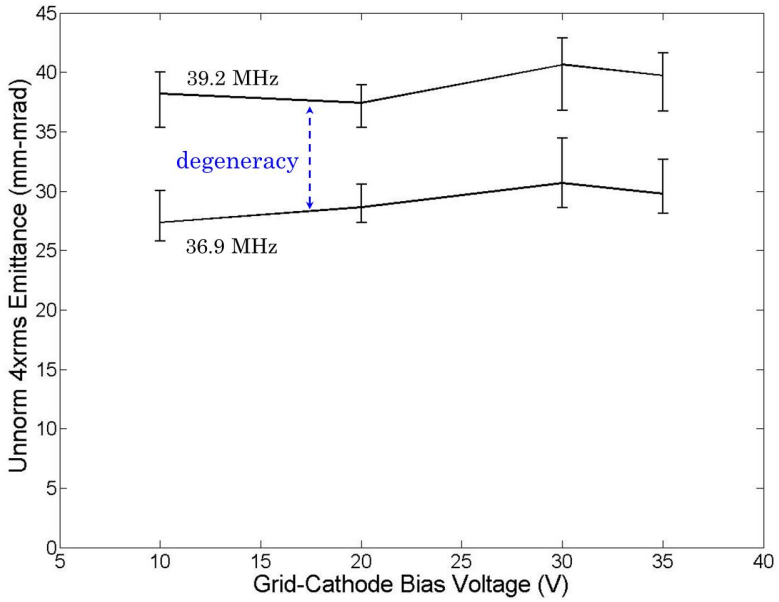

Figure 6.10: Experimental results of inferred emittance from measured values of resonant frequency for a range of bias voltages. The degeneracy in the measurement is shown for the two possible values of quadrupole mode frequency. The error bars reflect 5-10% measurement uncertainty.

where I is the current measured in turn five by the wall current monitor.

To test the emittance dependence on the mode frequency, the experiment and analysis are performed for a range of bias voltages. As explained in Section 4.1 and [49], the emittance is dependent on the bias voltage between the cathode and the cathode grid. There is no absolute dependence of emittance on bias voltage, but a change in bias voltage will cause a change in emittance. Upon finding the resonant frequency values from the resonance structure plots, the emittance for each bias voltage is calculated. The results are plotted in Figure 6.10.

The error σ_ϵ from the current is determined from the percent loss by beam current spreading out in the ring due to space-charge (see Figure 6.1). The method

Table 6.1: Quadrupole mode envelope resonance method results

Grid Bias (V)	Emitt. ϵ (mm-mrad)	$\sigma_{\epsilon,lower}$ (mm-mrad)	$\sigma_{\epsilon,upper}$ (mm-mrad)
10	38.2	2.8	1.8
20	37.4	2.1	1.5
30	40.6	3.9	2.3
35	39.7	3.0	1.9

of determining error in the envelope mode frequency value f_0 is biased toward the tendency for the simulation peaks to preferentially shift as the number of quadrupole perturbations tends to infinity. The error for the emittance ϵ is propagated from these two measurement errors [67]. This value is found to be 5-10% of its actual value, a weighted error as described in the previous section. Values of the emittance and errors are shown in Table 6.1.

6.4 Pinhole Experiment

Measurements of the velocity spread of the beam were performed using the pinhole scan technique [28]. The pinhole is the first UMER aperture setting listed in Table 4.2. The pinhole is 0.25 mm in diameter, producing a beam with negligible space-charge. The particles in this beam move in straight lines. As shown in Figure 6.11, a phosphor screen 28.4 cm downstream intercepts the beam. The beam centroid and spot size moments were measured from the resulting image and compared to the results of the quadrupole envelope resonance method. The pinhole

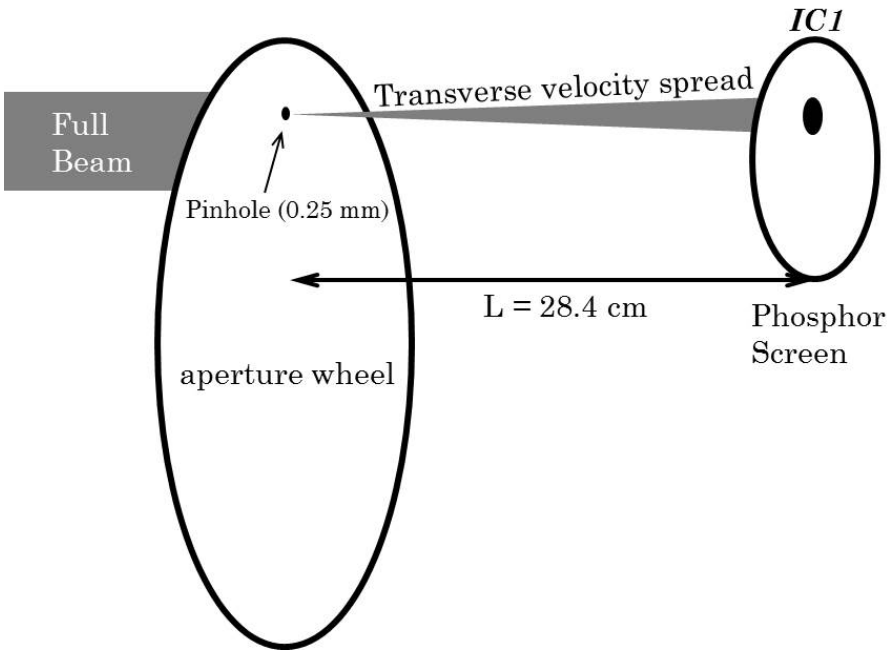

Figure 6.11: Conceptual drawing of the pinhole scan emittance measurement technique.

method is analogous to the pepper pot method of measuring emittance, except there is a moveable pinhole instead of a lattice of pinholes. This technique is preferable because it avoids overlapping beams.

Figure 6.12 shows sample images collected for the pinhole scan experiment for various aperture wheel settings. The hatch pattern in the images is a result of the interaction of the beam with the anode grid. A 1° rotation of the geared knob turns the aperture wheel by a small amount. Since the diameter of the wheel is large compared to the diameter of the beam, the 1° knob rotation corresponds to a linear translation of the pinhole by 0.1 mm. The smallest increment the knob can be rotated is 2°. The full beam radius can be measured with a single pinhole scan. Propagating the beam through the pinhole aperture is equivalent to inspecting thin

(0.25 mm) slices in y of the beam's trace space.

Since the aperture of the 21 mA beam is located at its center, emittance measurements are also taken relative to the center of the full beam. To find the full beam's center, the pinhole displacements for the edge of the beam are averaged.

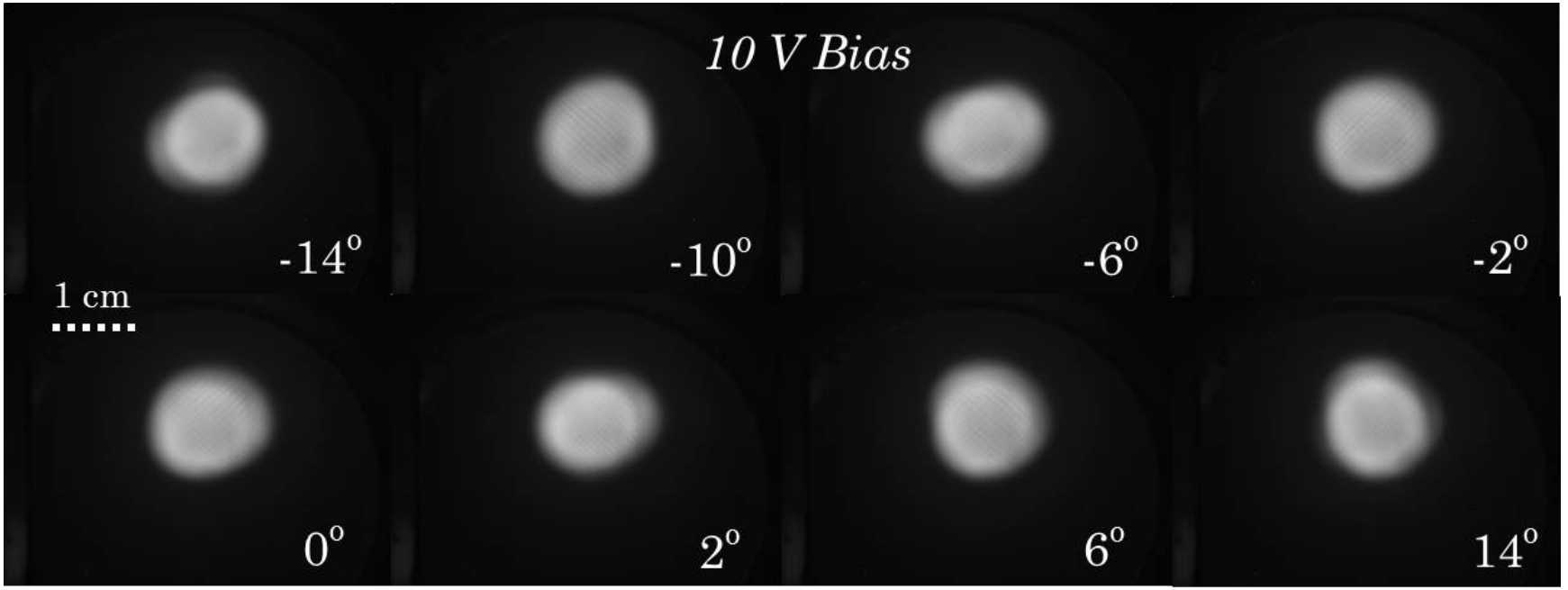

Figure 6.12: Sample images of the V_{bias} = 10 V pinhole scan. Every 1° corresponds to a 0.1 mm linear translation of the aperture. The hatch marks in the images are generated by the beam's interaction with the electron gun grid.

Let L be the displacement between the aperture and the screen. x_0 and y_0 are defined as the coordinates of the 0 mm displacement beamlet's centroid moment. x_c and y_c are defined as the coordinates of any given beamlet's centroid moment. The aperture coordinate system is defined as (x,y). A movement in the aperture wheel corresponds to a movement in the y direction. Thus, the divergence y' is

$$y' = \frac{(y_0 - y_c) - \Delta y}{L}, \tag{6.4}$$

and it can only be calculated in the y direction. The beam divergence was calculated for the images in Figure 6.12, and the results are plotted in Figure 6.13. The scatter is a direct result of the grid intercepting the beam. Beam images were taken for ± 1.5 mm corresponding to the beam radius of the 21 mA beam.

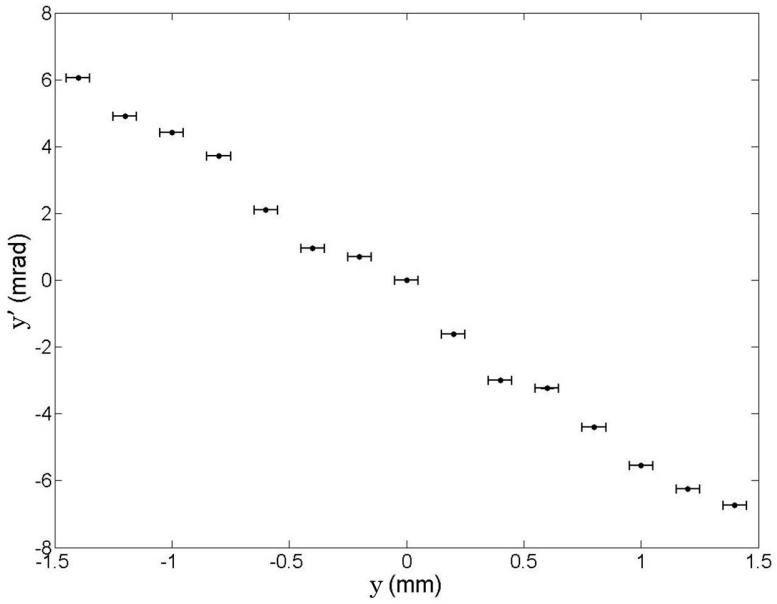

Figure 6.13: Phase space plot of the $V_{bias} = 10$ V beamlets. The scatter is a direct result of the grid intercepting the beam.

Emittance can be directly calculated from the moments of the pinhole images. As defined in Chapter 2, the emittance of the beam is

$$\epsilon_y = 4\sqrt{< y^2 >< y'^2 > - < yy' >^2}, \tag{6.5}$$

which can be written as

$$\epsilon = \sqrt{(r_0 r'_p)^2 - (r_0^2 tan\phi)^2}, \tag{6.6}$$

which is a coordinate-independent emittance. r_0 is the beam radius at the aperture, which is 1.5 mm for the 21 mA beam, r'_p is the ratio between the beamlet size to the beam aperture ($r_b/r_{pinhole}$), and $tan\phi$ is defined as

$$tan\phi = -\frac{< yy' >}{< y^2 >}, \tag{6.7}$$

which is just the slope of the fit line for the points in Figure 6.13. A table of these values for a range of bias voltages is given in Table 6.2.

Table 6.2: Pinhole scan method results

Grid Bias (V)	$tan\phi$	r'_p	Emitt. ϵ (mm-mrad)	σ_ϵ (mm-mrad)
10	-4.68	25.8	37.2	2.08
20	-4.89	26.5	38.2	1.89
30	-4.18	26.1	38.0	2.21
35	-4.66	25.4	36.6	2.71

The error is propagated, and the values of emittance from the pinhole scan are plotted on top of the emittance values from the envelope excitation method in Figure 6.14. This is not a direct comparison for several reasons. In an accelerator

experiment, emittance growth is inevitable. Thus, a measurement at injection will invariably have a lower value of emittance than for a measurement in the 5^{th} turn. The measurements are taken $\sim 0.9\ \mu s$ apart from each other during the lifetime of the beam. Additionally, any defect in the steering or matching can lead to emittance growth through the application of transverse energy to the beam. The values are relatively constant within the first $\sim 0.9\ \mu s$. This implies no significant emittance growth in the first 5 turns of UMER. The error in the pinhole scan is comparable to the error in the envelope resonance method. The benefit of the envelope resonance method, however, is the ability to measure emittance at any point in the ring, provided sufficient quadrupole perturbations have been applied.

Table 6.3: Exp. results of pin. scan and env. res. methods compared side-by-side.

V_{bias} (V)	ϵ_{pin} (μm)	$\sigma_{\epsilon,pin}$ (μm)	ϵ_{res} (μm)	$\sigma_{\epsilon,res,l}$ (μm)	$\sigma_{\epsilon,res,u}$ (μm)
10	37.2	2.08	38.2	2.8	1.8
20	38.2	1.89	37.4	2.1	1.5
30	38.0	2.21	40.6	3.9	2.3
35	36.6	2.71	39.7	3.0	1.9

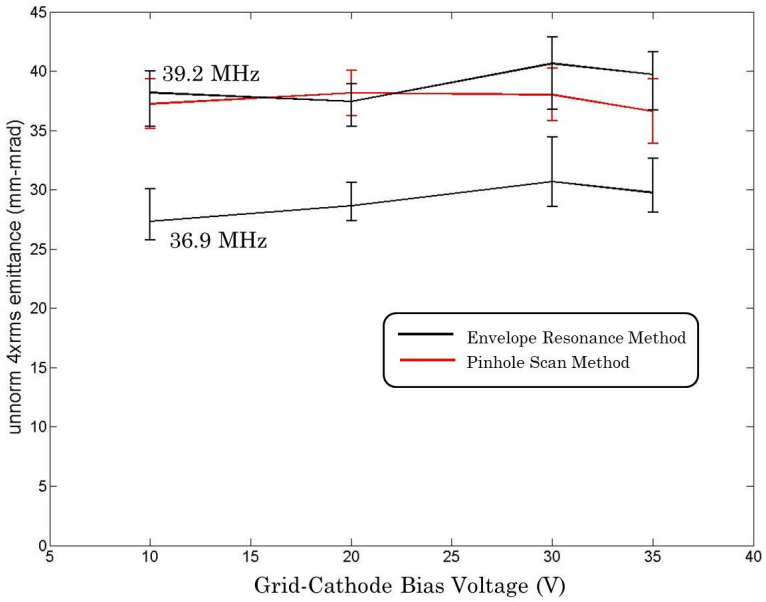

Figure 6.14: Emittance measurements from the pinhole scan at injection plotted with emittance measurements from envelope mode excitation in the 5^{th} turn. Measurements are at times $\sim 0.9\ \mu s$ apart from each other in the lifetime of the beam. The degeneracy shown in Figure 6.10 is resolved.

Chapter 7: Conclusion and Outlook

7.1 Summary

As particle accelerators increase in intensity, it is imperative to maintain good beam quality. For high energy physics, heavy ion applications, and free-electron lasers, the greatest challenge is to mitigate emittance growth during beam transport. To monitor emittance growth, a sensitive, non-invasive emittance diagnostic is required.

This dissertation reports successful demonstration of a sensitive, non-invasive emittance diagnostic using pulsed quadrupole envelope mode resonant excitations at the University of Maryland Electron Ring (UMER). The resonant growth structure is explored theoretically as well as in simulation and experiment. The resulting frequency measurements are used in concert with predictions from WARP envelope solver simulations to measure emittance. This method of measuring emittance can be applied to any circular accelerator or storage ring with intense-beam dynamics.

Periodic, impulsed perturbations were applied to the 21 mA UMER beam using an rf-driven electric quadrupole. The knockout imaging method captured 3 ns beam image slices at the center of the beam after four successive quadrupole perturbations. Image moments were calculated from these slices, and the envelope

mode frequency was identified. The emittance could then be inferred from the measured beam current and mode frequency using simulation results from numerical rms envelope integration. This works because the natural frequency of an envelope mode ω_0 depends explicitly on I/ϵ. The experiment was performed for a series of cathode-to-grid bias voltages.

There is good agreement between the delta-kicked simple harmonic oscillator model, rms envelope simulations, and experiment. The pinhole scan provides an experimental validation of the envelope resonance emittance measurement. It is shown that emittance can be measured with a 5-10% experimental uncertainty using the envelope resonance method, which is a comparable error to the pinhole scan method. The benefit to the envelope method is that it can be used to measure emittance at any location in the ring, provided sufficient quadrupole perturbations have been applied. Also, it is non-invasive when using long quadrupole pick-ups [18].

7.2 Future Work

7.2.1 Improvements on the Current Work

To reduce error in the current work, a better matching solution needs to be achieved that eliminates the skew in the beam. Barnard and Losic [44] studied envelope mode oscillations in a beam with angular momentum. Albeit a small perturbation, the mode frequencies depend on the skew, so a correction would improve the accuracy of the experiment. Unfortunately, current matching methods at UMER only involve systematic corrections in the first turn (see Appendix B).

To eliminate the degeneracy, the symmetry of the delta-kicked simple harmonic oscillator can be broken by using non-periodic impulsed perturbations. This can be implemented with the addition of another quadrupole placed at another location in the ring that does not diametrically oppose the first quadrupole's location. The resulting resonance structure (see Figure 7.1) shows a taller peak at the fundamental frequency, eliminating the degeneracy shown in this dissertation.

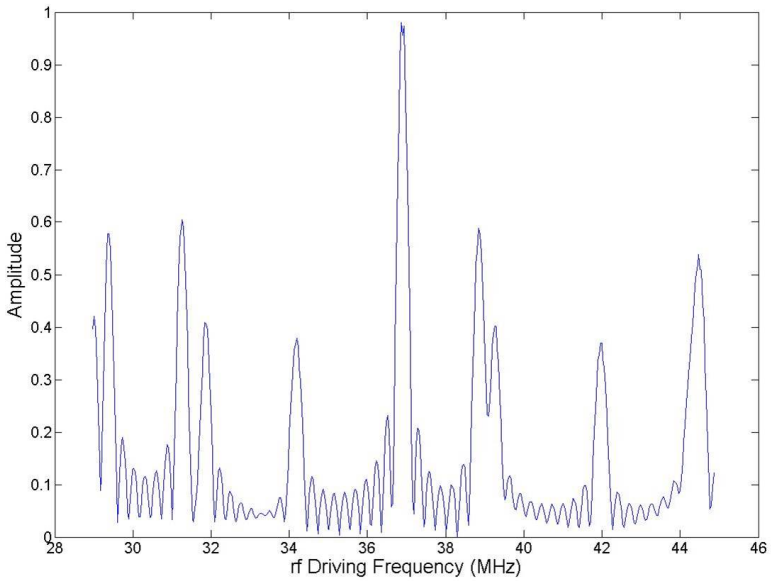

Figure 7.1: Degeneracy eliminated by breaking the periodicity of the impulses. This is simulation data from the integration of the delta-kicked SHO. Frequency structure is shown after 20 turns and 40 perturbations (two quadrupoles at different ring locations oscillating in phase with each other).

To permit non-invasive measurement of emittance, multi-plate BPMs can be used. Measuring beam size with a 4-plate BPM is difficult, but attainable [17,18,32]. A discussion of using UMER's BPMs for rms beam size measurements is provided

in Appendix C. 6-plate BPMs, however, more easily measure the rms beam spot size of a beam, allowing a non-invasive way to measure the resonant growth of the envelope [70]. This is very useful for emittance measurement, as the emittance is measured before the beam is used in an experiment. As an example, if the emittance in an intense particle beam needs to be adjusted for a target, the emittance diagnostic provides a real-time feedback mechanism of beam quality.

A digital micromirror device (DMD) is a digitally-controlled mirror lattice that has been proven as a successful way to measure beam halo in space-charge-dominated electron beams [19]. As shown in Chapter 3, measuring halo is an effective method of measuring resonant growth for intense beams with long lifetimes. Using this device, envelope excitations followed by halo measurements can be used to determine whether the beam is excited on resonance.

7.2.2 Ideas for Future Experiments

The work in this dissertation solely explores the quadrupole mode oscillation in the UMER 21 mA current electron beam. An extension is to investigate a range of beam intensities. It would be interesting to experimentally reproduce the phase advance plot shown in figure 3.8. Inductors have already been constructed to reach the rf frequency domains predicted for each of these intensities, and the rf amplitude would need to be modified according to equation 4.6. The most anticipated difficulty would be to find a steering and matching solution (see appendices A and B) such that there is minimal current loss as the beam is being perturbed.

It is not possible to perform the experiment for very high or low current beams. For beam currents larger than 21 mA, the longitudinal rarefaction wave will severely restrict the number of turns over which the perturbation can be applied. For UMER beams with a currents less than 6 mA, the frequencies of the envelope modes are close to the 1/2 integer resonance for particle oscillations. Perturbing this frequency will cause beam degradation and the emittance measurement would become invasive. Furthermore, the beam radius for small current beams would require large electrode voltages. The UMER "pencil beam" (0.6 mA) would need a peak-to-peak voltage of over 12 kV. Due to unavoidable transverse centroid displacements in the quadrupole, the beam would most likely not survive the kick.

While the envelope resonance method is not a plausible diagnostic for certain UMER currents, the emittance of the 6 mA beam can be characterized. The rarefaction wave does not reach the center of the beam until the 15^{th} turn, so with an appropriately matched beam, perturbations could be applied for 13 turns. This is a factor of 3 greater than the experiment detailed in this dissertation, and it should result in narrower, taller resonance peaks and possibly the formation of a beam halo.

Lund and Bukh [16] calculate several interesting results that would be interesting to explore experimentally. The mode frequencies depend on the focusing functions. Thus, perturbations on a alternating-gradient lattice structure should alter the oscillation frequency of an envelope mode. Bernal [73] has studied alternative lattice structures at the University of Maryland Electron Ring. It would be interesting to study the frequency dependence on the lattice focusing function and compare experimental and simulation results. Lund and Bukh [16] also described

the launching conditions for pure mode oscillations. Initial quadrupole mode excitation at injection has been measured at GSI [18] in 2014, and Hao [19] attempted pure mode injections at UMER. However, the lack of phase control makes it impossible to measure the mode frequency at one point in the ring, and the number of diagnostics in UMER leaves the oscillation period under-determined[1].

One final experiment that would be interesting to perform is a chaotic dynamics experiment. The beam, kicked hard enough, exhibits nonlinear behavior. The delta-kicked harmonic oscillator derived in Chapter 3 is used to study Hamiltonian chaos, specifically standard map bifurcations. By applying large quadrupole perturbations to the UMER beam at RC9 over long time scales (6 mA beam), the standard map can be explored.

[1] see Appendix C

Appendix A: Injection Steering in UMER

Steering the beam in the injection line is important to maintain beam quality in the ring. The goal is to steer the beam on to the equilibrium orbit of the ring without losing current. There are many possible steering solutions, but the method used in this dissertation minimizes the angle and displacement of the beam centroid from the center of the pipe in the injection line and uses the last few dipoles to kick the beam on to the desired orbit in the ring using the BPM traces as an empirical reference. Not only does this minimize the required magnet current, but it also provides a systematic approach to steering.

To benchmark the steering solution, the quadrupole magnets are used. If the beam is off-center as it passes through a quadrupole magnet, the magnet will impart a dipole kick to the beam. The beam is imaged using a gated camera and a phosphor screen located at RC1. A Matlab GUI is used on the camera control computer at the control desk to calculate the beam centroid of the camera image. If the application of a small current perturbation in the quadrupole causes the beam centroid to shift on the phosphor screen, the beam does not pass through the center of the quadrupole. A dipole upstream from the quadrupole is adjusted iteratively until a solution is found. This analysis is completed independently in x and y since

the transverse dimensions are uncoupled to first order.

With an equal number of dipole and quadrupole magnets, it is possible to steer through the center of all the quadrupole magnets. However, as it is seen from trajectory 1 in figure A.1, this solution requires a large amount of dipole current and results in large beam excursions. A different method involves a four step process that begins by considering the dipoles in groups of two.

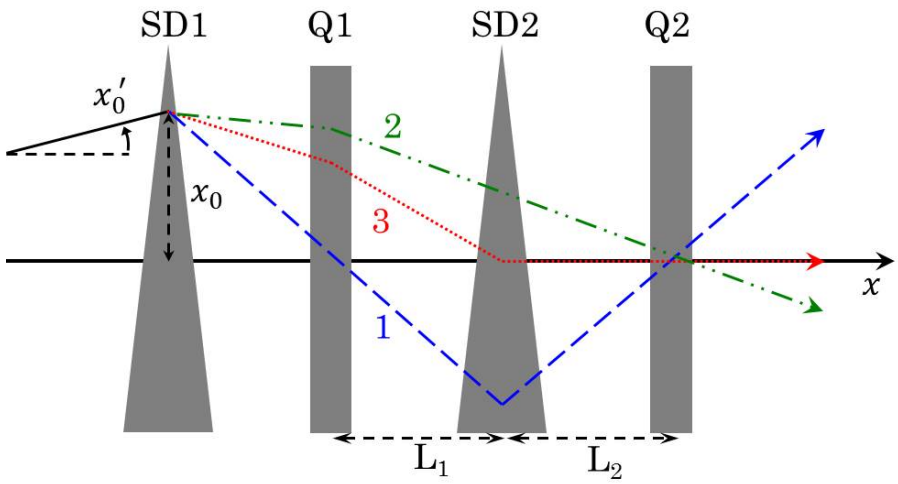

Figure A.1: This illustrates the four step process for centering the beam centroid horizontally in the injection line using pairs of steering dipoles (SD) and quadrupoles (Q). Step 1 (trajectory 1) steers the beam through the center of Q1. Step 2 (trajectory 2) is to turn SD2 off and steer through the center of Q2. Step 3 averages the two currents using equation A.1 to steer the beam through the center of SD2. Finally, step 4 uses SD2 to steer through the center of Q2, minimizing both displacement and angle.

- **Step 1:** Use the upstream dipole to steer through the center of the first quadrupole.

- **Step 2:** Turn off the downstream dipole and steer through the center of the

second quadrupole.

- **Step 3:** Steer through the center of the downstream dipole by appropriately averaging the current values from step 1 and 2 using longitudinal distances between magnets.

- **Step 4:** Use the downstream dipole to steer through the center of the second quadrupole.

This process is repeated for each subsequent dipole. Since in UMER the magnets are not equally spaced along the injection line, step 3 is a bit tricky and requires the ratio

$$I_{SD1} = \frac{L_1 I_{Q2} + L_2 I_{Q1}}{L_1 + L_2}, \tag{A.1}$$

where the subscripts 1 and 2 represent the upstream and downstream magnet components, respectively. I_{Q1} and I_{Q2} represent the currents required in the dipole SD1 to steer through the center of Q1 and Q2, respectively. L_1 is the longitudinal displacement between Q1 and SD2, and L_2 is the longitudinal displacement between SD2 and Q2.

The longitudinal displacements in the injection line are shown in figure A.2. It is worth noting that between SD3 and SD4 there are two quadrupole magnets. In this instance, it is best to use intuition to decide the quadrupole through which to steer.

The final horizontal and vertical steering currents used in the dipoles are shown in table $A.1$ for the 6 mA and 21 mA operating currents.

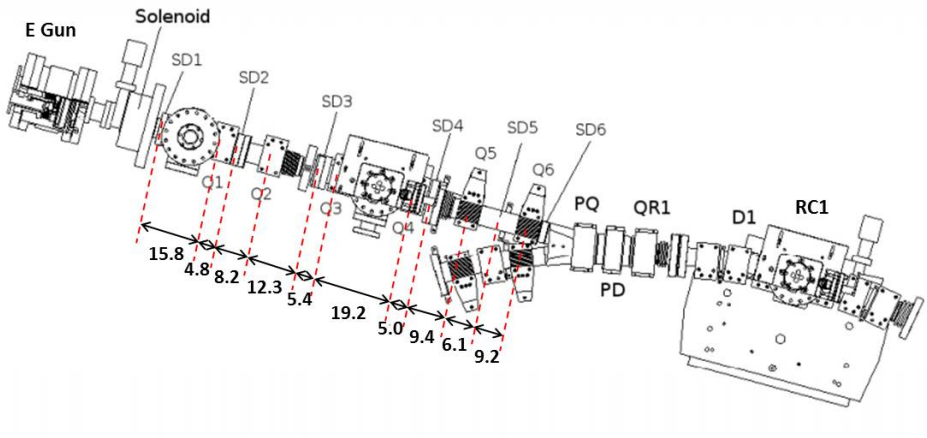

Figure A.2: Longitudinal displacements between magnet components in the UMER injection line. All displacements are in cm, measured to the center of each component with a tolerance of ±0.5 cm.

Table A.1: Dipole Currents, in Amps

	6mA		21mA	
Dipole	Horizontal	Vertical	Horizontal	Vertical
SD1	-0.55	1.6	0.85	1.97
SD2	-0.44	-0.15	-0.63	-1.25
SD3	0.19	0.85	-0.05	-0.8
SD4	-0.66	-1.6	0.3	1.5
SD5	0.2	-0.02	-0.7	0.4
SD6	0.5	1.0	1.0	-0.5
SDR6	-0.9	0.0	0.0	0.5

Appendix B: First-Turn Matching Technique

To reduce error in the experiment, a transverse matching algorithm was employed before taking data [19, 27]. As in Appendix A, this method is applied to the injection section of the ring, and it is implemented after a steering solution to send the beam through the center of the quadrupole magnets is found. All beam sizes in this section are defined as the 2xrms transverse beam size in x or y

This method involves an iteration of the matched beam sizes X_m and Y_m by filling a response matrix R_{wij} with the change in x or y (subscript w) beam size at various locations (subscript i) in the ring after changing a quadrupole magnet current (subscript j). It is defined as

$$R_{wij} = \frac{\partial w_i}{\partial I_j}, \tag{B.1}$$

where w can be either the x or y dimension. It is used to calculate the tensor $\mathbf{\Delta}$, where

$$\mathbf{E} = \mathbf{R}\mathbf{\Delta}, \tag{B.2}$$

expanded as

$$\begin{pmatrix} X_1 \\ Y_1 \\ X_2 \\ Y_2 \\ \cdots \\ X_n \\ Y_n \end{pmatrix} = \begin{pmatrix} R_{x11} & R_{x12} & R_{x13} & R_{x14} & 1 & 0 \\ R_{y11} & R_{y12} & R_{y13} & R_{y14} & 0 & 1 \\ R_{x21} & R_{x22} & R_{x23} & R_{x24} & 1 & 0 \\ R_{y21} & R_{y22} & R_{y23} & R_{y24} & 0 & 1 \\ \cdots & \cdots & \cdots & \cdots & \cdots & \cdots \\ R_{xn1} & R_{xn2} & R_{xn3} & R_{xn4} & 1 & 0 \\ R_{yn1} & R_{yn2} & R_{yn3} & R_{yn4} & 1 & 0 \end{pmatrix} \begin{pmatrix} \Delta I_1 \\ \Delta I_2 \\ \Delta I_3 \\ \Delta I_4 \\ X_m \\ Y_m \end{pmatrix}. \tag{B.3}$$

X_n in the tensor $\mathbf{E}$ are the beam sizes at the location n, ΔI_k is the change in current at quadrupole magnet k, and X_m and Y_m are the current matched beam sizes. $\mathbf{\Delta}$ is calculated using

$$\mathbf{\Delta} = (\mathbf{R}^T\mathbf{R})^{-1}\mathbf{R}^T\mathbf{E}. \tag{B.4}$$

The improved solutions to the currents in quadrupole magnets 1-4 are given by $I_1 - \Delta I_1$, $I_2 - \Delta I_2$, $I_3 - \Delta I_3$, and $I_4 - \Delta I_4$. This process is iterated until a solution is found.

The analysis was performed at the UMER ring for the 21 mA electron beam. The ring chambers used for matching were 1, 2, 5, and 12. A few combinations of quadrupole magnets were used in the above analysis to find the best solution. After a solution was found, the process was iterated again for further improvement. The first two iterations are shown in figures B.1 and B.2. Over iterations, the solution converges to a more consistent beam size across all 4 ring chambers.

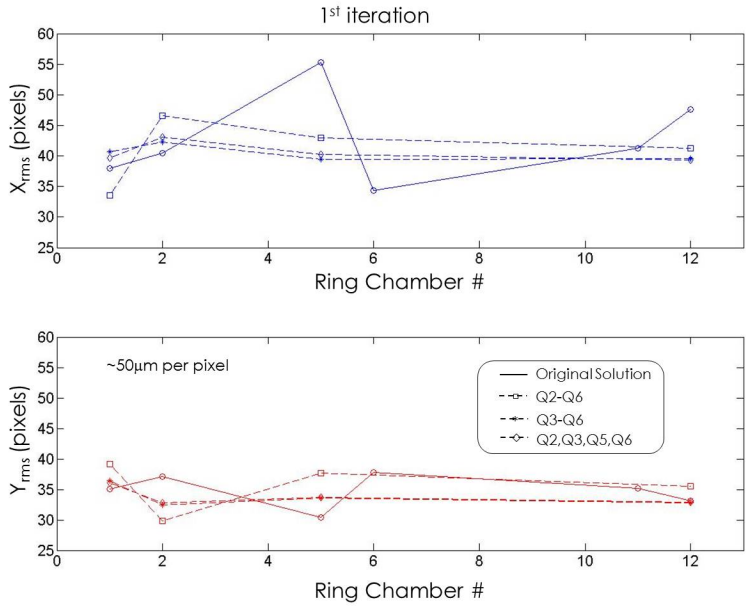

Figure B.1: X_{rms} and Y_{rms} beam size as a function of ring chamber on the 1^{st} iteration.

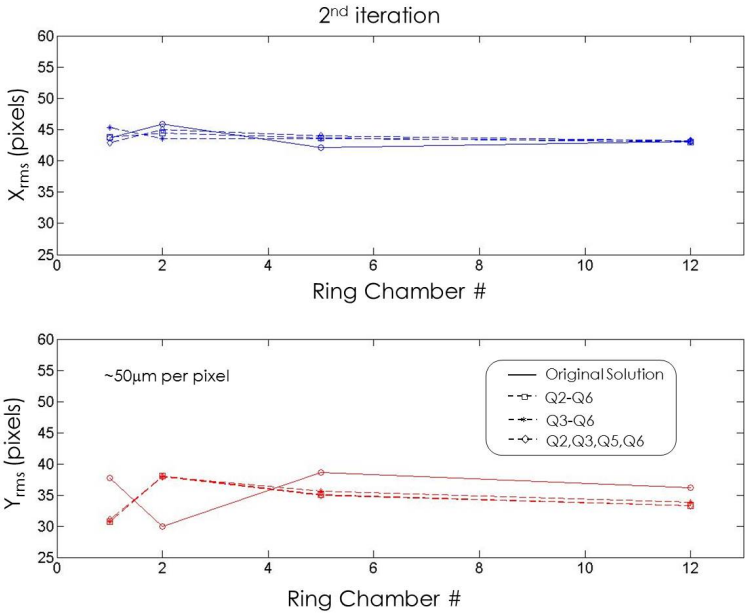

Figure B.2: X_{rms} and Y_{rms} beam size as a function of ring chamber on the 2^{nd} iteration.

Appendix C: Using Quadrupole Pick-ups to Measure Envelope Mode Frequency at UMER

Beam size has been measured with quadrupole pick-ups at accelerators across the world [17, 18, 32]. This Appendix will explain the difficulty in using this diagnostic at the University of Maryland Electron Ring (UMER).

Figure C.1 shows a measurement taken from two plates of a beam position monitor (BPM) after four rf quadrupole perturbations at UMER. The base signal is subtracted out, and all that is left is the perturbation applied by the quadrupole. It seems that the information needed is available in this plot to resolve the natural frequency of the envelope oscillations. However, the sine wave distribution reflects the applied rf frequency, not the natural frequency of the beam, since it is sampling along the longitudinal length of the beam as it passes. Since the BPMs are so short (< 2"), time-dependent oscillations cannot be recovered from a single BPM. With only 12 working BPMs, the Nyquist-Shannon theorem suggests that the system is under-determined and cannot be recovered. The quadrupole pick-up used in the GSI experiment was long enough (216 mm) to sample an entire period of an envelope mode oscillation. Although possible with more BPMs, it would be difficult to precisely recover the mode frequency with discretized measurements of beam size.

The center of the beam would need to be tracked within a 3 ns time slice to get resolution equal to the method presented in this dissertation.

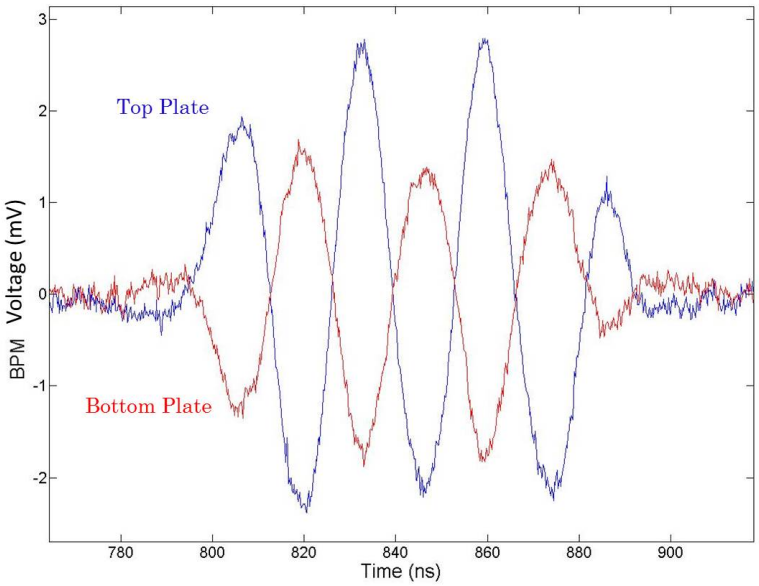

Figure C.1: Beam position monitor (BPM) data of the top and bottom plates taken after 4 perturbations with the rf quadrupole. The base BPM signal is subtracted out.

Furthermore, figure C.1 shows data from the top and bottom plates. The 90° phase shift between the signals implies that the largest contribution from the rf quadrupole is transverse translation, not expansion and contraction. An envelope mode should have an in-phase oscillation in the top and bottom plates, as illustrated in figure 2.10. Due to this beam "wiggle" in time, it would be very difficult to resolve a natural frequency. The wiggle frequency would reflect the applied rf frequency of the quadrupole, which is close to or equal to the natural frequency of the mode oscillation. Fourier analysis would result in two overlapping frequency peaks, with the

smallest amplitude being the desired natural frequency of the envelope oscillation.

Appendix D: RF Box Construction

This appendix outlines construction details of the rf box. The box was constructed using six pieces of 1/8" thick copper sheet (12"x12"). 0.25" aluminum angle was used to form a rigid structure for the copper, with 0.01" gauge copper bolted and soldered around the inside edges of the box to maintain uniform conductivity. Pictures of the box's assembly are shown in Figure D.1.

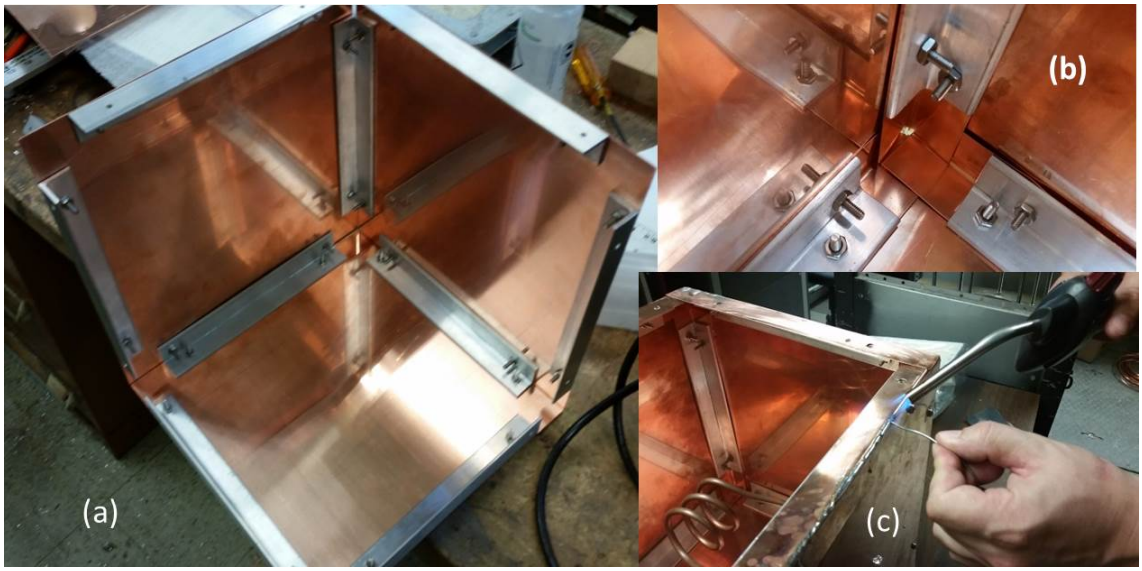

Figure D.1: Pictures of the rf box construction. (a) 0.25" Aluminum angle is used to keep a rigid structure. (b) 0.01" copper sheet is bent and placed between the edges and aluminum angle. (c) The copper sheet is soldered to the box sides to maintain uniform conductivity.

Such that the box can be secured on the 6" to $2\frac{3}{4}$" flange, "Fingers" are cut into the bottom of the box alongside an array of holes for the screw heads of the flange. This is pictured in figure D.2. The fingers are bent up and the $2\frac{3}{4}$" flange fits in the opening, secured with a hose clamp.

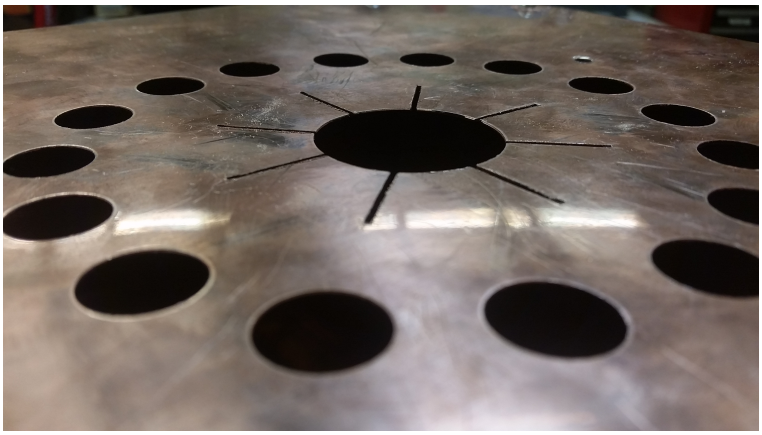

Figure D.2: 0.5" fingers are cut into the copper sheet at the bottom of the rf box to secure the box on top of the 6" flange at RC9. The array of holes shown around the fingers are positioned for screw head and washer clearance of the 6" flange.

The trim capacitor was secured by bolting one end to the bottom of the box and securing the top of the capacitor using ceramic standoffs as shown in figure D.3. Due to the thick (1/8") copper sheet, the trim capacitor maintained its rigid structure.

The air-core inductor in the primary circuit was constructed using 0.25" copper tubing wound around a 2" diameter mandrill on a lathe shown in figure D.4. The length of the coil is easily modified once the mandrill is removed by compressing the loops in an accordion-like manor. A tubing cutter was used to remove excess copper from the end of the coil.

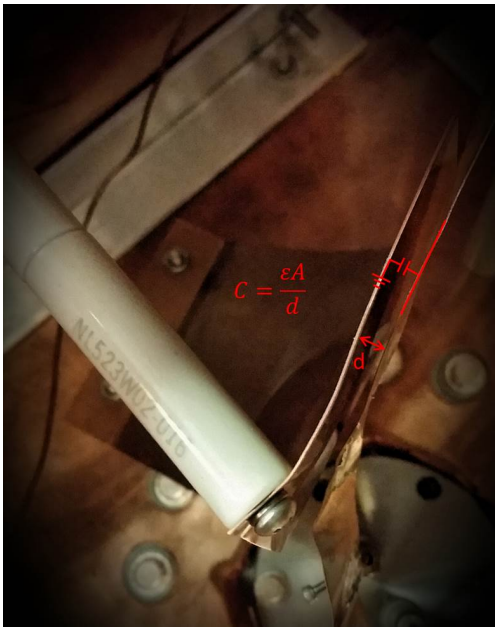

Figure D.3: Trim capacitor constructed by bolting a sheet of copper to the floor of the rf box, stabilized with ceramic standoffs.

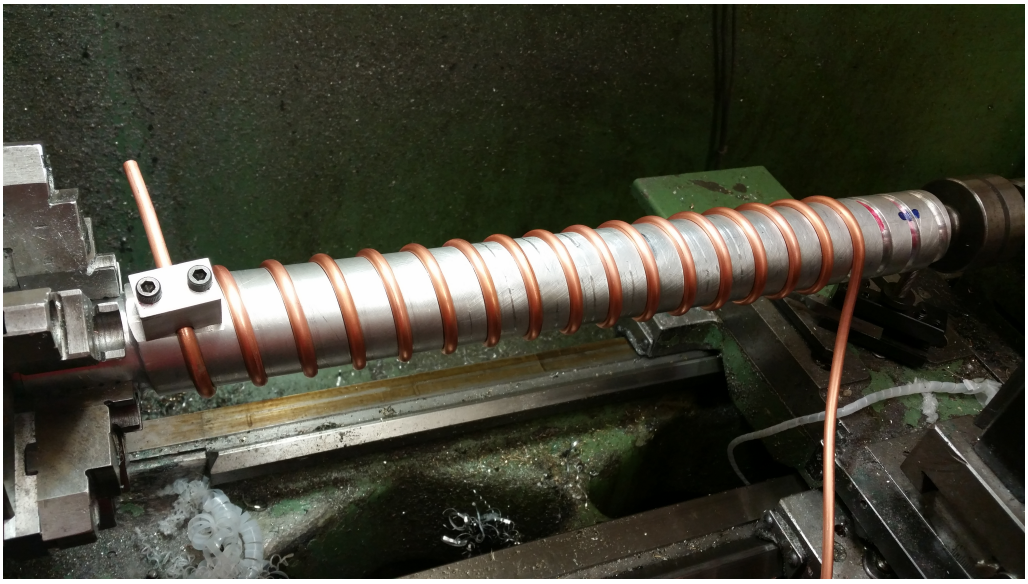

Figure D.4: Constructing inductors out of 0.25" copper tubing using a 2" diameter mandrill mounted on a lathe.

Bibliography

[1] R.R. Wilson, "The Tevatron," *Physics Today* **10** 23-30 (1977).

[2] L. Evans, "The Large Hadron Collider," *New J. Phys* **9** 335 (2007).

[3] S.C. Klevenhagen, *Principles and Practice of Radiation Oncology* (JNCI Cancer Spectrum, 5th Edition, Lippincott Williams & Wilkins, 2008).

[4] A. Singh and J. Silverman, *Radiation Processing of Polymers*, Germany, 1992.

[5] J.F. Diehl, *Safety of Irradiated Foods*, (Marcel Dekker, Inc., New York, 1995).

[6] M.J. Burns et al. "Status of the DARHT Phase 2 Long-Pulse Accelerator," (PAC Proceedings, Chicago, 2001).

[7] J. Arthur et al., "Linac Coherent Light Source (LCLS) Conceptual Design Report," (SLAC-R-593, 2002).

[8] T. Raubenheimer, "The LCLS-II, a New FEL Facility at SLAC," (Proc. of FEL2014, Switzerland, 2014).

[9] M.G. Minty and F. Zimmerman, *Measurement and Control of Charged Particle Beams* (Springer, Berlin, 2003).

[10] S.G. Anderson, J.B. Rosenzweig, G.P. LeSage and J.K. Crane, "Space-Charge effects in high brightness electron beam emittance measurements," Phys. Rev. ST Accel. Beams **5**, 014301, 2002.

[11] E.D. Courant and H.S. Snyder, *Theory of the Alternating-Gradient Synchrotron* (Annals of Physics, 1958), Chap. 3.

[12] I.M. Kapchinsky and V.V. Vladimirsky, *Proc. Int. Conference on High Energy Accelerators and Instrumentation* (CERN, 1959) pp. 274-288.

[13] P.M. Lapostolle, *IEEE Trans. Nucl. Sci.* (**NS-18**, 1971) p. 1101.

[14] F.J. Sacherer, *IEEE Trans. Nucl. Sci.* (**NS-18**, 1971) p. 1105.

[15] J. Struckmeier and M. Reiser, "Theoretical Studies of Envelope Oscillations and Instabilities of Mismatched Intense Charged-Particle Beams in Periodic Focusing Channels," *Particle Accelerators* (Vol. 14, 1984), pp. 227-160.

[16] S.M. Lund and B. Bukh, "Stability Properties of the Transverse Envelope Equations Describing Intense Ion Beam Transport," PRST-AB **7**, 024801 (2004).

[17] C.D. Nantista, "A Quadrupole Mode Resonant Cavity for Non-Disruptive, Single-Shot Emittance Measurement," SLAC-PUB-9501, 2002.

[18] R. Singh, P. Forck, P. Kowina, "Observations of the Quadrupolar Oscillations at GSI SIS-18," IBIC Proceedings, 2014.

[19] H. Zhang, "Experimental Study of Beam Halo in Intense Charge Particle Beams," (Doctoral Dissertation, University of Maryland, 2014).

[20] C. Papadopoulos, "Halo Creation and Propagation in the University of Maryland Electron Ring," (Doctoral Disseration, University of Maryland, 2009).

[21] H. Okamoto and H. Tanaka, "Proposed experiments for the study of beam halo formation," Nucl. Instr. Meth. in Phys. Res. A 437, 1999. pp. 178-187.

[22] E.P. Gilson, M. Chung, R.C. Davidson, P.C. Efthimion, R. Majeski and E.A. Startsev, "Simulation of Long-Distance Beam Propagation in the Paul Trap Simulator Experiment," Nucl. Instr. Meth. in Phys. Res. A 554, 2005. pp. 171-178.

[23] T.W. Koeth, B. Beaudoin, S. Bernal, I. Haber, R.A. Kishek, P.G. O'Shea, "Bunch-End Interpenetration During Evolution to Longitudinal Uniformity in a Space-Charge-Dominated Storage Ring," (PAC Proceedings, New York, 2011).

[24] J.C.T. Thangaraj, "Study of Longitudinal Space Charge Waves in Space-Charge-Dominated Beams," (Doctoral Dissertation, University of Maryland, 2009).

[25] B. Beaudoin, "Longitudinal Control of Intense Charged Particle Beams," (Doctoral Dissertation, University of Maryland, 2011).

[26] Y. Mo, "Study of Soliton Space Charge Waves in Intense Electron Beams," (Doctoral Dissertation, University of Maryland, 2013).

[27] H. Li, "Control and Transport of Intense Electron Beams," (Doctoral Dissertation, University of Maryland, 2004).

[28] D. Stratakis, "Tomographic Measurement of the Phase Space Distribution of a Space-Charge-Dominated Beam," (Doctoral Dissertation, University of Maryland, 2008).

[29] W. Guo and S.Y. Lee, "Quadrupole-mode transfer function and the nonlinear Mathieu instability," Phys. Review E, Vol. 65, 066505.

[30] M. Bai, "Non-Destructive Beam Measurements," Proc. of EPAC 2004, Lucerne, Switzerland

[31] W. Hardt, "On the Incoherent Space Charge Limit for Elliptical Beams," ISR, Geneva, 1966.

[32] A. Jansson, "Non-invasive single-bunch matching and emittance monitor," Phys. Rev. ST Accel. Beams **5**, 072803, 2002.

[33] J.D. Jackson, *Classical Electrodynamics* (3rd Edition, Wiley, 1999).

[34] K. Wille, *The Physics of Particle Accelerators, an introduction* (Oxford University Press, 2000), pg. 49.

[35] S.Y. Lee, *Accelerator Physics* (2nd Edition, World Scientific, 2004).

[36] D.A. Edwards and M.J. Syphers, *An Introduction to the Physics of High Energy Accelerators* (Wiley-VCH, 2004).

[37] M. Reiser, *Theory and Design of Charged Particle Beams* (2nd Edition, Wiley-VCH, 2008).

[38] P.J. Bryant and K. Johnsen, *The Principles of Circular Accelerators and Storage Rings* (Cambridge University Press, 1993).

[39] H. Wiedemann, *Particle Accelerator Physics* (3rd Edition, Springer, 2007)

[40] L. Smith, "Effect of Gradient Errors in the Presence of Space-Charge Forces," Proceedings of the International Conference on High-Energy Accelerators, 1963, p. 897.

[41] S.M. Lund, "Transverse Particle Dynamics," (USPAS lecture notes "Beam Physics With Intense Space-charge," 2015). p. 34.

[42] S.M. Lund and J.J. Barnard, "Transverse Equilibrium Distributions," (USPAS lecture notes "Beam Physics With Intense Space-Charge," 2006). p. 39.

[43] T.W. Koeth, "An Observation of a Transverse to Longitudinal Emittance Exchange at the Fermilab A0 Photoinjector," (Doctoral Dissertation, Rutgers University, 2009).

[44] J.J. Barnard and B. Losic. "Envelope Modes of Beams with Angular Momentum," (20th International Linear Accelerator Conference, 2000).

[45] R.L. Gluckstern, "Analytic Model for Halo Formation in High Current Ion Linacs," *Physical Review Letters* (Volume 73, Number 9, 1994).

[46] T. Wangler, et al. "Particle-core model for transverse dynamics of beam halo," *Phys. Rev. ST Accel. Beams* (1(8):084201, 1998).

[47] A. Friedman, R.H. Cohen, D.P. Grote, S.M. Lund, W.M. Sharp, J.-L. Vay, I. Haber, R.A. Kishek, "Computational Methods in the Warp Code Framework for Kinetic Simulations of Particle Beams and Plasmas," (IEEE Transactions on Plasma Science, **42** (**5**) 1321, 2014).

[48] I. Haber et al. "Space-Charge-Dominated Phenomena in the UMER Source Region," (PAC Proceedings, 2003).

[49] Y. Zou, H. Li, M. Reiser, P.G. O'Shea, "Theoretical Study of Transverse Emittance Growth in a Gridded Electron Gun," Nucl. Instr. Meth. in Phys. Res. A 519, 2004. pp. 432-441.

[50] Pro/Engineer home page, `www.ptc.com/product/creo/proengineer`, 2015.

[51] Solidworks home page, `http://www.solidworks.com/`, 2015.

[52] Maxwell 3D home page, `http://www.ansys.com/Products/Simulation+Technology/Electronics/Electromechanical/ANSYS+Maxwell`, 2015.

[53] J.R. Nagel, "Solving the Generalized Poisson Equation Using the Finite-Difference Method (FDM)." (IEEE AP-S, Utah, 2011).

[54] H.P. Westman, *Reference Data for Radio Engineers, Fourth Edition* (Inernational Telephone and Telegraph Corporation, 1949), Chap. 5.

[55] F.E. Terman, *Radio Engineering* (McGraw-Hill Book Company, Inc., New York and London, 1937).

[56] S.-B. Liao, P. Dourmashkin, and J. Belcher. *Introduction to Electricity and Magnetism* (MIT 8.02 Course Notes, Pearson, 2011), Chap. 12.

[57] T.R. Kuphaldt. *Lessons In Electric Circuits, Volume II - AC* (6th edition, 2007), Chap. 6.

[58] T.W. Koeth, "Theoretical Calculations and Measurements of the DEE Voltage in the Rutgers 12 Inch Cyclotron." (2005).

[59] H. Wollnik, *Optics of Charged Particles* (Academic Press, Inc., London, 1987), Chap. 3.

[60] P.W. Hawkes, *Quadrupoles in Electron Lens Design* (Supplement 7, Academic Press, New York, 1970).

[61] F. Krawczyk, "Download Area for Poisson Superfish," Los Alamos Code Group, 2012.

[62] "Lecture 16: Designing With Inductors." (IEEE-B, Oklahoma State University).

[63] "E5061B-3L5 LF-RF Network Analyzer with Option 005 Impedance Analysis Function Data Sheet," (Agilent Technologies, Inc., USA, 2013).

[64] Private Communication with Tom Loughran, senior staff of the UMD FabLab.

[65] W.D. Stem et al. "Recovering Measured Dynamics From a DC Circulating Space-Charge-Dominated Storage Ring." IPAC 2012 Proceedings, New Orleans.

[66] PIMAX2-ICCD Camera Data Sheet, `http://www.prom-sys.com/pdf/pimax2_512.pdf`.

[67] J.R. Taylor. *An Introduction to Error Analysis: The Study of Uncertainties in Physical Measurements* (University Science Books, 1997).

[68] N.H. Cook and E. Rabinowicz. *Physical Measurement and Analysis* (Addison-Wesley Publishing Company, Inc., Reading, MA, 1963).

[69] J.H. Moore, C.C. Davis, M.A. Coplan. *Building Scientific Apparatus: A Practical Guide to Design and Construction* (4th Edition, Cambridge University Press, 2009).

[70] K. Yanagida, S. Suzuki, and H. Hanaki. "Design study of beam position monitors for measuring second-order moments of charged particle beams," Phys. Rev. ST Accel. Beams **15**, 012801, 2012.

[71] JAMPRO Return Loss Conversion Table, `http://www.jampro.com/uploads/tech_docs_pdf/VSWRChart.pdf`, 2015.

[72] S. Dey, B.B. Bhattacharya, M.K. Kundu, and T. Acharya, "A Simple Architecture for Computer Moments and Orientation of an Image," Fundamenta Informaticae **52**, 2002. pp. 1-11.

[73] S. Bernal, B.L. Beaudoin, M. Cornacchia, D. Sutter, and R.A. Kishek, "Beam Transport in Alternative Lattices at the University of Maryland Electron Ring (UMER)," IPAC Proceedings, New Orleans, 2012.